



Institut de physique

---

# EXPERIMENTAL TECHNIQUES FOR OPTICAL FREQUENCY METROLOGY

---

Thèse présentée à la Faculté des Sciences pour l'obtention  
du grade de docteur ès sciences par:

**Nikola Bucalović**

Graduate physicist, Faculty of Physics  
University of Belgrade, Serbia

acceptée le 28.01.2014. sur proposition du jury:

Prof. hon. Pierre Thomann, directeur de thèse

Prof. Thomas Südmeyer, rapporteur

Dr. Stéphane Schilt, rapporteur

Dr. Steve Lecomte, rapporteur

Dr. Jacques Millo, rapporteur

Neuchâtel, 2014

## IMPRIMATUR POUR THESE DE DOCTORAT

---

**La Faculté des sciences de l'Université de Neuchâtel  
autorise l'impression de la présente thèse soutenue par**

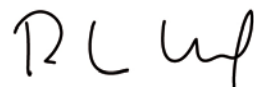
**Monsieur Nikola BUCALOVIC**

Titre:

**Experimental Techniques for Optical Frequency Metrology**

**sur le rapport des membres du jury composé comme suit :**

- Prof. hon. Pierre Thomann, Université de Neuchâtel, directeur de thèse
- Prof. Thomas Südmeyer, Université de Neuchâtel
- Dr Stéphane Schilt, Université de Neuchâtel
- Dr Steve Lecomte, CSEM, Neuchâtel
- Dr Jacques Millo, FEMTO-ST, Besançon, France



Neuchâtel, le 25 février 2014

Le Doyen, Prof. P. Kropf



*To all dear friends and good people, on both sides of time...*



# Acknowledgments

I would like to thank to all of the colleagues from the Laboratoire Temps-Fréquence for the time we spent together. In the last four years they became friends and an inseparable part of my life.

Stéphane Schilt was an all-time present helping hand. He introduced me into the laboratory techniques and has made a significant effort to improve my publication record. Gianni Di Domenico shared generously his engineering and scientific expertise. Without him many important aspects of the work described in this thesis simply would not have been possible. Thomas Südmeyer, as a new, young and dynamic leader of the LTF, has introduced the new standards and is responsible for the positive and challenging experience of the presentation of our work at the world-class conferences. Also, I wish to thank him for his infinite patience in numerous stressful situations. I strongly appreciate the time spent and the advices of the thesis jury members Steve Lecomte and Jacques Millo, whose experience has strongly contributed to the quality of the text presented in this work.

Above all, I want to point out the support, the wisdom and the intellectual generosity of Pierre Thomann. Only in the hands of a real gentleman, the power of decision making is capable of the positive creation, while maintaining the human touch and the respect for each person involved in the process.

I also thank to all the people that at some point have helped me with various aspects of research or everyday life activities. I assure you that your good deeds will not be forgotten.



# Keywords

optical frequency comb, ultra-stable laser, optical frequency metrology, frequency discriminator, beta-separation line, frequency noise





# Abstract

In the framework of this thesis, I present recent activities in the Laboratoire Temps-Fréquence (LTF) of the University of Neuchâtel, concerning the optical frequency metrology group. We developed the frequency discriminator technique for the characterization of the narrow linewidth heterodyne optical beats. The examination of the four different types of the frequency and phase discriminators has identified the appropriate tools for the analysis of the low-noise signals. We made the experimental test of the  $\beta$ -separation line formalism that enables easy calculation of the laser linewidth from its frequency noise power spectral density (PSD). Earlier proposed geometrical approximation has been validated in a wide linewidth range and for different laser line shapes. We developed and characterized the second ultra-stable high-finesse Perot-Fabry passive reference cavity. A novel low-noise planar waveguide extended cavity laser (PW-ECL) has been stabilized to this reference cavity in a Pound-Drever-Hall stabilization scheme. A thermal model of the cavity enclosure has been made and based on that an improvement in the temperature control system was possible, resulting in the higher flexibility of the cavity temperature change. Finally, the noise properties of a novel type of the ultrafast optical frequency comb were examined. A diode-pumped solid-state laser (DPSSL) Er:Yb:glass (ERGO) frequency comb is proven to be capable of the coherent frequency division from optical to microwave, at the level of stability of  $10^{-15}$  at 1 s. It is shown that the dynamics of the carrier-envelope offset (CEO) beat plays an important role in the stabilization of this type of the ultrafast laser.



# Publications

Parts of this thesis are published in the following journal papers and conference proceedings.

## Journal papers

- [1] N. Bucalovic, V. Dolgovskiy, M. C. Stumpf, C. Schori, G. Di Domenico, U. Keller, S. Schilt, and T. Südmeyer, “Effect of the carrier-envelope-offset dynamics on the stabilization of a diode-pumped solid-state frequency comb,” *Optics Letters*, vol. 37, pp. 4428–4430, Nov. 2012.
- [2] N. Bucalovic, V. Dolgovskiy, C. Schori, P. Thomann, G. Di Domenico, and S. Schilt, “Experimental validation of a simple approximation to determine the linewidth of a laser from its frequency noise spectrum,” *Applied Optics*, vol. 51, no. 20, p. 4582–4588, 2012.
- [3] S. Schilt, N. Bucalovic, V. Dolgovskiy, C. Schori, M. C. Stumpf, G. D. Domenico, S. Pekarek, A. E. H. Oehler, T. Südmeyer, U. Keller, and P. Thomann, “Fully stabilized optical frequency comb with sub-radian CEO phase noise from a SESAM-modelocked 1.5- $\mu\text{m}$  solid-state laser,” *Opt. Express*, vol. 19, p. 24171–24181, Nov. 2011.
- [4] S. Schilt, N. Bucalovic, L. Tombez, V. Dolgovskiy, C. Schori, G. Di Domenico, M. Zaffalon, and P. Thomann, “Frequency dis-

criminators for the characterization of narrow-spectrum heterodyne beat signals: application to the measurement of a sub-hertz carrier-envelope-offset beat in an optical frequency comb,” *Review of Scientific Instruments*, vol. 82, no. 12, p. 123116–123116, 2011.

- [5] V. Dolgovskiy, N. Bucalovic, P. Thomann, C. Schori, G. Di Domenico, and S. Schilt, “Cross-influence between the two servo loops of a fully stabilized Er:fiber optical frequency comb,” *JOSA B*, vol. 29, no. 10, p. 2944–2957, 2012.
- [6] V. Giordano, S. Grop, B. Dubois, P.-Y. Bourgeois, Y. Kersale, G. Haye, V. Dolgovskiy, N. Bucalovic, G. D. Domenico, S. Schilt, J. Chauvin, D. Valat, and E. Rubiola, “New-generation of cryogenic sapphire microwave oscillators for space, metrology, and scientific applications,” *Review of Scientific Instruments*, vol. 83, no. 8, p. 085113, 2012.
- [7] S. Schilt, V. Dolgovskiy, N. Bucalovic, C. Schori, M. C. Stumpf, G. Di Domenico, S. Pekarek, A. E. H. Oehler, T. Südmeyer, U. Keller, and P. Thomann, “Noise properties of an optical frequency comb from a SESAM-mode-locked 1.5- $\mu\text{m}$  solid-state laser stabilized to the  $10^{-13}$  level,” *Applied Physics B*, vol. 109, pp. 391–402, May 2012.
- [8] V. Dolgovskiy, S. Schilt, N. Bucalovic, G. Domenico, S. Grop, B. Dubois, V. Giordano, and T. Südmeyer, “Ultra-stable microwave generation with a diode-pumped solid-state laser in the 1.5- $\mu\text{m}$  range,” *Applied Physics B*, pp. 1–9, DOI: 10.1007/s00340-013-5740-7, 2013.

## Conference papers

- [1] N. Bucalovic, S. Schilt, V. Dolgovskiy, G. Di Domenico, S. Grop, B. Dubois, V. Giordano, M. Stumpf, S. Pekarek, U. Keller, and

- T. Südmeyer, “Near-infrared diode-pumped solid-state frequency comb for ultra-stable microwave generation,” in *UFO 2013, talk Mo4.2*, (Davos, Switzerland), Mar. 2013.
- [2] N. Bucalovic, V. Dolgovskiy, C. Schori, P. Thomann, G. Di Domenico, and S. Schilt, “Experimental validation of a simple approximate relation between laser frequency noise and linewidth,” in *CLEO 2012, talk CF1C.7*, (San Jose, USA), May 2012.
- [3] N. Bucalovic, V. Dolgovskiy, M. Stumpf, C. Schori, P. Thomann, G. Di Domenico, S. Pekarek, A. Oehler, T. Südmeyer, U. Keller, and S. Schilt, “Importance of the carrier-envelope-offset dynamics in the stabilization of an optical frequency comb,” in *EFTF 2012, talk #3148*, (Gothenburg, Sweden), Apr. 2012.
- [4] N. Bucalovic, S. Schilt, V. Dolgovskiy, C. Schori, L. Tombez, G. Di Domenico, M. Stumpf, S. Pekarek, A. Oehler, T. Südmeyer, U. Keller, and P. Thomann, “Er:Yb:glass oscillator (ERGO): a low-noise optical frequency comb for frequency metrology,” in *EGAS 43, poster AAP-002*, (Fribourg, Switzerland), June 2011.
- [5] V. Dolgovskiy, N. Bucalovic, S. Schilt, G. Di Domenico, P. Thomann, S. Grop, B. Dubois, V. Giordano, M. Stumpf, S. Pekarek, U. Keller, and T. Südmeyer, “Comparison of low-noise microwave generation from ultrafast fiber and DPSSL frequency combs,” in *Europhoton 2012, talk ThD.4*, (Stockholm, Sweden), Aug. 2012.
- [6] V. Dolgovskiy, N. Bucalovic, C. Schori, P. Thomann, G. Di Domenico, and S. Schilt, “Correlated impact of the feedback loops on the noise properties of an optical frequency comb,” in *DPG 2012, talk Q 28.4*, (Stuttgart, Germany), Mar. 2012.
- [7] S. Schilt, N. Bucalovic, V. Dolgovskiy, C. Schori, L. Tombez, G. Di Domenico, M. Stumpf, S. Pekarek, A. Oehler, T. Südmeyer, U. Keller, and P. Thomann, “Low-noise near-infrared optical

- frequency comb from a solid-state femtosecond laser,” in *Joint IFCS/EFTF 2011, talk #132*, (San Francisco, USA), May 2011.
- [8] S. Schilt, V. Dolgovskiy, N. Bucalovic, L. Tombez, M. Stumpf, G. Di Domenico, C. Schori, S. Pekarek, A. Oehler, T. Südmeyer, U. Keller, and P. Thomann, “Optical frequency comb with sub-radian CEO phase noise from a SESAM-modelocked 1.5  $\mu\text{m}$  solid-state laser,” in *CLEO 2011, talk CFK3*, (Baltimore, USA), May 2011.
- [9] V. Dolgovskiy, S. Schilt, G. Di Domenico, N. Bucalovic, C. Schori, and P. Thomann, “1.5- $\mu\text{m}$  cavity-stabilized laser for ultra-stable microwave generation,” in *Joint IFCS/EFTF 2011, poster #228*, (San Francisco, USA), May 2011.
- [10] S. Schilt, M. Stumpf, L. Tombez, N. Bucalovic, V. Dolgovskiy, G. Di Domenico, D. Hofstetter, S. Pekarek, A. Oehler, T. Südmeyer, U. Keller, and P. Thomann, “Phase noise characterization of a near-infrared solid-state laser optical frequency comb for ultra-stable microwave generation,” in *Optical Clock Workshop, oral presentation*, (Torino, Italy), Dec. 2010.

# Contents

<b>1</b>	<b>Introduction</b>	<b>1</b>
<b>2</b>	<b>Radio frequency (RF) discriminators</b>	<b>7</b>
2.1	Introduction . . . . .	7
2.2	Frequency discriminators . . . . .	9
2.2.1	Analog phase-locked loop discriminator . . . . .	10
2.2.2	Miteq RF discriminator . . . . .	11
2.2.3	HF2PLL, digital phase-locked loop . . . . .	12
2.2.4	DXD200, digital phase detector . . . . .	13
2.3	Characterization of RF discriminators . . . . .	16
2.3.1	Sensitivity and bandwidth . . . . .	16
2.3.2	Frequency range . . . . .	19
2.3.3	Noise floor . . . . .	20
2.3.4	AM/AN cross-sensitivity . . . . .	22
2.4	Comparison of RF discriminators . . . . .	25
2.5	Application of RF discriminators . . . . .	31
2.6	Conclusion . . . . .	34
<b>3</b>	<b>The <math>\beta</math>-separation line and laser linewidth</b>	<b>37</b>
3.1	Introduction . . . . .	38
3.2	Theoretical background . . . . .	39
3.3	Experimental setup . . . . .	42
3.3.1	Laser sources . . . . .	43
3.3.2	Frequency noise PSD measurement . . . . .	45
3.3.3	Line profile measurement . . . . .	46



3.4	Results . . . . .	47
3.5	Conclusion . . . . .	50
<b>4</b>	<b>Ultra-stable optical reference</b>	<b>53</b>
4.1	Introduction . . . . .	53
4.2	Pound-Drever-Hall stabilization technique . . . . .	54
4.2.1	Theoretical model . . . . .	56
4.2.2	Linear regime near the cavity resonance . . . . .	59
4.3	Planar waveguide extended cavity laser . . . . .	62
4.4	Reference cavity housing . . . . .	65
4.5	Cavity thermal enclosure . . . . .	68
4.6	Thermal model of the cavity enclosure . . . . .	71
4.6.1	Thermal properties of the system components	72
4.6.2	Thermal dynamics and active temperature control . . . . .	75
4.7	Optical setup . . . . .	82
4.8	Closing the loop . . . . .	84
4.9	High finesse Perot-Fabry reference cavity . . . . .	87
4.9.1	Thermal noise limit . . . . .	88
4.9.2	Thermal expansion turning point . . . . .	89
4.9.3	Cavity drift . . . . .	91
4.9.4	FWHM resonance linewidth. Cavity ringdown time. . . . .	92
4.9.5	Direct resonance profile measurement . . . . .	94
4.10	Conclusion . . . . .	96
<b>5</b>	<b>Er:Yb:glass oscillator (ERGO) optical frequency comb</b>	<b>97</b>
5.1	Introduction . . . . .	97
5.2	75-MHz Er:Yb:glass ultra-fast laser . . . . .	100
5.3	Frequency comb stabilization . . . . .	101
5.4	Stabilized CEO beat properties . . . . .	102

5.5	Optical comb line properties . . . . .	107
5.6	CEO dynamics impact on stabilization . . . . .	109
5.7	Conclusion . . . . .	116
<b>6</b>	<b>Conclusion and outlook</b>	<b>119</b>



# List of Figures

2.1	Schematic representation of an analog PLL discriminator. . . . .	11
2.2	Difference between the ideal and actual response of the digital phase detector. . . . .	15
2.3	Amplitude and phase of the normalized transfer function of different discriminators. . . . .	18
2.4	Normalized sensitivity of the frequency discriminators as a function of the carrier frequency detuning. . . . .	20
2.5	Noise floor of different discriminators. . . . .	21
2.6	Cross-sensitivity of the discriminators to amplitude modulation and to amplitude noise. . . . .	24
2.7	Examples of a graphical representation of a frequency (phase) discriminator with different bandwidths. . . . .	26
2.8	Graphical comparison of the characteristics of different discriminators. . . . .	30
2.9	Frequency noise PSD of the CEO beat in the Er:Yb:glass frequency comb, measured with different discriminators. . . . .	33
3.1	Graphical representation of the simple approximation proposed to determine the linewidth of a laser from its frequency noise PSD. . . . .	41
3.2	The experimental setup for the test of the $\beta$ -separation line based linewidth approximation . . . . .	43
3.3	Representative examples of frequency noise PSDs and corresponding line shapes for three different laser systems. . . . .	48

3.4	Comparison between the approximate and the actual linewidth. . . . .	51
4.1	Pound-Drever-Hall concept of laser stabilization to a reference cavity. . . . .	56
4.2	The Pound-Drever-Hall error signal. . . . .	58
4.3	Schematics of the PLANEX <sup>TM</sup> technology based laser	62
4.4	ORION <sup>TM</sup> module. . . . .	63
4.5	Output power and frequency tuning of the PW-ECL with the injection current. . . . .	64
4.6	Frequency noise and linewidth of the PW-ECL. . . . .	65
4.7	Response of the PW-ECL to the injection current modulation. . . . .	66
4.8	LTF-ULE2 reference cavity housing. . . . .	67
4.9	LTF-ULE2 reference cavity thermal enclosure. . . . .	69
4.10	Cross-section of the vacuum chamber with the ULE cavity in place. . . . .	71
4.11	Equivalent electrical circuit of the cavity and its thermal enclosure . . . . .	72
4.12	Response of the model to a 1 K step in the screen temperature . . . . .	76
4.13	Experimental determination of the time constant of the heat exchange between the screen and the cradle. . . . .	77
4.14	Fast and slow temperature control loops. . . . .	78
4.15	Response of the thermal model to a change in the screen temperature, shaped by the additional slow loop. . . . .	79
4.16	The evolution of the temperatures, during a +1 K step in the ULE cavity temperature . . . . .	80
4.17	Temperature monitoring data during $\sim 25$ day period, showing peak-to-peak temperature variations of the ambient, the thermal screen and the cradle. . . . .	81
4.18	ORION <sup>TM</sup> laser stabilization to the LTF-ULE2 cavity. . . . .	82
4.19	The free-space part of the setup, used for the injection of light in the reference cavity. . . . .	83

4.20	Shapes of the transmission and error signals during laser frequency sweep. . . . .	86
4.21	Laser stabilization loop bandwidth. . . . .	87
4.22	LTF-ULE2 notched optical cavity. . . . .	88
4.23	Static determination of the temperature inversion point of the LTF-ULE2 reference cavity. . . . .	90
4.24	Measured cavity drift at zero CTE temperature. . . . .	92
4.25	Measurement of the ringdown time for the LTF-ULE2 cavity. . . . .	93
4.26	Setup for direct LTF-ULE2 cavity resonance shape measurement. . . . .	94
4.27	Resonance shape of the LTF-ULE2 cavity. . . . .	95
5.1	Layout of the diode-pumped Er:Yb:glass laser oscillator (ERGO). . . . .	100
5.2	Amplitude and phase of the CEO beat stabilization loop. . . . .	103
5.3	CEO beat stabilization loop. . . . .	104
5.4	Frequency noise PSD and linewidth of the free-running ERGO comb CEO beat. . . . .	105
5.5	Frequency noise PSD and residual integrated phase noise of the phase-locked CEO beat. CEO beat RF spectrum. . . . .	106
5.6	Time series and Allan deviation of the ERGO $f_{\text{CEO}}$ . . . . .	107
5.7	RF reference limiting the stability of the ERGO comb. . . . .	109
5.8	Static tuning curve of the CEO frequency $f_{\text{CEO}}$ with respect to the pump current. . . . .	111
5.9	Frequency noise power spectral density (PSD) of the CEO beat measured at two different pump currents. . . . .	112
5.10	Amplitude and phase of the dynamic response of the $f_{\text{CEO}}$ to pump current modulation measured at different pump currents. . . . .	114
5.11	Gain and phase of the overall CEO stabilization loop transfer function at the two different pump currents. . . . .	115

6.1 Radio signal of the Voyager 1 probe . . . . . 125

# List of Tables

2.1	Properties of the frequency/phase discriminators. . .	27
4.1	Physical characteristics of the materials used for the mechanical parts . . . . .	73
4.2	Dimensions and thermal capacities of the elements of the subsystem cavity - thermal enclosure. . . . .	74
4.3	Emissivities of the surfaces involved in the radiative heat exchange . . . . .	74
4.4	Thermal resistances between the elements of the cavity thermal enclosure. . . . .	75
4.5	Comparison of the thermal noise floors for two LTF reference cavities. . . . .	89





*If you want to find the secrets of the universe, think  
in terms of energy, frequency and vibration.*

*Nikola Tesla*



# Chapter 1

## Introduction

From the time of the first encounters with fire, through torches, candles, petroleum lamps, incandescent bulbs, gas tubes and finally by harnessing the stimulated emission, humans and human societies have undergone an irreversible development, becoming the masters of light. Fortunately, we cannot claim to be the masters of time, but the very basis of our biological existence has pushed us, throughout all of these ages, to measure the important intervals of time. The more refined and complex the global economy has become, the tinier the time intervals were becoming important. From the yearly cycles of the Nile floods, throughout the 18<sup>th</sup> century trade and ship navigation, all the way to the contemporary satellite based positioning and further, we should be decently proud on the fact that, what matters has changed by almost 20 orders of magnitude and we can count it all.

The field of time and frequency is positioned between the worlds of the fundamental physics and the electrical engineering, with its language and knowledge base derived from both sides. The concept of noise is not so much present in the minds of the physicists and the engineers are strongly in advantage when it comes to the real world applications of the principles. When these two sensibilities are combined, we come to the present situation, where the laser emission is approaching the idealized representation of almost zero linewidth spectral line. The joke says it, that for the time and frequency com-

munity the laser is "just a band passed noise". If there is a need for the light source of the highest spectral purity, the laser has to be additionally treated with some laboratory scale techniques, and that need exists at the current forefront of the science and technology.

In recent years we are all experiencing the rapid, good change of the world we live in, brought to existence by performance improvements of the various concepts, not only, but still in an important part relying on the development of the oscillators. More resolution for the navigation, more data packed in the existing communication channels, full and reliable coverage by mobile phone networks and many other activities, nowadays taken for granted, all of them profit from the low noise and high stability signal sources. These changes are influencing every single person on a daily basis.

In the domain of the fundamental research, where the nature of things allows for the use of tools in the development stage, and where frightening forests of cables, commercially unacceptable equipment shapes and forms usually bring the level of performance not accessible to the general public, the imagination and curiosity have their own satisfaction. Big cosmological questions can be brought down to Earth and examined by clock comparison. The tests of the theory of relativity were performed in the 1970s by comparison of the hydrogen masers [1] or microwave Cs atomic clocks [2]. New generation of the optical atomic clocks, operating at the THz frequencies, comes with the anticipated stability at least an order of magnitude better than in the case of their microwave predecessors and very recently, the Sr lattice clocks have surpassed the Cs fountain clocks in terms of the fractional frequency stability [3]. At the stability level lower than 1 in  $10^{16}$  [4], it is possible to detect the frequency gravitational red shift. The prediction made by the general theory of relativity can be tested by comparison of two identical clocks, placed at different gravitational potentials (heights). Furthermore, if two different optical clocks exhibit effects of the fundamental constants in a different manner, and if the difference in their frequencies are observed, that would mean that the constants of nature, are not constant at all.

Although we are moving towards THz domain, majority of our instruments are still working in the microwave range i.e. the optical frequencies cannot be directly measured. For decades, the measurement of the optical frequencies was a cumbersome task, involving too complicated, too expensive harmonic frequency chains, on top of all limited to pre-selected optical frequencies. For some time, the science was stuck, applying the brute force, until the breakthrough was made in the understanding of the functioning of the ultra-fast mode-locked lasers. Femto-second pulses are formed as a result of the simultaneous, phase-locked oscillation of thousands of the laser cavity modes. This comb-like structure in the frequency domain can be controlled by stabilization of only two degrees of freedom, the repetition rate of the laser, defined by the cavity length, and the offset between the pulse envelope and the underlying carrier field, both of them in the microwave domain. All of a sudden an optical frequency ruler was available, rendering useless few of the frequency chains ever constructed and bringing the optical frequency measurement on a table top.

I joined Laboratoire Temps-Fréquence (LTF, Institute of Physics, University of Neuchâtel) in the beginning of 2010, as a part of the optical frequency metrology group. In this thesis I will try to reflect on my activities in a few logically distinctive sections.

Chapter 2 presents the characterization of various radio (RF) frequency or phase discriminators [5]. The frequency discriminator technique is used for the demodulation of the microwave signals, which brings the noise components down to the baseband for the analysis. Once all of the properties of the frequency (phase) discriminators were examined, a collection of these frequency-to-voltage converters could have been used as the basic tools for the measurements of the noise in the narrow heterodyne optical beat signals. The measurement of the noise of the carrier-envelope offset (CEO) beat frequency of the optical frequency comb is used as an example of the application of the frequency discriminator technique.

A few years ago, a simple approximation was proposed that en-

ables easy calculation of the laser linewidth from its frequency noise power spectral density (PSD) [6]. A line in the frequency noise PSD, named  $\beta$ -separation line, divides the noise spectrum in two distinctive parts. The surface of the spectrum that corresponds to the slow carrier modulation is used for the approximate calculation of the linewidth. The experimental validation of that approximation is the subject of the Chapter 3. Optical heterodyne beat signals from different sources are used as test signals. Their frequency noise is measured by the frequency discriminator technique and the comparison is made between the linewidth calculated by the proposed approximation and the directly measured linewidth [7].

The building and the characterization of the horizontal, ultra-stable, high-finesse, 10 cm long Perot-Fabry reference cavity is presented in Chapter 4. This is the second such system in our laboratory. The mechanical layout of this system has been adjusted for the possible transportation in the future. The low-noise planar waveguide extended cavity laser (PW-ECL) is stabilized to the passive reference cavity by the Pound-Drever-Hall technique. The thermal model of the cavity enclosure has been developed, which led to a significant improvement in the cavity temperature control. Although the reference cavity is strongly thermally shielded, it is possible to force the change of its temperature within two and a half days to a new set point. Therefore, it was possible to determine the temperature of the zero expansion of the cavity from a set of discrete frequency measurements.

In Chapter 5 the focus is on the noise properties of a novel type of the ultra-fast laser, a diode-pumped solid-state laser (DPSSL). It is based on the Er:Yb:glass (ERGO) gain material, while the passive mode-locking is achieved by the use of the semiconductor saturable absorber mirror (SESAM). This technology combines good characteristics of the classic solid state ultra-fast lasers like Ti:sapphire (high Q cavity, low noise operation), with the convenience of the diode pumping, characteristic for the fiber lasers. In this configuration, the record narrow free-running carrier-envelope offset (CEO)

beat of only  $\sim 4$  kHz has been reported [8], and the full frequency comb stabilization was achieved [9]. The CEO beat frequency of this frequency comb is changing with the pump laser power and it has a maximum at some point. The dynamics of the CEO beat has been examined at both sides of this reversal point, together with its influence on the possibility of the frequency comb stabilization [10].

The main motivation for the development of the ultra-narrow optical reference is the generation of the ultra-stable microwave signal that could be used for the characterization of the continuous cold Cs atom fountain (FOCS-2) [11]. The high spectral purity microwave signal can be generated through the coherent division of the optical reference signal, using an optical frequency comb as a frequency divider. Although I have described all of the elements necessary for the realization of such an experiment, the all-optical microwave generation is out of the scope of this thesis. Nevertheless, recently we successfully implemented the scheme where we phase-locked one of the teeth of the ERGO frequency comb to the cavity-stabilized laser. The extracted microwave signal was characterized by comparison with the transportable cryogenic sapphire oscillator (ULISS, Femto-ST, Besançon, France) [12, 13].





# Chapter 2

## Radio frequency (RF) discriminators

This chapter represents a description of a radio-frequency (RF) discriminator (frequency-to-voltage converter), based on an analog phase locked loop (PLL), whose intended use is the analysis of the noise properties of narrow-spectrum heterodyne beat signals. This type of frequency discriminator is based on a voltage-controlled oscillator (VCO), phase-locked to the signal under test. The control voltage that drives the VCO reflects the frequency fluctuations of the input signal and thus corresponds to the frequency noise of e.g. a heterodyne optical beat signal between two lasers or between a laser and an optical frequency comb (OFC). Furthermore, the properties of this discriminator are compared with three other commercially available devices. Depending on the signal under test, each of the examined discriminators represents the essential tool in all of the subsequent noise studies.

### 2.1 Introduction

Atomic physics, high resolution spectroscopy, optical heterodyne communication and many different fields of basic science and technology, nowadays routinely utilize narrow-linewidth and highly stable

lasers. Recent years have seen an interesting development in frequency metrology, with the advent of the optical atomic clocks, being superior in terms of stability to the best microwave primary frequency standards [14]. This activity, at the same time has motivated the development of a new generation of ultra-stable lasers, exhibiting linewidths at the hertz level or even better [15, 16], with one of the common methods for laser stabilization (e.g. of an extended cavity diode laser (ECDL) [17]) being the locking to an external reference (Perot-Fabry cavity or atomic/molecular transition).

One way to describe the spectral properties of a laser is by its optical line shape and the corresponding linewidth, usually full width at half maximum (FWHM) of the line shape. Laser linewidth can be directly determined by self-homodyne/heterodyne interferometry using long fiber delay lines [18], which is not practical in case of the ultra-narrow lasers because of their long coherence length and the extreme fiber lengths that would be needed. Heterodyning with another similar laser or with a reference source of a narrower profile is the usual approach that brings the analysis down to radio-frequency (RF) range.

While the optical linewidth is convenient as a single number used for rough comparison of different lasers, it brings little information about the spectral distribution of the laser noise, which is important for the identification of the sources of the external laser perturbations [19]. Furthermore, the common frequency noise characteristics of a free-running laser with flicker noise diverging at low frequencies, leads to an observation time dependent linewidth, making it thus improper as a figure of merit of the laser spectral properties.

A full insight into the noise processes affecting the laser is only possible by the measurement of its frequency noise power spectral density (PSD). In the efforts to stabilize a laser, the knowledge of its free-running frequency noise PSD is necessary for the determination of the servo-loop bandwidth [6], while, once stabilized, the laser has to be characterized in terms of the residual frequency (phase) noise as well.

In this part of the thesis, I will present a frequency discriminator that was developed for the measurement of the frequency noise of a radio-frequency (RF) heterodyne beat signals. A detailed characterization includes the discriminator sensitivity, its bandwidth and noise floor. These results are compared with different commercially available discriminators.

## 2.2 Frequency discriminators

The noise power spectral density gives a full representation of the noise processes connected with a particular physical quantity. The actual measurement usually consists of the spectral analysis of the voltage fluctuations. Depending on the physical quantity of interest, there has to be a means of converting its fluctuations into voltage fluctuations. In case of the examination of the frequency of a signal, a frequency-to-voltage converter i.e. a frequency discriminator is a crucial part of the experimental setup.

Devices with frequency-dependent transmission, such as gas-filled cells [20–23], Perot-Fabry resonators [24] or unbalanced two-beam interferometers [25] are used as frequency discriminators in the optical domain. By monitoring fluctuations of the optical intensity of the transmitted signal, any fluctuation in the optical frequency is directly transformed into measurable intensity variations and then into the electrical signal by a photodiode.

The frequency range of an optical frequency discriminator is usually restricted and if the laser of interest lies out of that range, a heterodyne beat with another laser can be used to down-convert the signal to the radio-frequency (RF) domain, where it can be examined using the an RF frequency discriminator. If the second laser is similar to the laser under test, both lasers contribute equally to the noise of the RF beat and the frequency noise PSD of the beat signal is at most two times higher than that of a single laser. If the noise of the reference laser is negligible, the frequency noise PSD of the laser under test is directly obtained from the analysis of the RF beat.

The sensitivity (or discriminator slope  $D_\nu$  in  $[\frac{\text{V}}{\text{Hz}}]$ ) is the main characteristics of a frequency discriminator, representing its ability to convert frequency fluctuations  $\delta\nu(t)$  of the input signal into the output voltage variations  $\delta V(t)$ . The higher the discriminator slope  $D_\nu$ , the better the frequency noise conversion. The frequency noise PSD of the input signal ( $S_{\delta\nu}(f)$  in  $[\frac{\text{Hz}^2}{\text{Hz}}]$ , where  $f$  is the Fourier frequency) is calculated from the PSD of the output voltage ( $S_V(f)$  in  $[\frac{\text{V}^2}{\text{Hz}}]$ ) by

$$S_{\delta\nu}(f) = \frac{S_V(f)}{D_\nu^2}. \quad (2.1)$$

The principle of operation of different RF discriminators will be given in the following subsections, whereas their characterization and comparison will be presented in separate sections.

### 2.2.1 Analog phase-locked loop discriminator

The analog PLL frequency discriminator was built as a follow-up of the work of Turner et al. [19]. The basic principle of this discriminator is to phase-lock a voltage-controlled oscillator (VCO) to the RF beat signal to be analyzed, using a high-bandwidth PLL. If the loop bandwidth is sufficient, the VCO follows any frequency fluctuations  $\delta\nu(t)$  of the input RF beat and the control voltage of the VCO  $\delta V(t)$  reflects the frequency fluctuations of the input signal. Once the response of the VCO is known (in  $[\frac{\text{Hz}}{\text{V}}]$ ), the fluctuations of the control voltage can be directly converted into frequency fluctuations of the input RF beat (within the loop bandwidth). While Turner et al. used a single integrated circuit PLL for their frequency discriminator, the PLL discriminator described here is built using discrete off-the-shelf analog components (VCO, phase detector and servo controller). This approach offers a larger flexibility in the adjustment of the PLL parameters (gain and bandwidth), which enables the optimization of the PLL characteristics with respect to the properties of the signal under test (e.g., to achieve the largest bandwidth or the

lowest noise floor). A scheme of the PLL discriminator is shown in Figure 2.1. The VCO (Mini-Circuits ZX95-209-S+) operates in the 199–210 MHz range, with a nominal tuning coefficient of  $1.5 \frac{\text{MHz}}{\text{V}}$ . A double-balanced mixer (Mini-Circuits ZP-1LH) is used as a phase detector, followed by a 10-MHz low-pass filter to suppress high frequency components. Finally, the loop is closed with a high-speed servo controller (New-Focus LB1005-S) with a proportional-integral (PI) corner frequency adjustable from 10 Hz up to 1 MHz and a proportional gain between  $-40$  dB and  $+40$  dB.

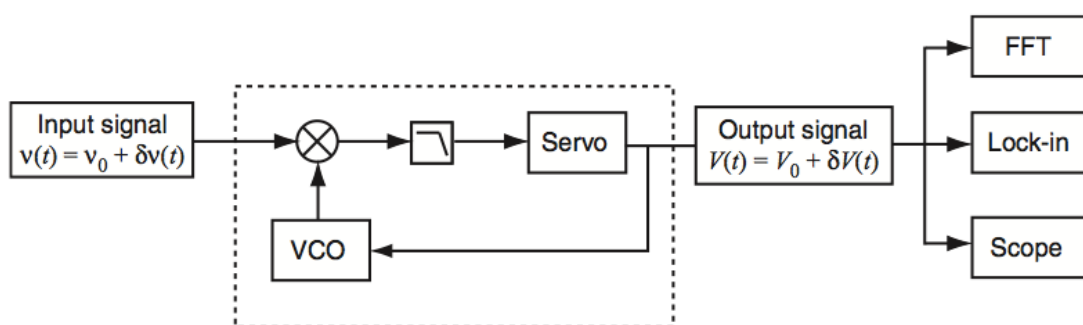


Figure 2.1: Schematic representation of an analog PLL discriminator. The control voltage  $\delta V(t)$  of the VCO constitutes the output signal that replicates the input frequency variations  $\delta \nu(t)$ . This signal is analyzed using an oscilloscope, a lock-in amplifier or an FFT analyzer.

## 2.2.2 Miteq RF discriminator

Simple plug-and-play RF discriminators are commercially available in different frequency ranges from various suppliers of radio-frequency components. One such device is Miteq FMDM 21.4/2-4, operating in the range of 18–26 MHz with a typical peak-to-peak bandwidth of 8 MHz and a linear bandwidth of 4 MHz, as specified by the manufacturer ([www.miteq.com](http://www.miteq.com)). The operation of this discriminator is based on the use of an input limiting amplifier to drive two staggered tuned L-C circuits. Opposing rectification of the circuits creates the discriminator "S" curve and a video amplifier is finally utilized to provide adequate output slope. The ability to precisely align the

skirts of the tuned circuits, which represents the discriminator linear bandwidth, is an advantage of this type of design. The nominal response of this discriminator is  $1 \frac{\text{V}}{\text{MHz}}$ .

### 2.2.3 HF2PLL, digital phase-locked loop discriminator

The HF2LI from Zurich Instruments, Switzerland, is an all-digital instrument consisting of a dual input digital lock-in amplifier extended with dual PLL capabilities ([www.zhinst.com](http://www.zhinst.com)). The lock-in amplifiers have a frequency bandwidth ranging from  $1 \mu\text{Hz}$  to  $50 \text{ MHz}$  (with a sampling rate of  $210 \frac{\text{MSa}}{\text{s}}$ ), a dynamic reserve of  $120 \text{ dB}$  and an input voltage noise of  $5 \frac{\text{nV}}{\sqrt{\text{Hz}}}$ . The instrument is based on a field-programmable gate array (FPGA) which permits computations with large numerical precision and short processing time. Moreover, the lock-in shortest integration time constant of  $800 \text{ ns}$ , lower by one order of magnitude than in other commercially available lock-in amplifiers, makes it suitable for wide bandwidth demodulation and as a phase detector for a PLL (referred to as HF2PLL) that replaces all the analog components in the dotted box in Figure 2.1 by their numerical counterparts.

The HF2PLL runs directly on the lock-in FPGA, ensuring a precise control of the PLL dynamics and resulting in a maximum  $-3 \text{ dB}$  bandwidth of  $60 \text{ kHz}$ . The HF2PLL has similar functional blocks as the analog PLL described in Subsection 2.2.1, with two notable differences:

- The phase detector makes use of the lock-in demodulation chain (including its low pass filters) since its purpose is to determine the phase difference between input and reference signals. This phase difference is the lock-in output channel  $\theta$ , as calculated directly from the quadrature (Y) and in-phase (X) components of the demodulated signal. The advantage of this approach compared to the analog PLL is its high rejection of

amplitude modulations of the input signal, thereby minimizing the amplitude noise sensitivity of the HF2PLL discriminator.  $\theta$  is the error signal and constitutes the input of the following numerical proportional-integral-derivative (PID) controller, as in the analog case.

- The VCO is replaced by a functionally equivalent numerical controlled oscillator (NCO), whose role is to keep track of the reference signal phase (from which the in-phase and quadrature reference signals are derived). The rate at which the NCO phase changes, which is the reference signal instantaneous frequency, is  $f(t) = f_c + dF$ , where  $f_c$  is a selectable PLL center frequency and the frequency deviation  $dF$  (in Hz) is the PID controller output. When the HF2PLL discriminator is used to characterize a heterodyne beat signal,  $dF$  is output as an analog signal with a software-selected gain (from  $0.75 \frac{\text{nV}}{\text{Hz}}$  to  $1.6 \frac{\text{V}}{\text{Hz}}$ ).

In comparison with the analog PLL where all electronic components suffer from  $1/f$  and white noise, the noise sources in the digital PLL are confined to the analog-to-digital converter at the lock-in input stage and to the analog  $dF$  output, since the numerical noise can be made arbitrarily small by increasing the internal numerical precision. On the other hand, the measurement bandwidth of analog PLLs is usually larger than that of their digital counterparts.

#### 2.2.4 DXD200, digital phase detector

A digital phase detector with a wide linear range of operation is used for the stabilization of the CEO beat [9] of two frequency combs currently operating in our laboratory. Its purpose is to detect the phase fluctuations between the CEO beat and the reference signal, in order to generate the error signal for the stabilization loop. This digital phase detector (DXD200 module from MenloSystems, Germany, which is a part of the XPS800 femtosecond phase stabilization unit)



has also been used as a diagnostic tool to measure small frequency fluctuations between the signal under test and the reference signal and has been characterized for comparison with the other frequency discriminators.

The basic element of this digital phase detector is a differential period counter, where the reference signal counts up and the RF beat signal counts down [26]. The counter has a range from 0 to 64 and is initialized at 32. The phase error can track a  $\pm 32 \times 2\pi$  phase difference between the two signals. The counter signal is then fed into a digital to analog converter to generate a signal proportional to the relative phase, with a nominal phase discrimination factor  $D_\varphi = \frac{3.3\text{V}}{32 \times 2\pi} = 0.016 \left[ \frac{\text{V}}{\text{rad}} \right]$ .

While this detector should provide an ideal linear response in a phase range of  $\pm 32 \times 2\pi$ , this is not the case in reality due to the presence of several nonlinearities in its range of operation. This effect was investigated over the entire range of operation of the phase detector by comparing two signals with a slightly different frequency ( $f_1 = f_{\text{ref}} = 20$  MHz,  $f_2 = f_1 + \Delta$ , with  $\Delta$  in the range of 10-100 mHz), in order to slowly scan the output voltage (phase difference resulting from the accumulated phase shift between the two signals). Some of the nonlinearities are directly observable in the DC output voltage of the phase detector (see Figure 2.2(a)). Furthermore, a small frequency modulation (at a rate  $f_{\text{mod}} = 10$  kHz, with a span of  $\Delta f = 50$  Hz) was applied to one of the 20-MHz carriers in order to measure the frequency response (in amplitude and phase) of the phase detector using a lock-in amplifier and to subsequently determine the detector sensitivity (in  $\left[ \frac{\text{V}}{\text{rad}} \right]$ ), as also described in the following Section 2.3. In order to be able to resolve the narrow peaks that occur at some specific points in the detector response as a result of the nonlinearities, a small modulation index  $\beta = (\frac{\Delta f}{2})/f_{\text{mod}}$  was used. In that case, the measured lock-in signal corresponds to the derivative of the phase detector response and the sensitivity was obtained by normalizing this signal by the modulation depth  $\beta$ . The outputs of the lock-in amplifier (X and

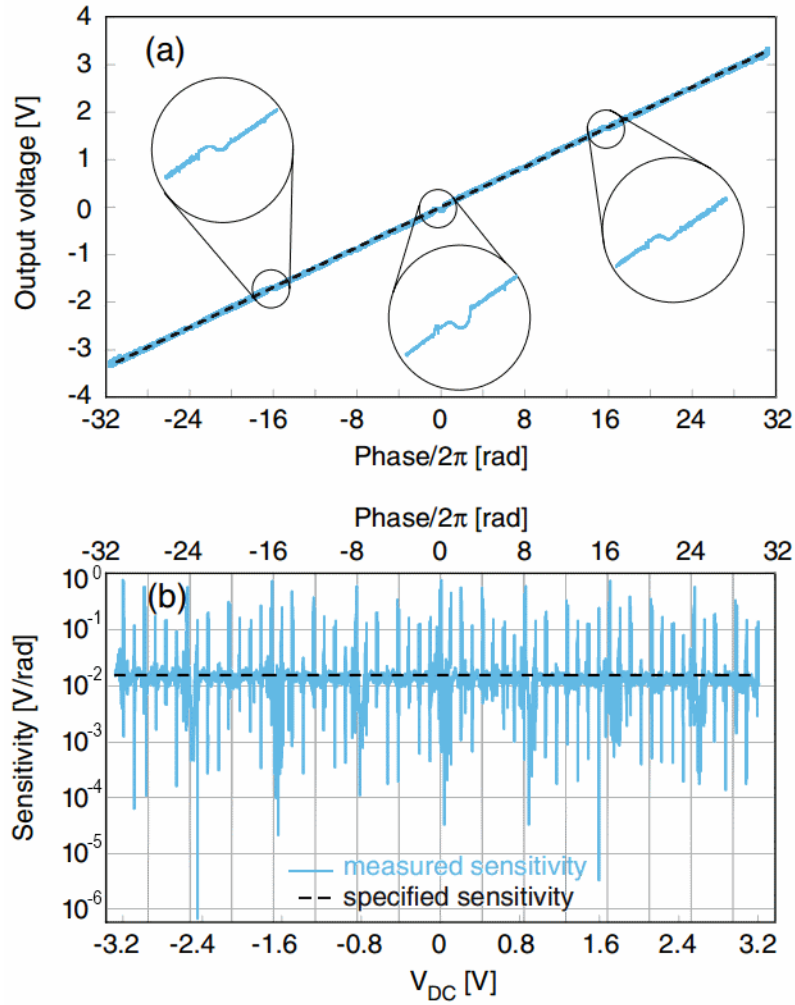


Figure 2.2: Difference between the ideal (dashed line) and actual (light thick curve) response of the digital phase detector. (a) DC analog output voltage as a function of the phase difference between the two inputs; some nonlinearities are visible at the encircled points. (b) Highlight of the nonlinearities of the detector occurring roughly every  $2\pi$  phase difference. This curve has been obtained by applying a frequency-modulated carrier at one input of the device and performing lock-in detection at the output to determine the discriminator sensitivity. The dashed line corresponds to the average slope of the DC curve (a).

Y components) were recorded with an acquisition card (National Instruments NI USB-6008), together with the phase detector operating DC voltage, during a phase sweep. The actual response displayed in

Figure 2.2(b) is not as smooth as expected and shows the presence of many nonlinearities, regularly separated by a  $2\pi$  phase difference. At these points, the sensitivity of the detector for small signals can be locally enhanced by a factor up to 50 ( $0.8 \left[\frac{\text{V}}{\text{rad}}\right]$ ). In order to have a proper discriminator of known sensitivity, the digital phase detector should be operated at a point where its response is constant, i.e., away from the nonlinear points. All the results shown in the following sections are obtained in such conditions. Finally, we should notice that the DXD200 acts as a phase discriminator. The voltage noise PSD at its output is equal to the phase noise PSD or frequency noise PSD multiplied by the square of the corresponding sensitivity

$$S_{\delta V}(f) = D_{\nu}^2(f)S_{\delta\nu}(f) = D_{\varphi}^2(f)S_{\delta\varphi}(f) \quad (2.2)$$

The relation between the frequency noise and phase noise PSD is given by [27]

$$S_{\delta\nu}(f) = f^2 S_{\delta\varphi}(f) \quad (2.3)$$

which finally gives the expression for the frequency sensitivity of the phase discriminator as

$$D_{\nu}(f) = \frac{D_{\varphi}(f)}{f}. \quad (2.4)$$

## 2.3 Characterization of RF discriminators

### 2.3.1 Sensitivity and bandwidth

The sensitivity of each discriminator has been determined by applying a frequency modulated input signal with a modulation depth  $\Delta f = 1$  kHz ( $\Delta f = 100$  Hz in the case of the digital phase detector DXD200) at a varying modulation frequency  $f_{\text{mod}}$ , using a calibrated, high-bandwidth reference voltage-controlled oscillator (VCO).

A 207 MHz carrier frequency was used with the analog PLL discriminator and a 20-MHz carrier frequency with the other discrimi-

nators, obtained by mixing the 207-MHz VCO signal with a 227-MHz reference signal and subsequent low-pass filtering. The modulation frequency  $f_{\text{mod}}$  was scanned in the range from 0.1 Hz to 10 MHz and the demodulated output signal of the discriminators was measured in amplitude and phase using a lock-in amplifier referenced to  $f_{\text{mod}}$  (standard lock-in, model Stanford Research Systems SR830, up to 100 kHz and RF lock-in, model SR844 at higher frequencies). Finally, the transfer function of each device was obtained by normalizing the lock-in output signal to the input frequency modulation depth  $\Delta f$ . The bandwidth of a discriminator is defined here as the frequency range in which the discriminator sensitivity remains within  $\pm 10\%$  ( $\pm 0.9$  dB) of its value at  $f_{\text{mod}} = 1$  kHz. The sensitivities (or discriminator slopes, in  $[\frac{\text{V}}{\text{Hz}}]$ ) reported throughout this chapter are generally given for the discriminator output connected to a high impedance load. The only exception concerns Miteq discriminator, used with a  $93\text{-}\Omega$  load as specified by the manual.

The amplitude and phase of the transfer function of each discriminator are displayed in Figure 2.3. The result for the analog PLL is shown for a maximum PI corner frequency of 1 MHz and a PI gain adjusted to optimize the PLL operation. The response of the analog PLL slightly depends on the PLL settings (gain and PI-corner) in a sense that the low frequency sensitivity is unaffected by the PLL parameters, but at high frequency, the position and amplitude of the oscillation (servo bump) varies with these parameters. The analog PLL has a typical bandwidth of 200 kHz (defined at  $\pm 0.9$  dB as mentioned before) with a discriminator slope of  $0.7 \frac{\text{V}}{\text{MHz}}$ . The Miteq discriminator has the largest bandwidth of 2 MHz with a discriminator slope of  $1.25 \frac{\text{V}}{\text{MHz}}$ , obtained for 0 dBm input signal, but this sensitivity significantly depends on the signal amplitude (e.g., it is reduced to  $0.86 \frac{\text{V}}{\text{MHz}}$  at  $-6$  dBm input signal). The HF2PLL has a lower bandwidth of 50 kHz, but its sensitivity is much higher and can be adjusted by software in the range from  $0.75 \frac{\text{nV}}{\text{Hz}}$  to  $1.6 \frac{\text{V}}{\text{Hz}}$ . For the Miteq and analog PLL discriminators, an instantaneous response to frequency fluctuations is obtained up to  $f_{\text{mod}} > 100$  kHz, while

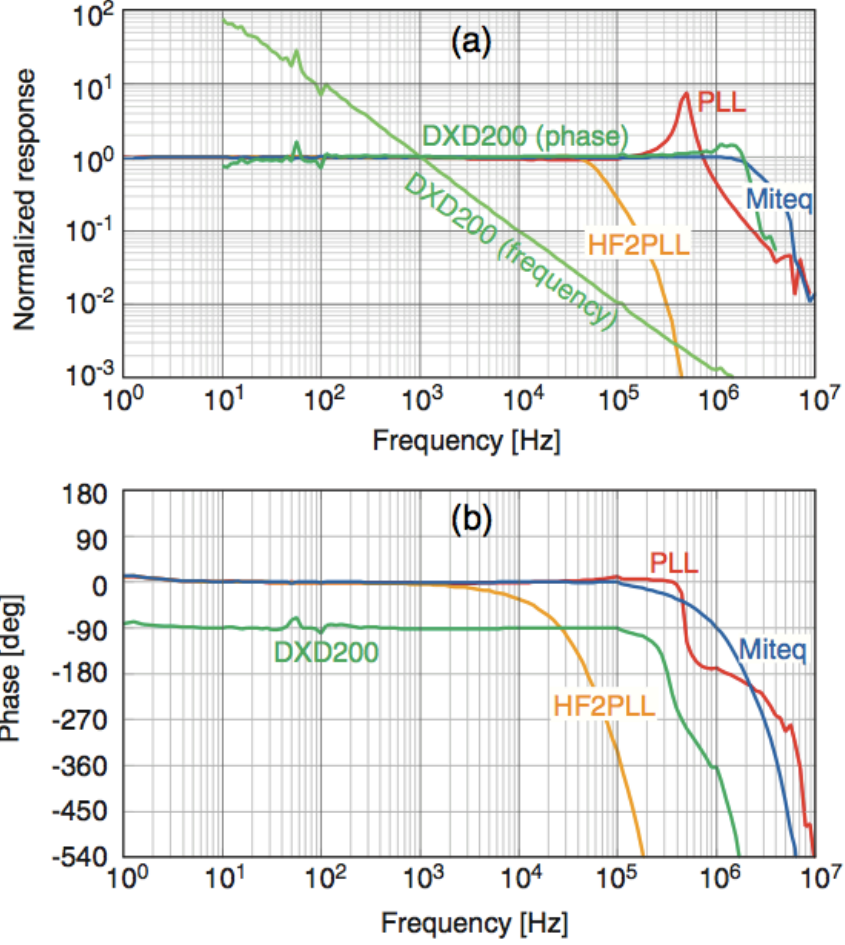


Figure 2.3: Amplitude (a) and phase (b) of the normalized transfer function of different discriminators, measured by applying a frequency-modulated input carrier and performing lock-in detection of the discriminator demodulated signal. Each transfer function has been normalized by the discriminator sensitivity measured at 1 kHz modulation frequency ( $D_{\nu}^{\text{PLL}} = 7 \times 10^{-7} [\frac{\text{V}}{\text{Hz}}]$ ,  $D_{\nu}^{\text{Miteq}} = 1.25 \times 10^{-6} [\frac{\text{V}}{\text{Hz}}]$ ,  $D_{\nu}^{\text{HF2PLL}} = 10^{-3} [\frac{\text{V}}{\text{Hz}}]$ ,  $D_{\nu}^{\text{DXD200}} = 1.8 \times 10^{-5} [\frac{\text{V}}{\text{Hz}}]$  or  $D_{\varphi}^{\text{DXD200}} = 1.8 \times 10^{-2} [\frac{\text{V}}{\text{rad}}]$ ). The amplitude response of the digital phase detector DXD200 is represented both in terms of response to frequency and phase modulation.

a significant phase shift is introduced at higher frequencies. In the HF2PLL, the phase shift occurs at much lower frequency, which is compatible with the amplitude attenuation. The sensitivity of the digital phase detector DXD200 decreases as  $1/f$ , since the module

acts as a phase comparator. The measured phase discriminator is around  $0.018 \frac{\text{V}}{\text{rad}}$  ( $0.016 \frac{\text{V}}{\text{rad}}$  expected from specifications, corresponding to  $D_\varphi = \frac{3.3\text{V}}{32 \times 2\pi}$ ). The phase detector introduces a  $-90^\circ$  phase shift at low Fourier frequency as it acts as a phase detector, while its response is being assessed in terms of frequency. At Fourier frequencies higher than 100 kHz, a significantly larger phase shift appears. The  $\pm 0.9$  dB bandwidth of DXD200 is  $\sim 1$  MHz.

### 2.3.2 Frequency range

The total frequency range of each discriminator is defined here as the frequency interval in which the discriminator operates. At the same time, the linear frequency range is considered to be the frequency interval in which the response is within  $\pm 10\%$  ( $\pm 0.9$  dB) of the discriminator sensitivity determined in previous Subsection 2.3.1. The frequency range of each discriminator, measured at 1 kHz modulation frequency, is shown in Figure 2.4. Both the analog PLL and the Miteq discriminator have a wide linear frequency range of several megahertz (7 MHz for the analog PLL and 9 MHz for Miteq). For the numerical PLL, the situation is different. The input carrier frequency can be anywhere in the range of  $\sim 1 - 49$  MHz, but the amplitude of the maximum detectable frequency fluctuations around this carrier depends on the selected sensitivity of the demodulator output. As the analog output of the HF2LI instrument is limited to  $\pm 10$  V, the maximum frequency fluctuation  $\Delta f_{\text{max}}$  which can be measured for a sensitivity  $D_\nu$  (in  $[\frac{\text{V}}{\text{Hz}}]$ ) is  $\Delta f_{\text{max}} = \pm \frac{10\text{V}}{D_\nu}$ . While a high sensitivity can be selected with the HF2PLL instrument, the drawback is the reduced frequency range.

Finally, the digital phase detector DXD200 can operate at any carrier frequency between 0.5 MHz and more than 200 MHz (provided that a reference signal at the same frequency is available), but the range of detectable fluctuations is limited to  $\pm 64\pi$  in terms of phase and is thus extremely narrow.

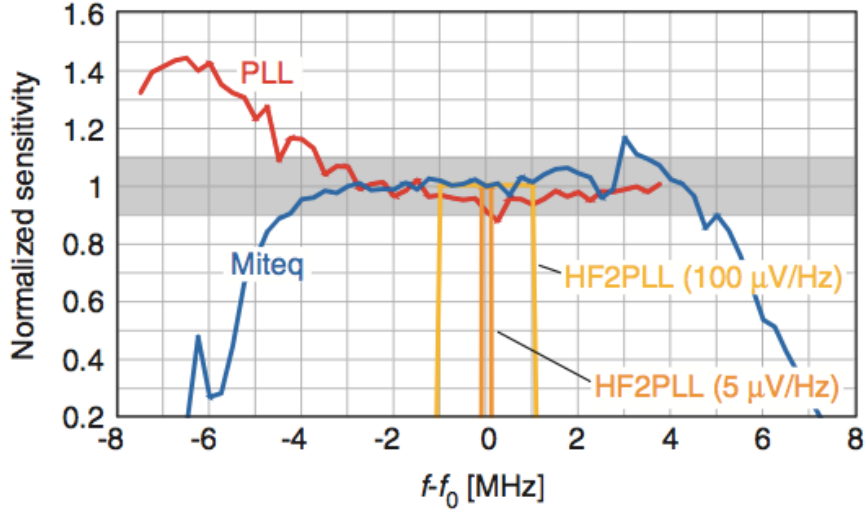


Figure 2.4: Normalized sensitivity of the frequency discriminators (measured for 1 kHz modulation frequency) as a function of the carrier frequency detuning. The gray area indicates the linear frequency range  $\Delta f_{\text{lin}}$  of each discriminator, defined as the frequency interval for which the discriminator response differs by less than  $\pm 10\%$  ( $\pm 0.9$  dB) from its nominal sensitivity. The frequency range of the HF2PLL is inversely proportional to the software-selected sensitivity  $D_\nu$  ( $\Delta f_{\text{lin}} = \pm \frac{10V}{D_\nu}$ ) and is shown here for two particular cases ( $D_\nu = 100 \frac{\mu V}{\text{Hz}}$  and  $D_\nu = 5 \frac{\mu V}{\text{Hz}}$ ) as an illustration.

### 2.3.3 Noise floor

A relevant characteristic of a frequency discriminator is its noise floor, which represents the smallest detectable frequency fluctuations with a signal-to-noise ratio of one. The noise floor of the different discriminators was measured with an FFT analyzer for Fourier frequencies up to 100 kHz and with an electrical spectrum analyzer at higher frequencies, when a stable, low-noise carrier was applied to the input. As previously, a 207 MHz carrier was used with the analog PLL discriminator and a 20 MHz carrier frequency with the other discriminators. The PSD of the discriminators output voltage has been converted into frequency noise PSD using the corresponding sensitivities previously determined. The results are shown in Figure 2.5.

The noise floor of the analog PLL-discriminator significantly de-

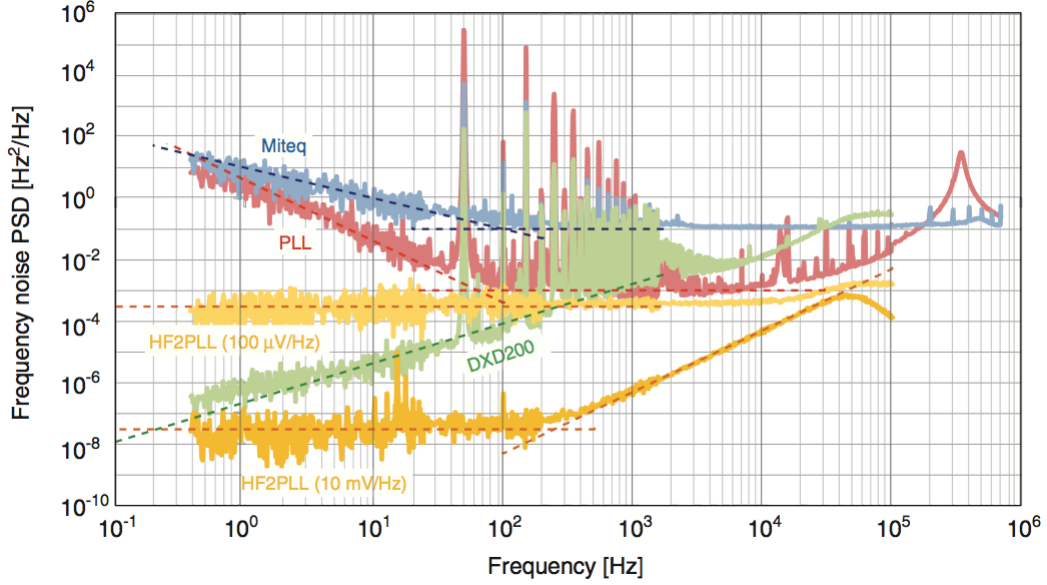


Figure 2.5: Noise floor of different discriminators. All of the measurements were made with the 20 MHz carrier, except for the analog PLL where the 207 MHz carrier was used. The noise floor of the analog PLL depends on the PI gain and is presented here in an optimized configuration. The white frequency noise of the HF2PLL (at low frequencies) results from white noise at the analog output and thus scales as  $\frac{1}{D_\nu^2}$  for sensitivities up to  $D_\nu = 10 \frac{\text{mV}}{\text{Hz}}$ . It is displayed here for two cases,  $D_\nu = 100 \frac{\mu\text{V}}{\text{Hz}}$  and  $D_\nu = 10 \frac{\text{mV}}{\text{Hz}}$ . The dashed lines represent an approximation of the noise floor of each discriminator in terms of a power series of  $f$  ( $f^{-2}$ ,  $f^{-1}$ ,  $f^0$ ,  $f^1$  and  $f^2$ ).

depends on the amplitude of the input signal and on the gain settings of the PI controller. It is presented here for a PI gain adjusted to optimize the noise floor. Operation at too high gain may increase the noise floor by one or two orders of magnitude at Fourier frequencies above 10 Hz. In the range of 100 Hz to 10 kHz, a white frequency noise floor is observed ( $\sim 10^{-3} \frac{\text{Hz}^2}{\text{Hz}}$ ). Out of this range, the noise floor scales as  $f^{-2}$  at low frequencies, resulting from the VCO white frequency noise that is multiplied by  $f^{-2}$  due to the Leeson effect [28] and linearly with  $f$  at high frequencies, resulting from the PLL servo bump.

The noise floor of the Miteq discriminator is white frequency noise



at frequencies  $f > 100$  Hz ( $\sim 0.1 \frac{\text{Hz}^2}{\text{Hz}}$ ) and increases as  $1/f$  at lower frequencies. The digital phase detector DXD200 has a typical  $1/f$  phase noise floor, which translates into a small frequency noise floor at low Fourier frequencies ( $< 10^{-5} \frac{\text{Hz}^2}{\text{Hz}}$  at 10 Hz). The frequency noise floor increases with  $f$  with a slope slightly larger than unity in a log-log plot (the experimentally observed dependence is  $f^\alpha$  with  $\alpha \approx 1.3$ ), and surpasses the noise floor of the two prior frequency discriminators at Fourier frequencies over 1 kHz (compared to the analog PLL discriminator) or 30 kHz (compared to Miteq). The noise floor of the HF2PLL has two contributions i.e. white frequency noise at low Fourier frequencies and white phase noise at high frequencies. The white frequency noise floor results from white noise in the analog port that outputs the frequency deviation  $dF$ . When converted into an equivalent frequency noise using the discriminator sensitivity, this leads to a frequency noise floor that depends on the selected sensitivity  $D_\nu$  and which scales as  $\frac{1}{D_\nu^2}$  for  $D_\nu$  below  $D_\nu = 10 \frac{\text{mV}}{\text{Hz}}$ . For higher sensitivities, the frequency noise floor starts to increase again due to the other noise contributions. The lowest noise floor is about  $3 \times 10^{-8} \frac{\text{Hz}^2}{\text{Hz}}$ , obtained for  $D_\nu = 10 \frac{\text{mV}}{\text{Hz}}$ . On the other hand, the white phase noise ( $\sim 5 \times 10^{-13} \frac{\text{rad}^2}{\text{Hz}}$ ) at high frequencies is due to the white noise at the input port of the HF2LI lock-in and is thus insensitive to the PLL output gain. The HF2PLL has the lowest noise floor in the frequency range from 1 Hz to 50 kHz.

### 2.3.4 AM/AN cross-sensitivity

An ideal frequency discriminator should be sensitive to frequency modulation (FM) or frequency noise (FN) only and insensitive to amplitude modulation (AM) or amplitude noise (AN). However, the situation is different in a real device and the cross-sensitivity of each discriminator has been investigated, both in terms of AM and AN. In the first case, a pure AM signal was applied to the input of the discriminator (with the AM depth ranging from 10% to 100% depending on the discriminator) and the output signal was measured

using a lock-in amplifier. In the second case, white AN was added at the input of the discriminators and the output voltage PSD was recorded using an FFT analyzer. The sensitivity of each discriminator (in  $[\frac{V}{Hz}]$ ) was used to convert the measured AM (AN) response into an equivalent FM (FN) signal. Then, an AM-to-FM (AN-to-FN) conversion factor (in  $[\frac{Hz}{\%}]$ ) was determined for each discriminator by normalizing the measured equivalent frequency response by the applied AM or AN (the latter was separately measured using a power detector, model Mini-Circuits ZX47-55LN-S+).

Figure 2.6 shows that all discriminators have some cross-sensitivity to AM and AN, the magnitude of which is being very similar in both cases. The analog PLL and the DXD200 show a similar AM (AN) sensitivity, which increases approximately linearly with the modulation frequency, meaning that these discriminators are more sensitive to fast AM (AN). The general trend is similar for HF2PLL, but the AM (AN) sensitivity is two orders of magnitude weaker. Miteq discriminator has by far the highest AM sensitivity with a constant conversion factor of 5  $[\frac{kHz}{\%}]$ .

It was also observed that the AM-to-FM conversion factor in the analog PLL depends somewhat on some loop parameters, such as the amplitude of the input carrier and the servo gain. In this discriminator, the origin of this AM sensitivity lies in some imperfections in the PLL loop, which slightly shift the operating point out of its nominal position. In a perfect analog PLL, the two input signals (LO and RF) are locked in quadrature ( $90^\circ$  out-of-phase), as the error signal (mixer output) is zero in this phase condition. In such an ideal situation, it can be demonstrated that a PLL is fully insensitive to AM. However, a small electronic offset (e.g., induced at the servo input) may slightly shift the PLL operating point from the quadrature condition, making it sensitive to AM. The response to AM thus directly scales with the small phase shift from the quadrature point. Fine adjustment of the input offset of the PI servo controller allows to retrieve the correct PLL quadrature operation point and to minimize the AM sensitivity compared to the result shown in Figure 2.6,

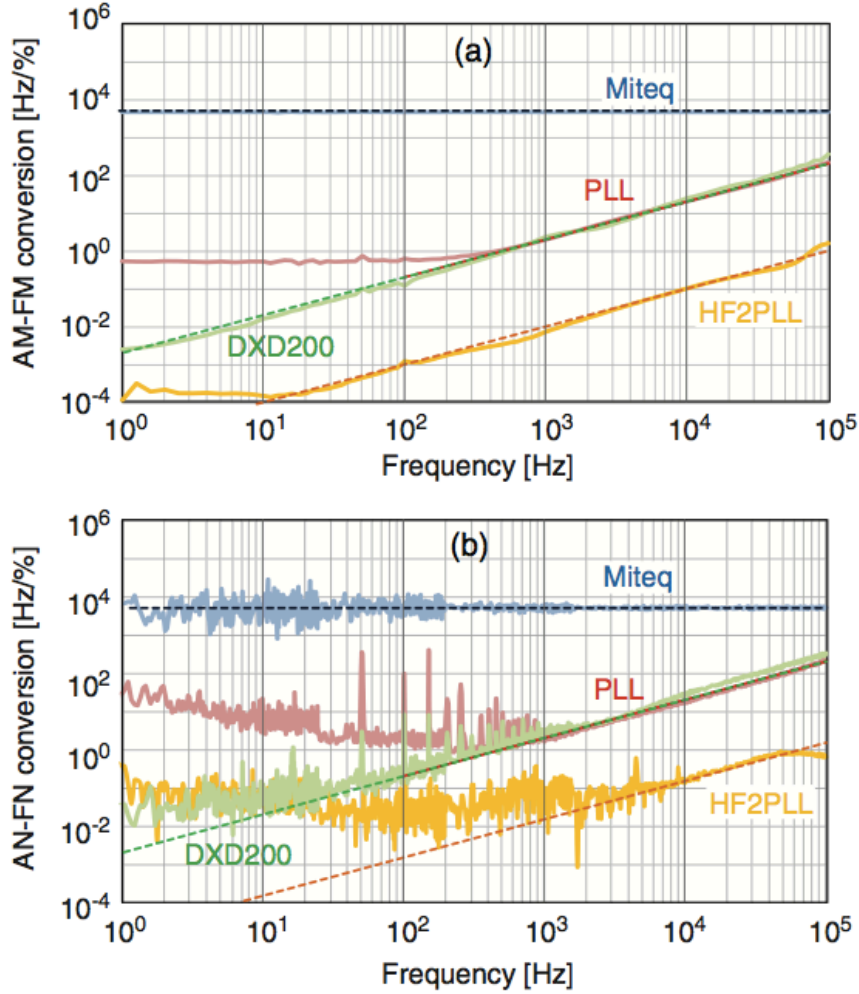


Figure 2.6: Cross-sensitivity of the discriminators to amplitude modulation (a) and to amplitude noise (b), expressed in terms of AM-to-FM (AN-to-FN) conversion factor (in  $[\frac{\text{Hz}}{\%}]$ ). The dashed lines represent an approximation of the AM-FM (AN-FN) conversion factor as a constant level (for Miteq) or proportional to  $f$  (for the other discriminators), obtained in the high frequency range where the measurements are out of the noise floor of each discriminator. These trend lines are used to extract numerical values for the AN-FN cross-sensitivity of each discriminator as listed in Table 2.1.

obtained without input offset correction. Such adjustment is quite straightforward in the presence of the pure AM, which is easy to detect, but is more critical in the presence of the simultaneous AM

and FM, or, even worse, in the presence of AN and FN.

## 2.4 Comparison of RF discriminators

Table 2.1 summarizes the main properties of each discriminator extracted from the characterization measurements of Section 2.3. A convenient means to compare the characteristics of different discriminators is to graphically depict their respective domain of application in the plane  $(f, S_{\delta\nu})$ . The idea is to represent a frequency or phase discriminator as a surface delimited by the following boundaries (Figure 2.7(a)): the discriminator noise floor  $S_{\min}$ , its bandwidth  $f_{\text{BW}}$ , and the maximum measurable frequency noise PSD  $S_{\max}$ . While the noise floor and the bandwidth of each discriminator are straightforwardly extracted from the measurements shown in Section 2.3, the upper frequency noise limit has been indirectly determined from the discriminator linear frequency range  $\Delta f_{\text{lin}}$ , taking into account the relationship that links the frequency noise spectrum and the linewidth. This relation has been discussed in detail in [6], while its experimental validation is given in Chapter 3. The main conclusions of this study is that the frequency noise spectrum  $S_{\delta\nu}(f)$  can be divided geometrically into two surfaces (the slow and fast modulation areas) by the  $\beta$ -separation line, defined as  $S_{\delta\nu}(f) = \frac{8 \ln 2}{\pi^2} f$ . It was shown in [6] that only the slow modulation area of surface  $A$ , for which  $S_{\delta\nu}(f) > \frac{8 \ln 2}{\pi^2} f$ , contributes to the linewidth of the signal,  $\text{FWHM} = \sqrt{(8 \ln 2)A}$ , while the fast modulation area  $S_{\delta\nu}(f) < \frac{8 \ln 2}{\pi^2} f$  only contributes to the wings of the lineshape without affecting the linewidth.

A correct measurement of the frequency noise of a beat signal requires that the linewidth of the analyzed signal be narrower than the discriminator linear range i.e.  $\text{FWHM} \ll \Delta f_{\text{lin}}$ . In order to have a sufficient margin, it is expected that  $\text{FWHM} \leq \frac{\Delta f_{\text{lin}}}{n}$  while in this study it is considered that  $n = 3$ . In this condition, the fraction of the spectral power which is out of the discriminator operating range can be shown to be 0.04% for a Gaussian lineshape

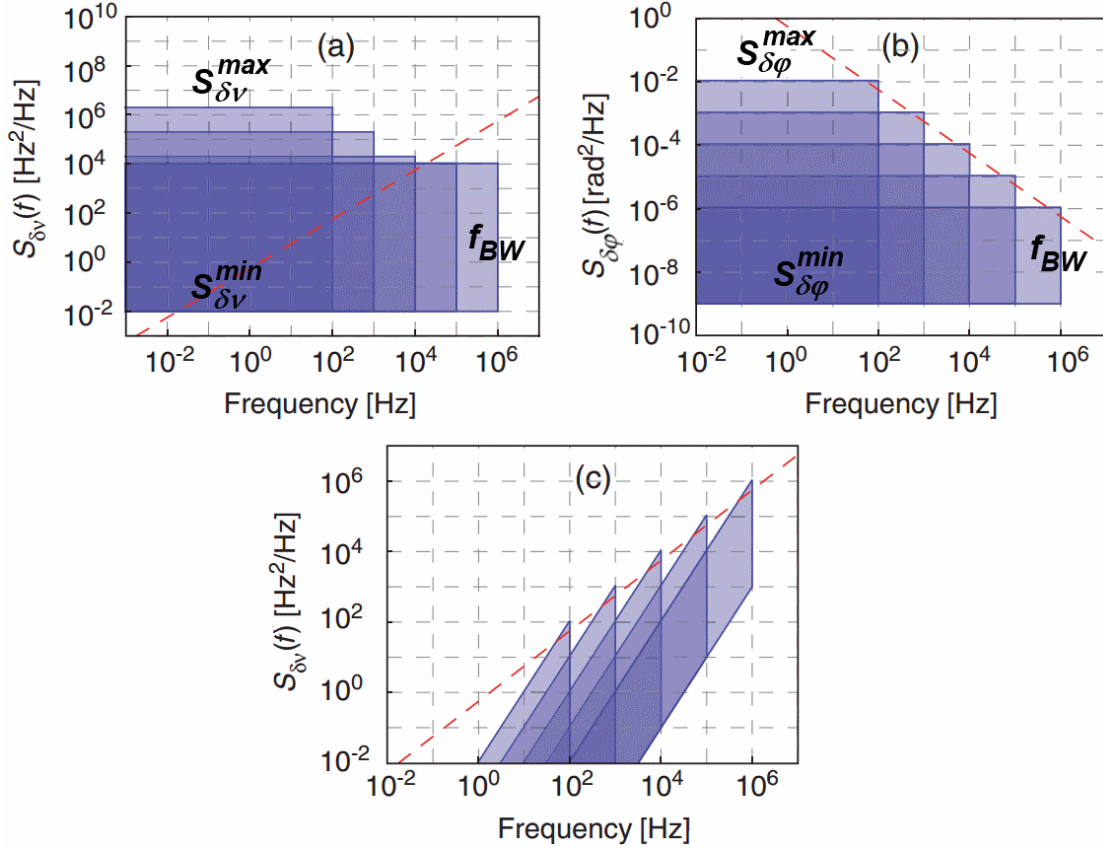


Figure 2.7: Examples of a graphical representation of a frequency/phase discriminator with different bandwidths ( $f_{\text{BW}} = 100 \text{ Hz}, 1 \text{ kHz}, 10 \text{ kHz}, 100 \text{ kHz}$  and  $1 \text{ MHz}$ ): (a) frequency discriminator in the plane  $(f, S_{\delta\nu})$ , (b) phase discriminator in the plane  $(f, S_{\delta\varphi})$ , and (c) phase discriminator in the plane  $(f, S_{\delta\nu})$ . The frequency discriminator has a range of  $\Delta f = 100 \text{ kHz}$  and a noise floor  $S_{\text{min}} = 0.01 \frac{\text{Hz}^2}{\text{Hz}}$ ; the phase discriminator has a range  $\Delta\varphi = 2\pi$  and a noise floor  $S_{\delta\varphi}^{\text{min}} = 10^{-9} \frac{\text{rad}^2}{\text{Hz}}$ . The dashed line represents the  $\beta$ -separation line  $S_{\delta\nu}(f) = \frac{8 \ln 2}{\pi^2} f$  in the frequency noise spectrum and its correspondent  $S_{\delta\varphi}(f) = \frac{8 \ln 2}{\pi^2} \frac{1}{f}$  in the phase noise spectrum.

(valid for  $\frac{8 \ln 2}{\pi^2} f_{\text{BW}} < S_{\text{max}}$ , see [6]) and 21% for a Lorentzian lineshape ( $\frac{8 \ln 2}{\pi^2} f_{\text{BW}} > S_{\text{max}}$ ). Assuming a white frequency noise in a bandwidth  $f_{\text{BW}}$ ,  $S_{\delta\nu}(f < f_{\text{BW}}) = S_{\text{max}}$ , the surface of the slow modulation area is simply  $A = S_{\text{max}} \cdot f_{\text{BW}} = \frac{\text{FWHM}^2}{8 \ln 2}$ , so that

Discriminator	Frequency range			Demodulation span	
	Total [MHz]	Linear [MHz]	Center [MHz]	Total $\Delta f_{max}$	Linear $\Delta f_{lin}$
Analog PLL	199-210	203-210	206.5	11 [MHz]	7 [MHz]
HF2PLL	1-49	...	...	$\frac{20}{D_\nu}$ [Hz]	$\frac{20}{D_\nu}$ [Hz]
Miteq	16-30	18-27	22.5	14 [MHz]	9 [MHz]
DXD200	0.5-200	...	...	$128\pi$ [rad]	$128\pi$ [rad]
	Sensitivity $D_\nu$		$\pm 0.9$ dB BW $f_{BW}$ [kHz]	AN-FN conv. $\left[\frac{\text{Hz}}{\%}\right]$	
Analog PLL	$7 \cdot 10^{-7} \frac{\text{V}}{\text{Hz}}$		200	$2 \cdot 10^{-3} \cdot f$	
HF2PLL	$8 \cdot 10^{-10} - 1.6 \frac{\text{V}}{\text{Hz}}$		50	$1.5 \cdot 10^{-5} \cdot f$	
Miteq	$1.25 \cdot 10^{-6} \frac{\text{V}}{\text{Hz}}$		2000	$5 \cdot 10^3$	
DXD200	$0.018 \frac{\text{V}}{\text{rad}}$		1000	$2 \cdot 10^{-3} \cdot f$	
	Noise floor $\left[\frac{\text{Hz}^2}{\text{Hz}}\right], S(f) \sim f^\alpha$				
	Range 1 $-2 < \alpha < -1$		Range 2 $\alpha = 0$	Range 3 $1 < \alpha < 2$	
Analog PLL	$4 \cdot f^{-2}$		$10^{-3}$	$1 \cdot 10^{-7} \cdot f$	
HF2PLL	...		$3 \cdot 10^{-12} D_\nu^{-2}$	$5 \cdot 10^{-13} \cdot f^2$	
Miteq	$10 \cdot f^{-1}$		$10^{-1}$	...	
DXD200	...		...	$1.5 \cdot 10^{-7} \cdot f^{1.3}$	

Table 2.1: Properties of the frequency/phase discriminators.

$$S_{\max} \leq \frac{\left(\frac{\Delta f_{\text{lin}}}{n}\right)^2}{8 \ln 2 \cdot f_{\text{BW}}}. \quad (2.5)$$

For a given discriminator range  $\Delta f_{\text{lin}}$ , the maximum measurable frequency noise thus decreases as the inverse of the discriminator bandwidth  $f_{\text{BW}}$ . This relation is valid as long as  $S_{\max} > \frac{8 \ln 2}{\pi^2} f_{\text{BW}}$ . On the contrary, when  $S_{\max} < \frac{8 \ln 2}{\pi^2} f_{\text{BW}}$ , it becomes independent of the bandwidth and  $S_{\max} = \frac{\Delta f_{\text{lin}}}{n\pi}$ . This results from the fact that the additional frequency noise occurring in a bandwidth increment does

not contribute to the signal linewidth, as it is entirely below the  $\beta$ -separation line [6]. The upper limit  $S_{\max}$  of the frequency discriminators has been determined for a white frequency noise; however, one has to keep in mind that a higher frequency noise level acting in a narrower bandwidth would still be measurable if its surface  $A$  was smaller than  $S_{\max} \cdot f_{\text{BW}}$ .

The geometrical illustration of the phase discriminator is slightly different, as it first has to be represented in the phase noise plane  $(f, S_{\varphi})$ . In that plane, the discriminator is also depicted by a rectangular surface, limited by the following boundaries (Figure 2.7(b)): the discriminator noise floor  $S_{\varphi}^{\min}$ , its bandwidth  $f_{\text{BW}}$ , and the maximum measurable phase noise  $S_{\varphi}^{\max}$ . As for the frequency discriminators previously considered, the maximum measurable phase noise  $\Delta\varphi_{\text{rms}}$  must be smaller than the discriminator linear range  $\Delta\varphi_{\text{lin}}$ :  $\Delta\varphi_{\text{rms}} \leq \frac{\Delta\varphi_{\text{lin}}}{2n}$ , again with the choice of  $n = 3$ . Assuming a low-pass filtered white phase noise  $S_{\delta\varphi}(f < f_{\text{BW}}) = S_{\delta\varphi}^{\max}$ , the rms phase fluctuations are given by the integrated phase noise

$$\Delta\varphi_{\text{rms}}^2 = \int_0^{f_{\text{BW}}} S_{\delta\varphi}(f) df = S_{\delta\varphi}^{\max} \cdot f_{\text{BW}}, \quad (2.6)$$

so that

$$S_{\delta\varphi}^{\max} \leq \frac{1}{f_{\text{BW}}} \left( \frac{\Delta\varphi_{\text{lin}}}{2n} \right)^2. \quad (2.7)$$

To have a constant phase excursion  $\Delta\varphi_{\text{rms}}$ , the maximum phase noise PSD must be inversely proportional to the discriminator bandwidth. In order to compare the frequency and phase discriminators in the same plot, the rectangular surface representing the phase detector in the plane  $(f, S_{\delta\varphi})$  is converted into the  $(f, S_{\delta\nu})$  plane by applying the transformation

$$(f, S_{\delta\varphi}(f)) \rightarrow (f, f^2 S_{\delta\varphi}(f)), \quad (2.8)$$

as  $S_{\delta\nu}(f) = f^2 S_{\delta\varphi}(f)$ . The constant lower and upper phase noise limits of the phase discriminator thus convert into the lines of slope +2 in terms of frequency noise (Figure 2.7(c)). One also notices that the maximum frequency noise value moves parallel to the  $\beta$ -separation

line as a function of the discriminator bandwidth, since it corresponds to  $S_{\max} = S_{\delta\varphi}^{\max} \cdot f_{\text{BW}}^2 = \Delta\varphi_{\text{rms}} \cdot f_{\text{BW}}$  and is thus proportional to the Fourier frequency like the  $\beta$ -separation line. From this observation it is possible to deduce the phase fluctuations that correspond to the  $\beta$ -separation line:

$$\Delta\varphi_{\text{rms}} = \frac{\sqrt{8 \ln 2}}{\pi} \cong 0.75 \text{ [rad]}. \quad (2.9)$$

The graphical comparison of different discriminators is shown in Figure 2.8. It is noticeable that the analog PLL discriminator and the Miteq RF discriminator have very similar properties in terms of minimum and maximum measurable frequency noise (slightly better for the analog PLL), but the Miteq discriminator has a wider bandwidth. Their noise floor below the  $1 \frac{\text{Hz}^2}{\text{Hz}}$  level over a wide frequency range and their intersection with the  $\beta$ -separation line at a Fourier frequency of a few hertz should enable these discriminators to characterize beat signals with a few hertz linewidth (assuming a white frequency noise), provided that no other undesirable effect will degrade the noise floor, as might be the case in presence of the amplitude noise (see discussion in the following Section 2.5). The digital phase detector DXD200 enables detection of much smaller frequency fluctuations, especially at low Fourier frequencies, as a result of its sensitivity to the phase fluctuations of the input signal. Owing to its applicability to a large fraction of the slow modulation area which is below the  $\beta$ -separation line, this discriminator is suitable for the characterization of coherent beat signals with sub-radian integrated phase noise. Nevertheless, the maximum frequency noise measurable with this device is limited to  $4.5 \times 10^{-3} \cdot f^2 \left[ \frac{\text{Hz}^2}{\text{Hz}} \right]$  due to its  $128\pi$  phase coverage.

The HF2PLL combines several advantages of the other discriminators. Its very low-noise performance, resulting from the numerical operation, converts into a low noise floor, which can be as small as  $3 \times 10^{-8} \frac{\text{Hz}^2}{\text{Hz}}$  (for  $D_\nu = 10 \frac{\text{mV}}{\text{Hz}}$ ). This makes the discriminator slightly more sensitive than the DXD200 for the characterization



of low-noise beat signals with down to sub-radian integrated phase noise, at Fourier frequencies higher than 100 Hz. However, its bandwidth is slightly lower than for the other discriminators. At lower Fourier frequencies, the HF2PLL discriminator does not compete with the superior capabilities of the digital phase detector DXD200, which results from its white phase noise floor. The flexibility offered by the computer selectable discriminator value  $D_\nu$  in the HF2PLL also makes possible the characterization of much wider beat signals with a linewidth ranging from kilohertz to megahertz, which is by far not possible with the digital phase detector. The analog PLL and the Miteq discriminators are also suitable for such broad linewidths.

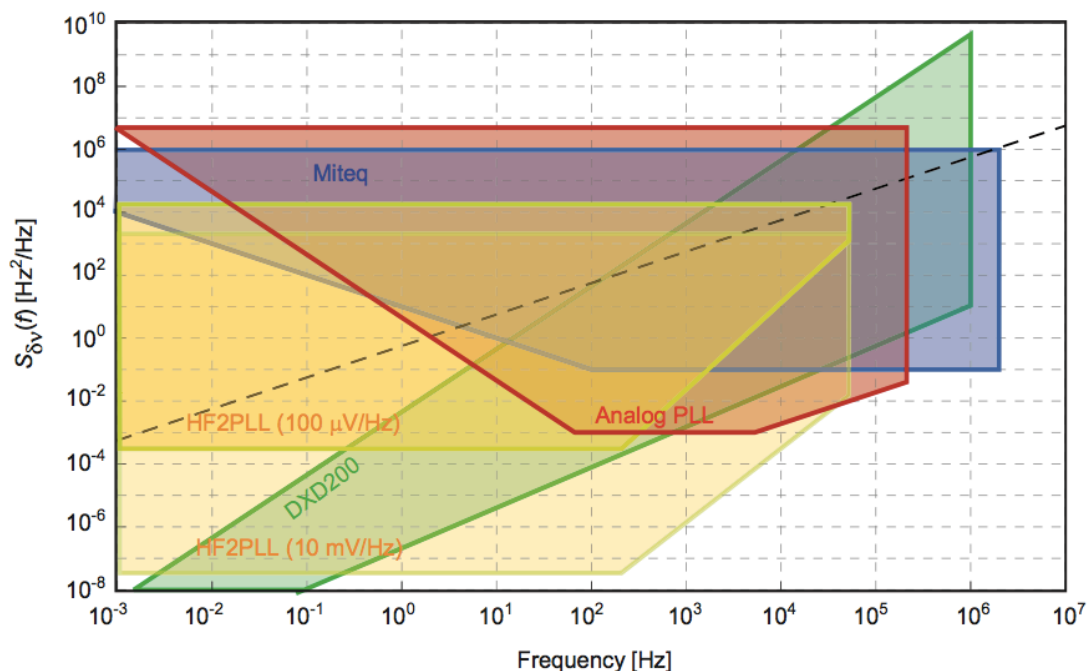


Figure 2.8: Graphical comparison of the characteristics of different discriminators. Each discriminator is represented by a surface delimited by its noise floor  $S_{\min}$ , its bandwidth  $f_{\text{BW}}$  and the maximum measurable frequency noise PSD  $S_{\max}$ . The situation for HF2PLL depends on the selected discriminator value  $D_\nu$  and is shown here for two cases,  $D_\nu = 100 \frac{\mu\text{V}}{\text{Hz}}$  and  $D_\nu = 10 \frac{\text{mV}}{\text{Hz}}$ . The dashed line represents the  $\beta$ -separation line  $S_{\delta\nu}(f) = \frac{8 \ln 2}{\pi^2} f$  [6].

## 2.5 Application of RF discriminators

In this section an example of the application of the described discriminators is presented. They are used for the characterization of a real experimental signal. For illustration purposes, the CEO beat signal of an optical frequency comb is used as a test signal. This CEO beat is generated from the output of a diode-pumped solid-state  $1.56\ \mu\text{m}$  Er:Yb:glass femtosecond laser oscillator, spectrally broadened to an octave spectrum in a highly nonlinear fiber. Detailed description of the frequency comb and generation of the CEO beat signal can be found in [8,29] as well as in Chapter 5. Self-referencing of the comb is achieved by stabilizing the CEO beat, detected in a standard f-to-2f interferometer [30] to a 20 MHz frequency reference signal using a PLL. The wide linear range of DXD200 digital phase detector, which can track large phase fluctuations of much more than  $2\pi$ , is used in the PLL to detect the CEO beat phase fluctuations.

The CEO beat signal of this comb was used to assess the capability of different discriminators to measure the frequency noise spectrum of a real signal. Each discriminator was used to demodulate the same 20 MHz CEO signal and the discriminator output signal was measured using an FFT spectrum analyzer to determine the frequency noise PSD of the CEO beat in the range from 1 Hz to 100 kHz. With the analog PLL discriminator, the CEO beat signal ( $f_{\text{CEO}} = 20\ \text{MHz}$ ) was mixed with a reference signal ( $f_{\text{ref}} = 227\ \text{MHz}$ ), in order to frequency up-convert it into the range of operation of this discriminator (at  $f_{\text{ref}} - f_{\text{CEO}} = 207\ \text{MHz}$ ). With all the other devices, the 20 MHz CEO beat was directly used with an amplitude of 0 dBm. Measurements were performed for the free-running CEO signal and for the CEO phase-locked to a 20 MHz reference signal to reduce its frequency noise. For the stabilized CEO beat, the digital phase detector DXD200 was used in the stabilization loop to produce the error signal that displays the phase fluctuations of the CEO beat compared to the reference signal. In that case, the frequency noise PSD measured with the digital phase detector is an in-loop measurement, but it was checked that an out-of-loop measurement performed

with a similar device gave an identical result. For all the other discriminators, the frequency noise spectra of the stabilized CEO were measured out-of-loop.

Figure 2.9 compares the CEO frequency noise spectra obtained with different discriminators. The free-running CEO beat has a line width (FWHM) of a few kilohertz [8], measured in an observation time of  $\sim 10$  ms. This linewidth is much smaller than the range of operation of all the frequency discriminators used (analog and numerical PLLs and Miteq), which are thus perfectly suitable for the characterization of the frequency noise of the free-running CEO beat. It is clearly seen that all of the measured spectra are in very good agreement (Figure 2.9(a)). However, the digital phase detector DXD200 is not applicable to the measurement of the free-running CEO, as the CEO phase fluctuations are much larger than the range of this discriminator, especially at low Fourier frequencies.

The frequency noise is strongly reduced when the CEO is phase-locked to an external frequency reference. A loop bandwidth of  $\sim 5.5$  kHz is sufficient to completely reduce the frequency noise of the CEO below the  $\beta$ -separation line, indicating that the CEO beat linewidth is reduced to zero, resulting in the apparition of a coherent peak in the CEO RF spectrum with a sub-radian integrated phase noise [9, 31], which is the characteristic of a tight phase lock. In that case, the small frequency noise occurring at low Fourier frequencies constitutes a very useful signal for the comparison of the discriminators, as shown in Figure 2.9(b). The digital phase detector DXD200 is the most sensitive discriminator at low Fourier frequencies, owing to its sensitivity to the phase of the signal rather than to its frequency. The measurement with the analog PLL discriminator overlaps the curve obtained with the digital phase detector in the frequency range  $f > 50$  Hz of the spectrum, where significant frequency fluctuations occur as a result of the limited feedback gain and the presence of the loop servo bump. At lower Fourier frequencies, the measurement is limited by the noise floor of the analog PLL discriminator.

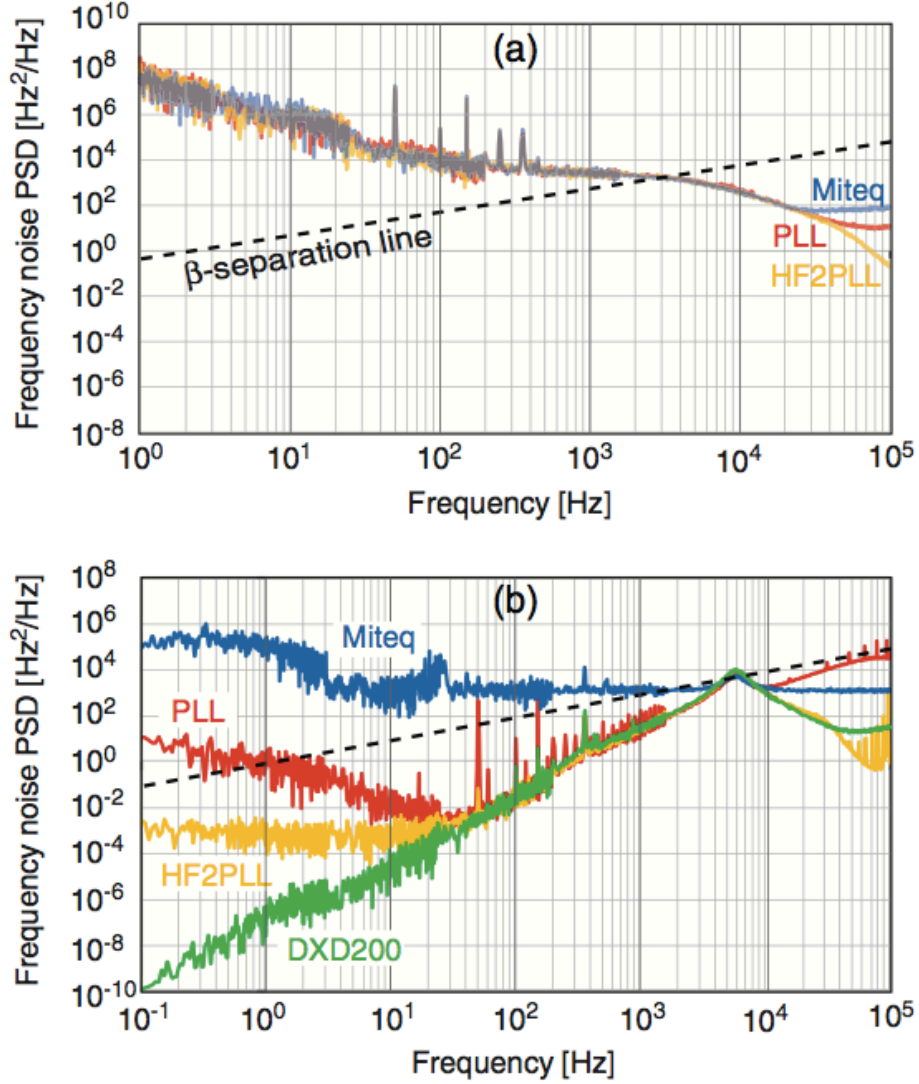


Figure 2.9: Frequency noise PSD of the CEO beat in the Er:Yb:glass frequency comb, measured with different discriminators; (a) free-running CEO and (b) CEO phase-stabilized to a 20 MHz reference signal. For HF2PLL, the discriminator value is  $100 \frac{\mu\text{V}}{\text{Hz}}$ . The  $\beta$ -separation line that is relevant for the determination of the CEO beat linewidth is also shown as a dashed line [6].

The HF2PLL should enable the detection of the lower frequency fluctuations due to its potentially much lower intrinsic noise floor, which can be reached at elevated discriminator sensitivity  $D_\nu$  (e.g.

$S_{\delta\nu}^{\min} = 3 \times 10^{-8} \frac{\text{Hz}^2}{\text{Hz}}$  for  $D_\nu = 10 \frac{\text{mV}}{\text{Hz}}$  from Subsection 2.3.3). However, such a high discriminator value could not be used in this measurement and a value  $D_\nu = 100 \frac{\mu\text{V}}{\text{Hz}}$  was used instead. The low frequency noise floor is reduced to  $\sim 5 \times 10^{-4} \frac{\text{Hz}^2}{\text{Hz}}$  in this case, which is in good agreement with the level observed in the CEO frequency noise spectrum.

Finally, Miteq discriminator, with its strong AN cross-sensitivity, can measure only a small portion of the locked CEO frequency noise spectrum, due to its high noise floor of  $\sim 1 \times 10^3 \frac{\text{Hz}^2}{\text{Hz}}$  out of the servo bump at  $\sim 7$  kHz. The relative amplitude noise PSD measured in the CEO beat is  $\sim -84 \frac{\text{dB}}{\text{Hz}}$  in the range between 200 Hz and 100 kHz and increases roughly as  $1/f$  for  $f < 200$  Hz (measured with a power detector). With the measured AN-FN conversion factor of  $5 \frac{\text{kHz}}{\%}$  for Miteq discriminator, this translates into an AN-induced noise floor of  $\sim 900 \frac{\text{Hz}^2}{\text{Hz}}$ , which is in very good agreement with the observed value of  $\sim 1 \times 10^3 \frac{\text{Hz}^2}{\text{Hz}}$ , showing that the measurement with this discriminator is strongly limited by its AN sensitivity.

## 2.6 Conclusion

The full characterization of the PLL frequency discriminator was presented in this chapter. This discriminator was developed in order to analyze the frequency noise properties of an RF signal, e.g. an optical beat signal between two lasers or between a laser and a frequency comb. Owing to its large linear frequency range of 7 MHz, its bandwidth of 200 kHz and its noise floor below  $0.01 \frac{\text{Hz}^2}{\text{Hz}}$  in the range from  $\sim 10$  Hz to 100 kHz, this frequency discriminator is able to fully characterize the frequency noise of a beat signal with a linewidth ranging from a couple of megahertz down to a few hertz. It thus has a wide range of applications, for instance for the characterization of the frequency noise spectrum of free-running lasers, the measurement of transfer functions in free-running optical frequency combs (for the CEO, the repetition rate or an individual comb line), or for

the characterization of the frequency noise properties of stabilized frequency combs and ultra-narrow linewidth cavity-stabilized lasers.

Three other types of commercially available discriminators, (i) a Miteq RF discriminator, (ii) a digital PLL (HF2PLL) encompassed in a high-frequency lock-in amplifier, and (iii) a digital phase detector (DXD200) have been characterized in order to make the comparison with the analog PLL. From their measured characteristics, these discriminators were compared with respect to their domain of application in the frequency noise plane ( $f, S_{\delta\nu}$ ). These discriminators have complementary properties that make them applicable to different types of input signals.

The Miteq discriminator is the simplest one to use. With its wide linear range of operation, it is perfectly suitable for the characterization of free-running lasers or frequency combs. Its white frequency noise floor of  $0.1 \frac{\text{Hz}^2}{\text{Hz}}$  reached at  $f > 100$  Hz with a  $1/f$  increase at lower frequencies, should make it applicable also for the analysis of narrow-linewidth signals. However, this discriminator has shown a strong sensitivity to amplitude modulation and amplitude noise with a conversion factor of  $\sim 5 \frac{\text{kHz}}{\%}$ , which strongly limits its use for low frequency noise signals in the presence of amplitude noise. For this reason, this discriminator could only measure a small portion of the frequency noise spectrum of the locked CEO in the frequency comb, the rest of the spectrum being hidden by the AN-induced noise floor.

The HF2PLL has a software-controlled output gain, allowing it to achieve a broad range of discrimination factors and thus to straightforwardly adjust its domain of operation. This flexibility, combined with its low intrinsic noise floor, makes this discriminator applicable to the characterization of lasers with a wide range of linewidths. However, the lower bandwidth of this discriminator prevents a complete characterization of the frequency noise spectrum of lasers with MHz-range linewidth, such as distributed feedback lasers. Furthermore, the potential capability of this discriminator to reach a very low noise floor at low Fourier frequencies, and thus to characterize low-noise beat signals with sub-radian integrated phase noise, is

somewhat limited by the impracticality of the use of a high discriminator factor with a real signal. For this reason, the characterization of the CEO frequency noise in the frequency comb was limited to Fourier frequencies  $f > 100$  Hz. At lower frequencies, a noise floor of  $\sim 10^{-3} \frac{\text{Hz}^2}{\text{Hz}}$  prevents the detection of smaller frequency fluctuations, despite the much lower intrinsic noise floor of the HF2PLL in the  $3 \times 10^{-8} \frac{\text{Hz}^2}{\text{Hz}}$  range obtained at a higher discriminator factor of  $10 \frac{\text{mV}}{\text{Hz}}$ .

Finally, the digital phase detector DXD200 is very sensitive to small frequency fluctuations at low Fourier frequency owing to its sensitivity to phase fluctuations, which makes it the most sensitive device for the characterization of a real beat signal containing simultaneous frequency noise and amplitude noise, such as encountered in the frequency-stabilized CEO beat in the Er:Yb:glass frequency comb.

## Chapter 3

# The $\beta$ -separation line and laser linewidth

Laser frequency fluctuations can be characterized either comprehensively by the frequency noise spectrum or in a simple but incomplete manner by the laser linewidth. A formal relation exists to calculate the linewidth from the frequency noise spectrum, but it is laborious to apply in practice. Recently a much simpler geometrical approximation, applicable to any arbitrary frequency noise spectrum was proposed [6]. In this chapter, an experimental validation of this approximation is presented. Laser sources of different spectral characteristics are used. For each of them, the measurement of the frequency noise spectrum as well as the direct measurement of the linewidth have been made. Afterwards the frequency noise spectrum has been used to calculate the approximate linewidth and compare it to the values measured directly. A very good agreement between the approximate and directly measured linewidths is observed over a broad range of values (from kilohertz to megahertz) and for significantly different laser line shapes.



## 3.1 Introduction

The linewidth, i.e., the full width at half-maximum (FWHM) of the optical line shape, is commonly used to characterize the spectral properties of a laser, as this single parameter is convenient to compare different laser sources in a simple and straightforward manner. However, it gives only poor information about the spectral distribution of the laser frequency noise. Fitting the laser line shape by a Voigt profile allows to extract the Lorentzian and Gaussian contributions, thus to get some information about the respective contribution of white frequency noise and flicker noise to the laser spectrum [32], but the information obtained in this way remains incomplete. Finally, any free-running laser suffers from flicker noise that diverges at low frequency, leading to a linewidth that depends on the observation time. All these points make the linewidth improper as a figure of merit of the laser spectral properties.

On the opposite, a full picture of the laser frequency noise is given by the frequency noise power spectral density (PSD). It represents the spectral density of the laser frequency fluctuations and shows noise spectral components that contribute to the laser linewidth. The frequency noise PSD can be measured by signal demodulation, using a frequency discriminator to convert the frequency fluctuations of the laser into measurable voltage fluctuations. An optical frequency discriminator, such as the side of an atomic/molecular transition [20,22] or of a Perot-Fabry resonance [24], can be used to measure directly the laser frequency fluctuations in the optical domain. Alternatively, a radio-frequency (RF) discriminator (Chapter 2) can be used to analyze the frequency fluctuations of the heterodyne beat signal between the laser under test and a reference laser in the electrical domain [5]. Both approaches are fully equivalent.

The frequency noise PSD contains the full information about the laser frequency noise. The optical line shape, and thus the linewidth, may in principle be calculated from the frequency noise spectrum, while the reverse process is not possible. However, the exact determination of the linewidth from the frequency noise spectral density

is not straightforward in most cases and involves a two-step numerical integration procedure [33–36], which will be briefly explained in Section 3.2.

Recently, a very simple approximation to determine the linewidth of a laser from an arbitrary frequency noise spectrum has been proposed, based on theoretical considerations [6]. Here, the first experimental validation of this simple formula will be presented. Using state-of-the-art femtosecond fiber and solid-state lasers as test signals, the comparison has been made between the linewidth calculated from the measured frequency noise PSD by the simple approximation from [6], and the actual linewidth independently measured. Femtosecond lasers were used as test signals because they offer easy and convenient means to modify the frequency noise spectrum and consequently to vary the corresponding linewidth over a broad range. The experimental validation of the simple approximation for the linewidth is presented over three decades, covering linewidths spanning from kilohertz to megahertz.

## 3.2 Theoretical background

The universal method for the calculation of the laser optical line shape from its frequency noise PSD  $S_{\delta\nu}(f)$  has been derived by Elliot et al. [33]. The PSD of the laser optical field  $S_E(\nu)$  is given by

$$\begin{aligned}
 S_E(\nu) &= \\
 &= 2 \int_{-\infty}^{\infty} e^{-i2\pi\nu\tau} \left[ E_0^2 e^{i2\pi\nu_0\tau} \times \exp \left( -2 \int_0^{\infty} S_{\delta\nu}(f) \frac{\sin^2 \pi f \tau}{f^2} df \right) \right] d\tau
 \end{aligned} \tag{3.1}$$

This expression is the Fourier transform of the autocorrelation function of the laser electric field represented by the term in the square brackets. The only situation in which Equation 3.1 can be analytically solved is the ideal case of a pure white frequency noise [34], which leads to the well-known Lorentzian line shape described by the

Schawlow–Townes linewidth [37], modified by Henry [38]. In the real case of an experimental frequency noise spectrum, Equation 3.1 has to be numerically integrated and some care is required in the implementation of this procedure to obtain the correct laser optical line shape without numerical artifacts. This includes the evaluation of the autocorrelation function of the laser electric field over an ensemble of correlation times  $\tau$ , i.e., the first integral (in the parentheses) has to be calculated many times for different values of  $\tau$ . Using improper values for either the overall range of  $\tau$  (which determines the resolution of the line shape spectrum calculated from Equation 3.1) or the sampling rate of the autocorrelation function (which determines the Nyquist frequency of the calculated line shape) may lead to an incorrectly calculated laser optical line shape. As the line shape (linewidth) to be retrieved is not known *a priori*, the choice of the  $\tau$  values is not trivial and may require an iterative process to achieve the correct linewidth. Furthermore, an experimental frequency noise spectrum covers a finite frequency range, so that the first integration cannot be performed between zero and infinity as defined in the general Equation 3.1. Therefore, one has to restrict the integration over a narrower interval, but from the double integration of the Equation 3.1, it is not obvious to determine which parts of the frequency noise spectrum contribute to the linewidth and which parts do not.

The recently introduced concept of the  $\beta$ -separation line in the frequency noise spectrum provides a straightforward metric to identify those spectral components that contribute to the linewidth [6]. Based on that concept a simple approximate formula to determine the linewidth of a laser from its frequency noise PSD is derived. This approximation, based on a geometrical separation of the frequency noise PSD into two areas, applies to any type of noise and avoids the two-step integration procedure required in the exact line shape calculation previously discussed.

Here, the principles of this approximation are briefly reviewed, while in the following sections, an experimental validation of this formula will be presented together with the assessment of the accu-

racy of this approximation, using real experimental laser spectra.

The  $\beta$ -separation line was introduced in the theoretical study [6] and is defined as

$$S_{\delta\nu}(f) = \frac{8 \ln 2}{\pi^2} f \quad (3.2)$$

It geometrically separates the frequency noise PSD in two regions (Figure 3.1), with significantly different influence on the optical line shape.

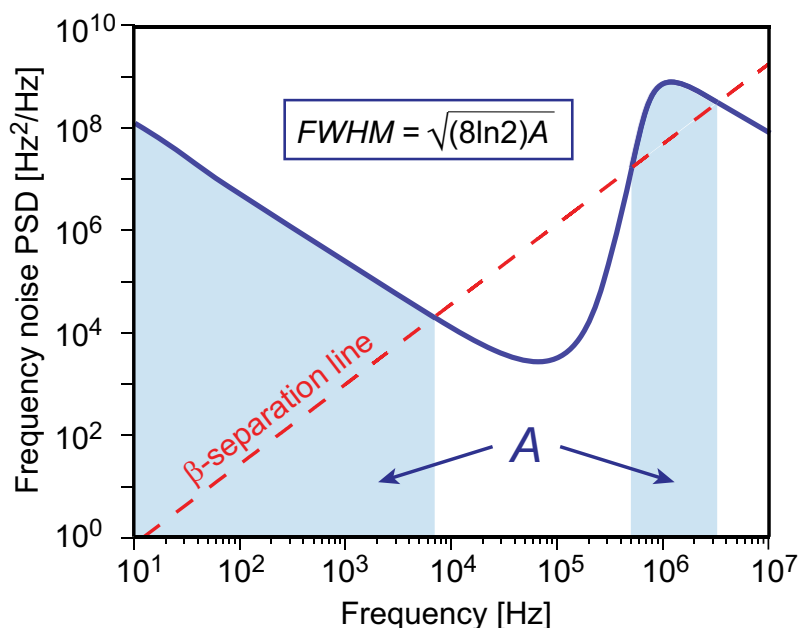


Figure 3.1: Graphical representation of the simple approximation proposed to determine the linewidth of a laser from its frequency noise PSD  $S_{\delta\nu}(f)$ , calculated from the surface  $A$  of the slow modulation area. The shadowed areas on this schematized frequency noise spectrum represent the surface  $A$  that encloses all spectral components for which  $S_{\delta\nu}(f)$  exceeds the  $\beta$ -separation line  $S_{\delta\nu}(f) = \frac{8 \ln 2}{\pi^2} f$  (dashed line).

Only the slow frequency modulation area, where  $S_{\delta\nu}(f) > \frac{8 \ln 2}{\pi^2} f$ , contributes to the linewidth of the signal. In the fast frequency modulation area, where  $S_{\delta\nu}(f) < \frac{8 \ln 2}{\pi^2} f$ , the frequency fluctuations are too fast to affect the laser linewidth and only contribute to the wings of the line shape. A very simple approximation of the laser

linewidth is obtained from the surface  $A$  of the slow modulation area of the PSD spectrum displayed in Figure 3.1:

$$\text{FWHM} = \sqrt{(8 \ln 2)A} \quad (3.3)$$

Here,  $A$  represents the overall surface under the portions of  $S_{\delta\nu}(f)$  that exceeds the  $\beta$ -separation line, which is mathematically obtained by integrating the product between the frequency noise PSD and the Heaviside step function  $H(x) = 0$  if  $x < 0$ ,  $H(x) = 1$  if  $x \geq 0$ :

$$A = \int_{1/T_0}^{\infty} H \left( S_{\delta\nu}(f) - \frac{8 \ln 2}{\pi^2} f \right) S_{\delta\nu}(f) df \quad (3.4)$$

A cut-off frequency  $1/T_0$ , where  $T_0$  is the observation time, is introduced to prevent the divergence of the integral, and consequently of the linewidth, in the presence of  $1/f$  noise. However, integration down to zero frequency (infinite observation time) is possible in the absence of diverging low-frequency noise.

In comparison with the two-step integration procedure, the approximation based on the  $\beta$ -separation line requires only the evaluation of the area of a bounded surface below the frequency noise spectrum  $S_{\delta\nu}(f)$ . This integration is quite trivial and not prone to numerical artifacts, making this method very robust and easy to apply.

### 3.3 Experimental setup

The validation of the theoretical approximation 3.3 of the laser linewidth requires examination of different test signals, covering a wide range of linewidths. An appropriate test signal for this study would be a laser source or an optical beat signal of variable linewidth. The carrier-envelope-offset (CEO) beat of a frequency comb, which corresponds to the heterodyne optical beat between comb lines located at the two extreme edges of an octave-spanning comb spectrum [30], can be changed in a wide range of linewidths. This convenience of

the CEO beat of a frequency comb makes it a good test signal for the experimental validation of the approximate formula 3.3. The schematics of the experiment is displayed in Figure 3.2, while the detailed explanations of the laser sources and the measurement techniques are presented in the corresponding Subsections.

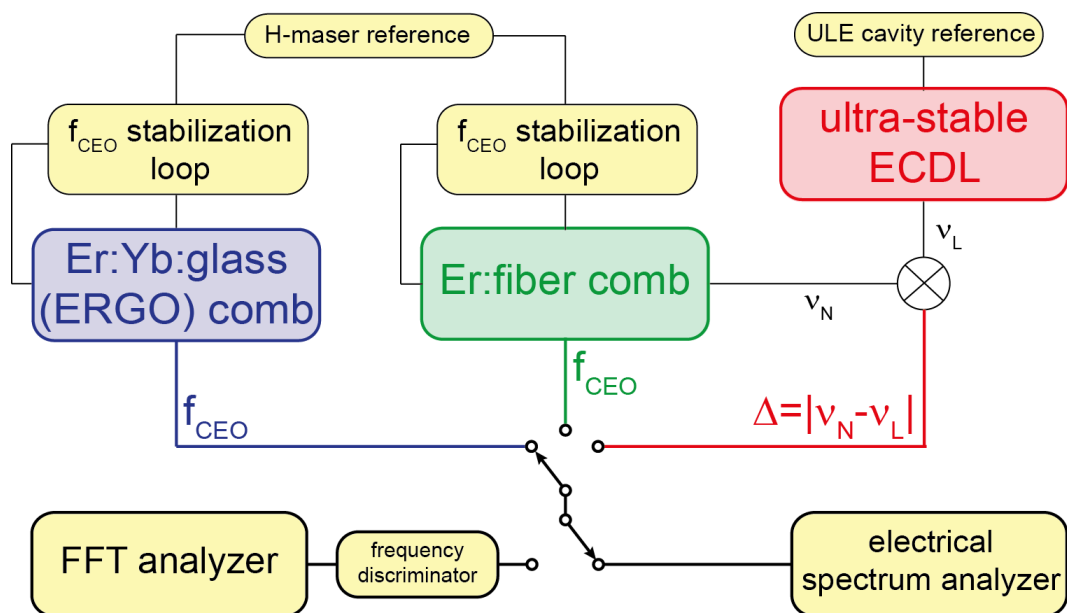


Figure 3.2: The experimental setup for the test of the  $\beta$ -separation line based linewidth approximation.

### 3.3.1 Laser sources

A frequency comb is generated from an ultrafast laser with femtosecond pulses. It comprises tens to hundreds of thousands of equidistant spectral lines that form a frequency ruler over a broad spectrum [21, 39]. The carrier-envelope-offset results from a phase shift between the laser pulse envelope and the carrier field. In the frequency domain, it is manifested as a uniform shift  $f_{\text{CEO}}$  of all frequency comb lines from exact harmonics of the laser repetition rate  $f_{\text{rep}}$

$$\nu_N = f_{\text{CEO}} + N f_{\text{rep}}. \quad (3.5)$$

In time and frequency metrology, a frequency comb provides a direct link between optical and microwave frequencies and is generally stabilized to a microwave reference. This is accomplished by phase-locking the two comb parameters ( $f_{\text{CEO}}$  and  $f_{\text{rep}}$ ) to a highly stable external reference. For the stabilization of the CEO in frequency combs used for this experiment, the phase fluctuations between the CEO beat and the external reference are detected in a digital phase detector (Menlo DXD200). After amplification by a servo controller, the feedback signal is applied to the pump diode of the femtosecond laser. Depending on the gain and bandwidth of the CEO servo loop, the frequency noise of the CEO beat, and thus its linewidth, may be modified. In this experiment, two different frequency combs were used, each covering a different range of linewidths. In each comb, the CEO beat is locked to a 20 MHz reference oscillator.

The first frequency comb is generated from a commercial Er:fiber laser (FC1500 MenloSystems, Germany) with 250 MHz repetition rate. This system suffers from significant noise, as commonly observed in Er:fiber lasers [40], leading to a measured free-running CEO beat linewidth of 200 kHz to 300 kHz (at 10 ms observation time). A linewidth ranging from 300 kHz to 2 MHz can be obtained in the stabilized CEO beat by altering the loop parameters.

The second frequency comb is based on an Er:Yb:glass (ERGO) laser oscillator, a femtosecond diode-pumped solid-state laser with 75 MHz repetition rate [8]. Its superior noise properties lead to a free-running CEO beat linewidth of  $\sim 4$  kHz (at 10 ms observation time) [9]. A narrow-linewidth range (4 kHz to 20 kHz) was covered with this system by changing the parameters of the CEO servo loop. Moreover, different levels of white noise were added to the piezoelectric transducer controlling the length of the femtosecond laser cavity, which induces additional frequency noise in the CEO beat due to the correlation between the noise of the repetition rate and of the CEO beat generally observed in a frequency comb [41]. In combination with the adjustment of the stabilization loop parameters, this en-

abled further broadening of the CEO linewidth in the intermediate range of 20 kHz to 100 kHz.

In both combs, the phase stabilization strongly reduces the low frequency  $1/f$  noise of the free-running CEO beat. Consequently, only a small portion of the frequency noise spectrum exceeds the  $\beta$ -separation line and contributes to the linewidth, which is moreover independent of the observation time. This allows a true comparison between the linewidth determined from the frequency noise PSD and the actual linewidth observed on a spectrum analyzer, without any experimental artifacts. This also enables a long averaging of the spectra in order to enhance the signal-to-noise ratio and to increase the accuracy of the linewidth determination, thus improving the comparison between the approximate and real linewidths.

Finally, a third different system has been considered in the analysis, in order to demonstrate the universality of the  $\beta$ -separation line approach to linewidth determination. It consists of the heterodyne beat between one line of the Er: fiber femtosecond laser and a 1.55  $\mu\text{m}$  cavity-stabilized ultra-narrow linewidth laser [42]. In this case, a frequency noise PSD of a different shape was obtained compared to the CEO beats of the frequency combs, with a corresponding linewidth of  $\sim 170$  kHz.

### 3.3.2 Frequency noise PSD measurement

The frequency noise PSD of the beat signals was measured using a frequency discriminator, in order to convert the frequency fluctuations into measurable voltage fluctuations [5]. For the ERGO and Er: fiber CEO beats, the digital phase detector DXD200 of the CEO stabilization loop was used, with a measured sensitivity of  $\approx 0.02 \times \frac{1}{f} \left[ \frac{\text{V}}{\text{Hz}} \right]$  (Chapter 2). It was demonstrated in [5] that these devices do not have a constant sensitivity over their entire range of operation. Some nonlinear points are observed, where local sensitivity significantly deviates from the average measured value. Even if the phase detector is operated out of these strong nonlinearities, the sensitivity slightly depends on the exact operating point. This



makes a very accurate determination of this sensitivity difficult, resulting in a typical uncertainty in the order of 10%. The frequency noise of the beat between the ultra-stable laser and the Er:fiber frequency comb was demodulated using an RF frequency discriminator (frequency-to-voltage converter) Miteq FMDM-21.4/4-2 with a sensitivity of  $1.25 \times 10^{-6} \left[ \frac{V}{Hz} \right]$  (Chapter 2). The response of this discriminator is dependent on the amplitude of the input signal [5], which leads to a similar uncertainty of 10% on the discriminator sensitivity.

For each experimental signal, the PSD of the discriminator output voltage was recorded on a fast Fourier transform (FFT) analyzer and afterwards converted into frequency noise PSD using the discriminator sensitivity. In order to achieve a good spectral resolution over the entire considered frequency range, each spectrum was obtained from the combination of five FFT spectra of decreasing spectral resolution (span of 24.4 Hz, 195 Hz, 1.56 kHz, 12.5 kHz, and 100 kHz) after co-averaging at least 300 individual FFT traces. The area of the frequency noise PSD exceeding the  $\beta$ -separation line was determined for each spectrum by Equation 3.4 and the approximate linewidth  $\text{FWHM}_{\text{PSD}}$  was then calculated using Equation 3.3. The relative uncertainty on the calculated linewidth lies in the range from 10% to 15% and is mainly due to the uncertainty on the discriminator sensitivity.

### 3.3.3 Line profile measurement

The RF heterodyne beat (either CEO beat or laser to comb beat) was separately recorded on an electrical spectrum analyzer (ESA). The absence of  $1/f$  noise in the spectra enables improvement of the signal-to-noise ratio of the recorded signal by co-averaging 200 spectra. The measured power spectra were fitted by a Voigt profile in order to extract the Gaussian and Lorentzian contributions and thus the Voigt linewidth  $\text{FWHM}_{\text{Voigt}}$ . The uncertainty in the Voigt linewidth was determined from the standard deviation of the Lorentzian and Gaussian contributions, using the analytical approximation of the Voigt linewidth given by Olivero and Longbothum [43]. De-

pending on the quality of the signal, the typical relative uncertainty ranges from 1% to 12%.

## 3.4 Results

For every test signal, both the line profile and the frequency noise PSD were measured in the same conditions. The objective was to directly compare the measured linewidths with those derived from the frequency noise PSD using the approximate formula 3.3. Some representative examples of experimental signals obtained for the three laser systems used in this study are shown in Figure 3.3.

The upper row of Figure 3.3 shows the frequency noise PSD  $S_{\delta\nu}(f)$  measured using the frequency discriminators. The surface  $A$  of the spectrum for which  $S_{\delta\nu}(f)$  exceeds the  $\beta$ -separation line (i.e. the slow modulation area) is represented by a shadowed area. The linewidth  $\text{FWHM}_{\text{PSD}}$ , calculated from this area by Eq. 3.3, is displayed in each plot with its corresponding uncertainty, obtained as described in Subsection 3.3.2 and indicated in parentheses. The lower row of Figure 3.3 shows the line shape profiles recorded on the ESA, together with the Voigt fit. The small values of the fit residuals shown on top of the line shapes in Figures 3.3(d)–3.3(f), which represent the difference between the fitting function and the measured data, validate the choice of a Voigt profile as a fitting function to extract the FWHM of the measured line shapes. The resulting Voigt linewidth  $\text{FWHM}_{\text{Voigt}}$  is indicated in each spectrum with the corresponding uncertainty in parentheses, obtained as described in Subsection 3.3.3.

In the example of the ERGO comb (left column in Figure 3.3), the narrow linewidth of 3.9(1) kHz is the result of the contribution of only a tiny portion of the frequency noise PSD (ranging from 300 Hz to 2 kHz). In the displayed example of the Er:fiber comb (right column in Figure 3.3), a larger part of the frequency noise PSD contributes to the linewidth, in particular the peak near 40 kHz corresponding to the servo bump that results from the deliberately

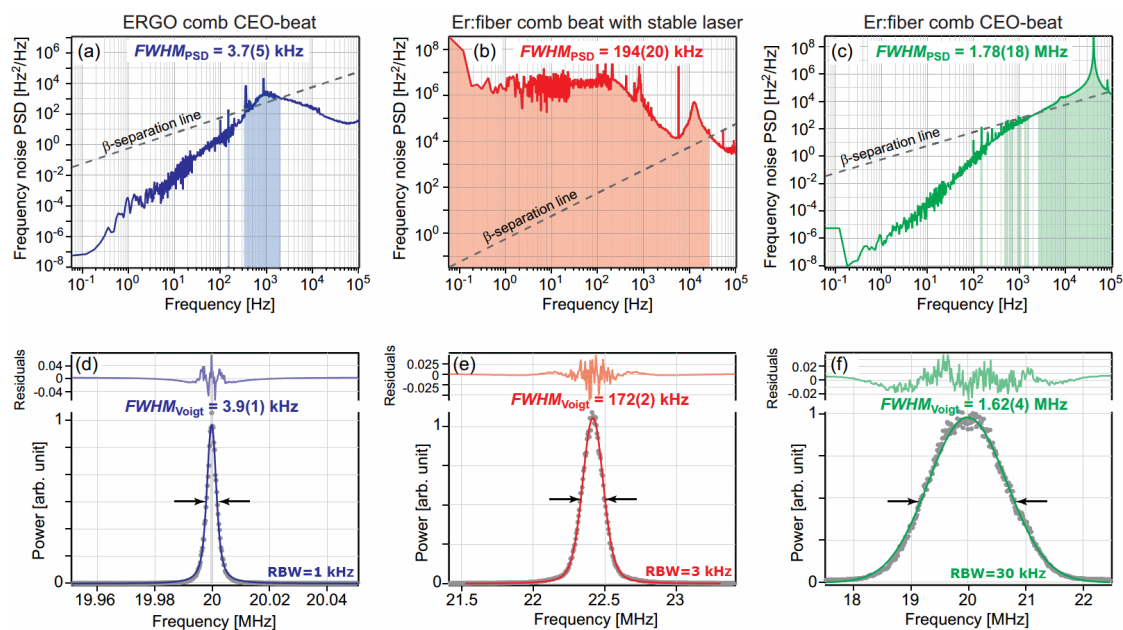


Figure 3.3: Representative examples of frequency noise PSDs (upper row) and corresponding line shapes (lower row) for three different laser systems: CEO beat in the ERGO comb (left), heterodyne beat between one line of the Er:fiber comb and a cavity-stabilized laser (middle), and CEO beat in the Er:fiber comb (right). The linewidth  $\text{FWHM}_{\text{PSD}}$  is calculated from the shadowed area for which the frequency noise PSD exceeds the  $\beta$ -separation line (dashed line). The line shapes were recorded using an ESA (grey circles) and were fitted by a Voigt profile (line) to extract the actual linewidth  $\text{FWHM}_{\text{Voigt}}$ . Fit residuals shown on top of the lower row represent the difference between the values of the fit function and the measured data. The uncertainty on the FWHM is given in parentheses following the FWHM value.

increased servo gain. This leads to a larger linewidth of 1.62(4) MHz.

In both comb signals, the low frequency noise does not contribute to the linewidth since it has been completely reduced below the  $\beta$ -separation line by the active CEO stabilization. This leads to a linewidth independent of the observation time. In the beat between the Er:fiber comb and the cavity-stabilized laser, the low-frequency noise is not strongly suppressed and all noise components at  $f < 30$  kHz contribute to the linewidth. However, the low-frequency noise remains bounded, i.e., does not diverge, so that

the corresponding linewidth of 170(2) kHz is also independent of the observation time.

Such measurements and data processing have been repeated for different experimental conditions in order to cover the widest possible range of linewidths. In total, 26 sets of data have been recorded and the corresponding linewidths have been extracted. They cover linewidth values ranging from 3.9(1) kHz to 1.62(4) MHz (19 points for the ERGO comb, 6 for the Er:fiber comb and one laser-Er:fiber comb beat). Figure 3.4 summarizes these results, showing the linewidth  $\text{FWHM}_{\text{PSD}}$ , calculated from the frequency noise PSD ( $y$  axis) as a function of the actual linewidth  $\text{FWHM}_{\text{Voigt}}$  ( $x$  axis) determined from the Voigt fit of the ESA trace, together with the corresponding error bars. One observes that all of the points in Figure 3.4, distributed over a broad range of almost three decades, are aligned on the  $y = x$  line within the experimental error bars. One also notices a systematic underestimation of  $\sim 10\%$  of the linewidth calculated from the frequency noise PSD using the simple approximation 3.3 for all points corresponding to a linewidth lower than 100 kHz. All these points have been obtained from the same laser system (CEO beat of the ERGO comb with or without additional noise applied to the comb piezo transducer) using the same digital phase detector. This systematic error can be attributed to a bias in the value of the discriminator sensitivity used in the scaling of the frequency noise PSD, which might result from a slightly different operating point of the phase detector as compared to the conditions used in the calibration of this device (Chapter 2), as discussed in Subsection 3.3.2. The point corresponding to a linewidth of  $\sim 170$  kHz in Figure 3.4 relates to the beat between the Er:fiber comb and the narrow-linewidth laser, which has been measured using a different frequency discriminator (Miteq FMDM-21.4/4-2 frequency-to-voltage converter). The sensitivity of this discriminator is dependent on the amplitude of the input signal and the 14% overestimation of the calculated linewidth, observed in Figure 3.4, might also result from a small bias in the considered discriminator sensitivity, due to slightly different signal amplitude used

in the experiment. Finally, the points of the broadest linewidth in Figure 3.4 were obtained from the CEO beat of the Er:fiber comb using the digital phase detector. The frequency noise of this signal being much larger than in the case of the ERGO comb, one cannot exclude that a small influence of the nonlinear response of the phase detector, as discussed in Subsection 3.3.2, slightly impacts these data points. In such a case, a different frequency noise level could likely lead to a different bias, which could be a reason for the absence of a systematic bias in Figure 3.4 in the data points corresponding to the Er:fiber comb. Nevertheless, the linewidths obtained with the simple approximation 3.3 are in agreement with the actual linewidths within the experimental error bars of approximately 10%. This result, furthermore obtained with three different laser systems, fully validates this simple approach to determine the linewidth of a laser from its frequency noise spectrum. Moreover, the line shapes considered in this study span from pure Gaussian ( $\gamma = 10^{-4}$ ), to almost an equal weight of Lorentzian and Gaussian contributions ( $\gamma = 0.91$ ), where  $\gamma$  represents the ratio of Lorentzian- to Gaussian-width of the Voigt profile. This characteristics shows that the proposed linewidth approximation based on the  $\beta$ -separation line applies to various line shape functions and demonstrates its broad usability.

## 3.5 Conclusion

In this work, a previously introduced simple geometrical approximation 3.3 to determine the linewidth of a laser from its frequency noise power spectral density has been experimentally validated. State-of-the-art laser light sources (two optical frequency combs and an ultrastable laser) have been used to generate the optical test signals of different spectral properties. For each of the test signals, both the frequency noise PSD and the line shape were independently measured. An excellent agreement between the approximate linewidth calculated from the experimental frequency noise PSD and the actual linewidth extracted from a fit of the measured line shape was

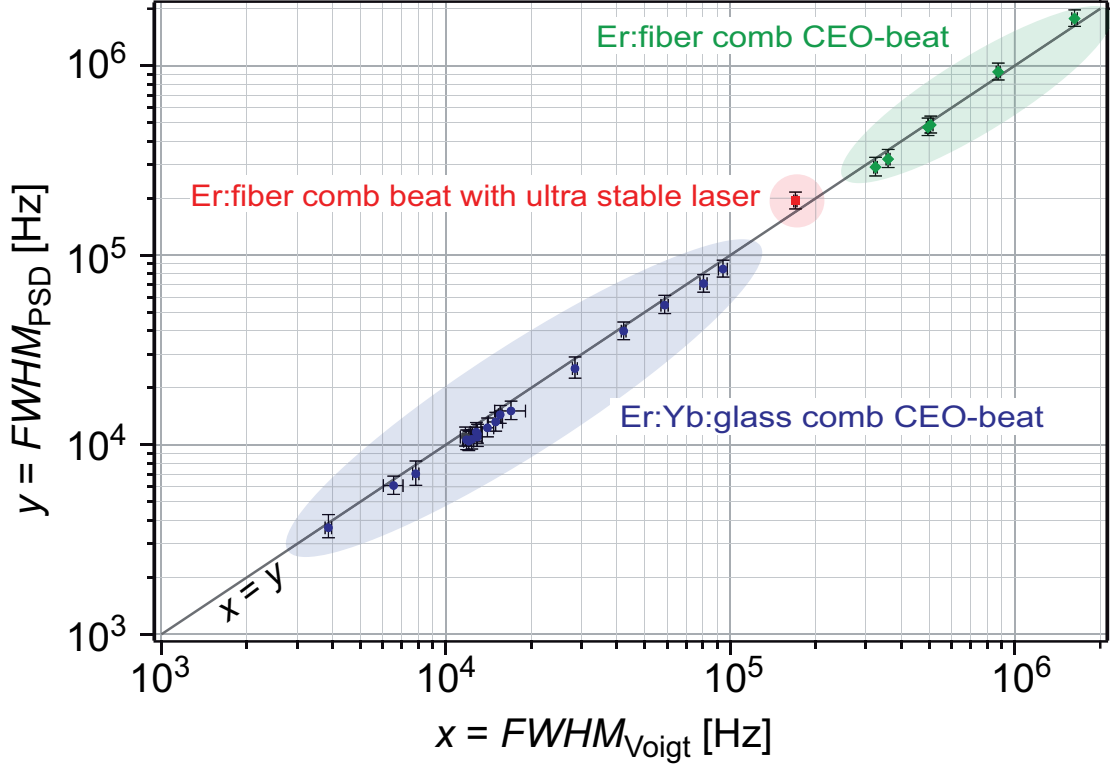


Figure 3.4: Comparison between the approximate linewidth  $FWHM_{\text{PSD}}$ , calculated from the measured frequency noise PSD ( $y$  axis), and the actual linewidth  $FWHM_{\text{Voigt}}$  ( $x$  axis) determined from the Voigt fit of the ESA trace, obtained over a broad range with three different laser systems. The uncertainty at each point is indicated by the error bars.

observed within the experimental uncertainties.

This study has demonstrated the applicability of this simple approximation of the linewidth over a broad range of values, spanning almost three decades (from  $10^3$  Hz to  $10^6$  Hz), and for a wide variety of line shape functions characterized by a ratio of Lorentzian- to Gaussian-linewidth ranging from  $10^{-4}$  to 0.9.

Altogether, this simple approximation is obtained in an easy and straightforward manner from any experimental frequency noise PSD, avoiding the complicated and time-consuming two-step numerical integration procedure encountered in the exact determination of the laser line shape (and thus linewidth) from the frequency noise PSD.

It thus represents a very useful tool for any experimentalist in laser physics as well as in time and frequency metrology.

# Chapter 4

## Ultra-stable optical reference

Laser development is continuously pushing forward the limits of the measurement precision. With the improvements in laser performance and the goal of the ever improving coherence in mind, new techniques and interesting applications have been set-up. Spectral characteristics qualify contemporary ultra-stable laser systems for the development of the new generation of the optical frequency standards [44]. Interrogation of the atomic reference transition by means of an ultra-stable optical oscillator, gives rise to the optical atomic clock signal, with the stability influenced by the coherence time of the interrogation oscillator [45]. In our work, the realization of the ultra-stable laser as a short-term optical reference was motivated by the fully optical generation of the low phase noise and high stability microwave signals, where the coherent frequency division from optical to microwave domain is performed by an optical frequency comb.

### 4.1 Introduction

In the past fifteen years, frequency metrology has witnessed a fruitful revolution. The measurement of the optical frequencies became straightforward for many research laboratories when the frequency



comb technology enabled coherent link between the optical and microwave frequency domain. Nowadays, the combination of the frequency comb with the ultra-stable laser, represents the gear mechanism of all of the optical clocks in operation worldwide. Furthermore, the cavity stabilized laser is obviously finding its use in the high resolution spectroscopy, where its linewidth of the order of 1 Hz and below enables access to the narrow atomic or molecular transitions. Whatever the use of the ultra-stable laser, its key property and attractiveness lies within the level of stability, reachable at the moment only in the optical domain.

The development of the stable optical reference was in the framework of the continuous cold cesium (Cs) atom fountain [46] project. The main goal is to provide optically generated microwave local oscillator with the state of the art short and mid-term performances, that could be used in the characterization of the cold atom fountain primary microwave frequency standard. The first ULE reference cavity, LTF-ULE1 [42] was developed and characterized in the first stage of the project. The second system (LTF-ULE2) is necessary in order to evaluate the performance of the laser stabilization. The experience with the first system enabled some slight improvements in the LTF-ULE2 design and assembly process. With all the noise contributions taken into account, the laser stabilized to such a reference cavity should reach the stability at the level of  $10^{-15}$  at 1 s integration time [47].

## 4.2 Pound-Drever-Hall stabilization technique

This technique can be applied both for locking a laser to a reference Perot-Fabry cavity, as well as for locking the cavity to the laser [48]. It has its roots in the similar microwave technique originally developed by R. V. Pound [49].

With the modern mirror coating techniques, it is possible to reach

very high reflectivity and low losses in the desired wavelength range. When an optical cavity is formed with the mirrors whose reflectivity is close to one for a predetermined wavelength range, it behaves as an optical resonator of very high quality factor. The transmission through the cavity is possible only in a narrow spectral width i.e. only when the incoming light is resonating in the cavity. It is possible to stabilize the laser to the side of the resonance fringe, but the narrow band-pass of the cavity transmission i.e. the long response time of the cavity limits the bandwidth of the stabilization loop in that case. In addition, with the use of the side of the resonance as the frequency discriminator, it is not possible to make a distinction between the frequency and the intensity noise of the laser.

In the Pound-Drever-Hall (PDH) technique, the incoming light consists of the carrier and the two first order phase modulation sidebands. The use of the high modulation frequencies (typically around 20 MHz) enables the operation far from the low frequency laser noise. As long as the modulation frequency is higher than the reference cavity resonance width, the sidebands are directly reflected, with no phase change and the carrier component is the subject to the complex response of the cavity [50]. If the carrier is at the right frequency, it will resonate in the cavity and a small portion of it will leak backwards through the cavity front mirror. The phase difference between the leaking field and the field directly reflected from the cavity can be measured by the detection of the interference term (at the modulation frequency) between the total field at the carrier frequency and the modulation sidebands. The light stored in the cavity serves as a reference field for the incoming light and when the feedback is correctly applied the two fields are phase-locked. The directly reflected portion of the light field is not affected by the cavity response time, thus making it possible to detect fast laser field fluctuations. With the error signal in reflection behaving as the first order low-pass filter [51] for the laser frequency fluctuations and with the proper design of the servo loop (e.g. to compensate for the phase shift that starts to be noticeable at the Fourier frequency equal to

the half of the resonance linewidth), it is possible to reach high stabilization bandwidth, unaffected by the response time of the reference cavity. The conceptual scheme of the Pound-Drever-Hall stabilization technique is shown in Figure 4.1.

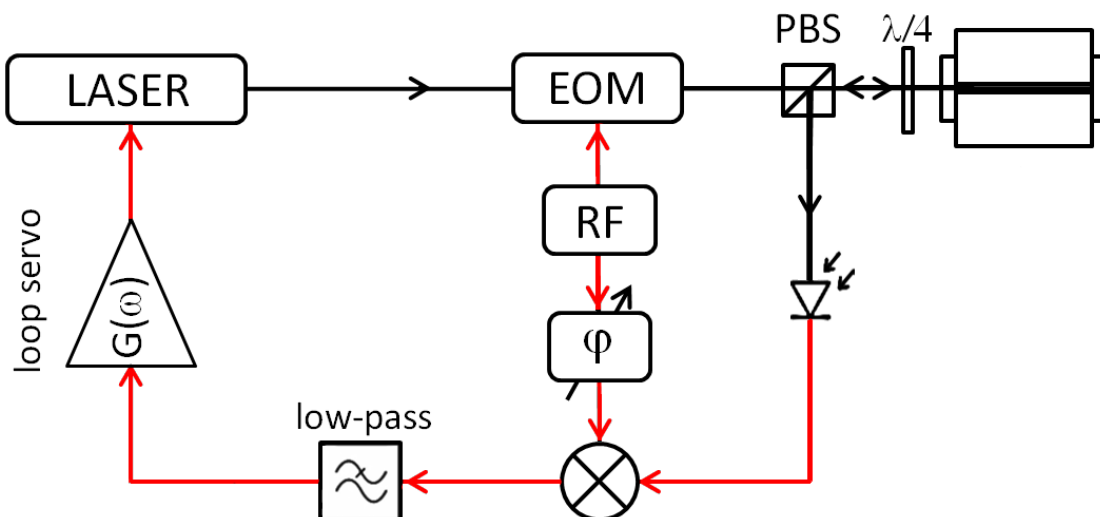


Figure 4.1: Pound-Drever-Hall concept of laser stabilization to a reference cavity. EOM: electro-optical modulator, PBS: polarization beam-splitter cube,  $\frac{\lambda}{4}$ : quarter-wave plate, RF: local radio frequency oscillator,  $\varphi$ : phase shifter. Black lines correspond to the optical path, while the red ones indicate the paths of the electronic signals.

### 4.2.1 Theoretical model

A detailed theoretical description of the Pound-Drever-Hall method is given by Black [52]. The laser light field is represented simply by  $E_0 e^{i\omega t}$ . After the phase modulation at the frequency  $\frac{\Omega}{2\pi}$  and with the small modulation index  $\beta$ , the incident light field will comprise the carrier at the frequency  $\frac{\omega}{2\pi}$  and two sidebands at frequencies  $\frac{\omega \pm \Omega}{2\pi}$

$$\begin{aligned}
 E_i &= E_0 e^{i(\omega t + \beta \sin \Omega t)} \approx \\
 &\approx E_0 \left[ J_0(\beta) e^{i\omega t} + J_1(\beta) e^{i(\omega + \Omega)t} - J_1(\beta) e^{i(\omega - \Omega)t} \right] \quad (4.1)
 \end{aligned}$$

where  $J_0(\beta)$  and  $J_1(\beta)$  are the Bessel functions of the first kind. Because of the small modulation index, the power of the unmodulated beam ( $P_0$ ) is split between the carrier with the power of  $P_c = J_0^2(\beta)P_0$  and only the two first sidebands with the powers of  $P_s = J_1^2(\beta)P_0$ .

The amplitude of the reflected beam is proportional to the amplitude of the incident beam and they are related by the complex reflection coefficient  $F(\omega)$

$$E_r = F(\omega)E_i = E_0 \left[ F(\omega)J_0(\beta)e^{i\omega t} + F(\omega + \Omega)J_1(\beta)e^{i(\omega+\Omega)t} - F(\omega - \Omega)J_1(\beta)e^{i(\omega-\Omega)t} \right]. \quad (4.2)$$

The phase modulation sidebands are reflected from the interferometer without any change in phase, while the reflected carrier field is a subject to a strong dispersive phase shift near the resonance [53]. The phase shifted carrier leaking out of the cavity and the directly reflected carrier are mixed with the non-shifted sidebands in the photo-detector, resulting in the AM signal at the modulation frequency, proportional to the laser frequency deviation from the cavity resonance [54]. In other words, the nonzero phase-shift on the carrier introduces an imbalance between the otherwise canceled mixing products of the upper and lower sidebands with the carrier. As a consequence, what would have been the perfect cancellation of the two out-of-phase beat signals (in the case of the pure phase modulation), is detected as the amplitude modulated signal that exhibits the discriminant behavior [50]. The reflected power  $P_r = |E_r|^2$ , detected on a photo-diode, in its developed form is given by

$$P_r = P_c|F(\omega)|^2 + P_s \left\{ |F(\omega + \Omega)|^2 + |F(\omega - \Omega)|^2 \right\} + 2\sqrt{P_c P_s} \left\{ \text{Re} [F(\omega)F^*(\omega + \Omega) - F^*(\omega)F(\omega - \Omega)] \cos \Omega t + \text{Im} [F(\omega)F^*(\omega + \Omega) - F^*(\omega)F(\omega - \Omega)] \sin \Omega t \right\} + 2\Omega \text{ terms.} \quad (4.3)$$

The detected power comprises both the absorptive and the dispersive response of the cavity. The desired anti-symmetric and dispersive

error signal is in phase with the phase modulation signal and is equal to the factor in front of the  $\sin \Omega t$  in Equation 4.3. By demodulation at the frequency  $\Omega$  [50], the error signal is extracted as

$$\varepsilon = 2\sqrt{P_c P_s} \operatorname{Im}[F(\omega)F^*(\omega + \Omega) - F^*(\omega)F(\omega - \Omega)]. \quad (4.4)$$

On the plot of the error signal (Figure 4.2) we can see a characteristic triple dispersive response, with zero crossing when any of the beam frequency components starts to resonate in the cavity. The slope signs are different for the sidebands and for the carrier.

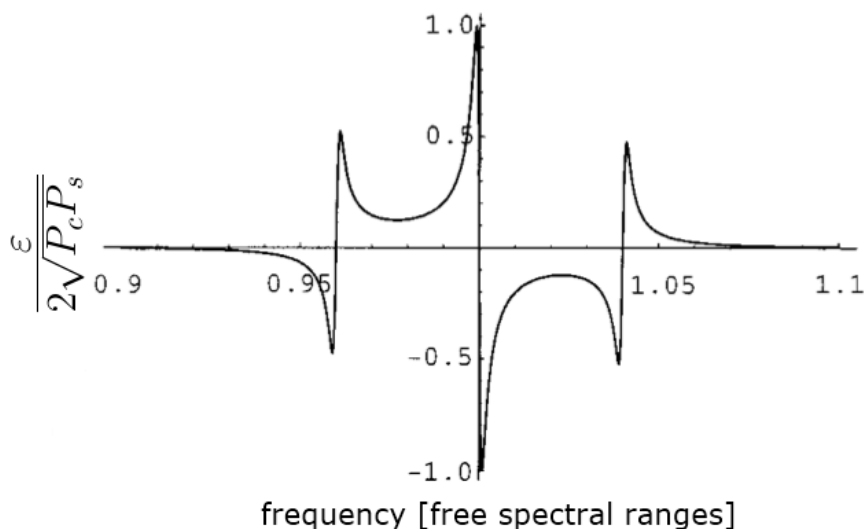


Figure 4.2: The Pound-Drever-Hall error signal [52].

One might wonder what would be the consequence of the improper setting of the demodulation phase and if that would introduce a portion of the unwanted absorptive feature to be present in the error signal. The contribution of the absorptive cavity response is zero at the cavity resonant frequency  $\omega_0$ , with the non-zero response only near the modulation sidebands i.e. when  $\omega - \omega_0 = \pm\Omega$ . The slope of the central part would be affected and the performance of the stabilization with it, but the lock point would not have been shifted.

Theoretically anticipated performance of the stabilization loop can be easily compromised by the technical imperfections [50, 55]. Any residual amplitude modulation (RAM, not to be confused with the laser intensity noise), i.e. amplitude modulation at the phase modulation frequency in the system, will be transmitted to the cavity error signal given by Equation 4.3 and it would introduce an offset in the locking system. Therefore it should not be ignored [56] but the use of an EOM instead of the direct laser current modulation helps to minimize its effect. Furthermore, the effect of the RAM is less expressed with the high finesse cavities [50].

## 4.2.2 Linear regime near the cavity resonance

For the illustrative purposes, it suffices to analyze the case of the symmetric and lossless cavity. The complex, amplitude reflection coefficient is given by

$$F(\omega) = \frac{r(e^{i\phi} - 1)}{1 - r^2 e^{i\phi}} \quad (4.5)$$

where  $r$  is the amplitude reflection coefficient of each of the cavity mirrors and  $\phi$  is the phase acquired by the beam during each round trip in the cavity. The phase itself can be expressed as

$$\phi = \frac{2\omega L}{c} = \frac{\omega}{FSR} \quad (4.6)$$

where FSR is the cavity free spectral range. The last equation shows that the amplitude reflection coefficient is dependent on the cavity properties ( $r, L$ ) as well as on the light frequency ( $\omega$ ). As it was mentioned at the beginning of this Section, the Pound-Drever-Hall technique can be used both for locking the cavity length to a stable laser or for locking a laser to a stable cavity. This relation of the length and the frequency is clearly seen through the above defined light phase.

In the vicinity of the resonance, since the modulation frequency  $\Omega$  is high, the sidebands are fully reflected,  $F(\omega \pm \Omega) \approx -1$ , and

the reflected carrier power is  $\sim |F(\omega)|^2 \approx 0$ . What remains as the reflected power is

$$P_r \approx 2P_s - 4\sqrt{P_c P_s} \operatorname{Im}[F(\omega)] \sin \Omega t. \quad (4.7)$$

Exactly on resonance, the phase  $\phi$  is equal to the multiple of  $2\pi$ , while in its vicinity, there is a small addition to it

$$\phi = 2\pi N + \delta\phi = 2\pi N + \frac{\delta\omega}{FSR} \quad (4.8)$$

With the approximation of  $e^x \approx 1+x$  in mind it is possible to express the amplitude reflection coefficient in terms of small frequency change  $\delta\omega$  as

$$F(\delta\omega) \approx \frac{r}{1-r^2} \delta\phi = \frac{r}{1-r^2} i \frac{\delta\omega}{FSR}. \quad (4.9)$$

In the case of the high reflectivity mirrors, the cavity finesse is given by

$$\mathcal{F} = \frac{FSR}{\Delta f_{\text{FWHM}}} = \frac{\pi r}{1-r^2} \quad (4.10)$$

where  $\Delta f_{\text{FWHM}}$  is the full-width half-maximum linewidth of the cavity resonance. The amplitude reflection coefficient is finally expressed as

$$F(\delta\omega) = i \frac{1}{\pi \Delta f_{\text{FWHM}}} \delta\omega. \quad (4.11)$$

Now the reflected power near the resonance is

$$P_r \approx 2P_s - \frac{4\sqrt{P_c P_s}}{\pi \Delta f_{\text{FWHM}}} \delta\omega \sin \Omega t \quad (4.12)$$

and the error signal is proportional to the deviation of the laser frequency from the cavity resonant frequency

$$\varepsilon = -\frac{4\sqrt{P_c P_s}}{\pi \Delta f_{\text{FWHM}}} \delta\omega. \quad (4.13)$$

In the vicinity of the resonance, the system is in the linear regime of operation, behaving as the frequency discriminator (frequency-to-voltage converter) with the discriminator slope

$$D = \frac{4\sqrt{P_c P_s}}{\pi \Delta f_{\text{FWHM}}}. \quad (4.14)$$

When the laser frequency exactly matches the cavity resonant frequency, the signal in reflection is equal to zero, because the leaking field and the incoming field are  $180^\circ$  out of phase. The anti-symmetric error signal carries the information about the deviation from the resonant frequency as well as the information on the sign of the correction that should be applied to keep the laser at the top of the resonance. Being at the top of the resonance and not on the side of it, makes this detection scheme immune to the laser intensity noise.

In order to increase the sensitivity to the frequency fluctuations, the discriminator slope should be maximized. The cavity design and the mirror reflectivity are utilized to decrease the  $\Delta f_{\text{FWHM}}$ . On the technical side, it is necessary to maximize the factor  $\sqrt{P_c P_s}$ . Since the powers in the carrier and the sidebands are proportional to the squares of the corresponding Bessel functions  $J_0(\beta)$  and  $J_1(\beta)$ , it is necessary to maximize the product  $J_0(\beta)J_1(\beta)$  with the relation to the modulation index  $\beta$ . The maximum of this product is reached for  $\beta=1.08$  and the corresponding power ratios are  $P_c = 0.52P_0$ ,  $P_s = 0.22P_0$  and  $P_s = 0.42P_c$ , where  $P_0$  is the power in the non-modulated carrier.

Finally, the advantageous characteristics of the Pound-Drever-Hall laser stabilization technique should be restated once more: large capture range (determined by the modulation frequency), decoupling of the laser frequency and intensity noise, response in reflection which is not limited by the cavity response (resulting in a high feedback bandwidth) and the high sensitivity (discriminator slope).



### 4.3 Planar waveguide extended cavity laser

A laser that is intended to be stabilized to a Perot-Fabry cavity should be a single frequency laser with intrinsically good noise properties and narrow linewidth. Additionally it should be tunable, while its control bandwidth should be sufficiently high. Successful stabilizations of extended cavity lasers (ECLs) has been previously reported [15, 57]. In our case, during the development of the LTF-ULE1 cavity, Newport Velocity 6328 laser (in further text referred to as ECDL) was routinely used. In the meantime, a novel technology has emerged, optimized for the low phase noise operation.

The planar waveguide extended cavity laser (PW-ECL) made by Redfern Integrated Optics Inc. is a low phase noise light source, interesting for the domain of the precision metrology, because of its spectral characteristics, form factor and low cost.

The PLANEX<sup>TM</sup> diode laser cavity configuration (Figure 4.3) involves an InP Perot-Fabry type gain chip with high reflectivity back mirror, coupled to a silica-on-silica Planar Lightwave Circuit (PLC) containing a Bragg grating which serves as a wavelength selective feedback filter and enables a single mode operation. This hybrid

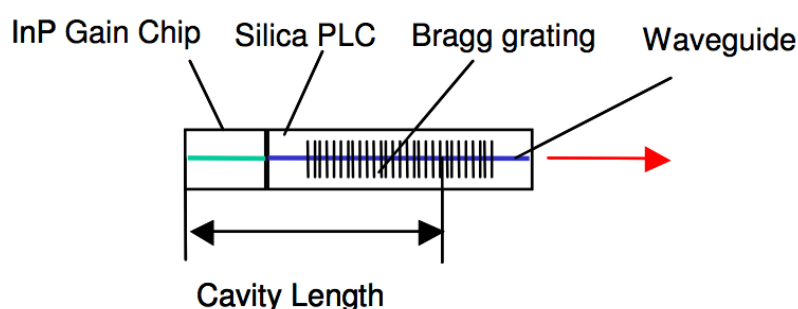


Figure 4.3: Schematics of the PLANEX<sup>TM</sup> technology based laser

laser structure is hosted in a standard 14-pin laser diode butterfly package. The highly stable, PM fiber coupled output, lies in the C-band (1528 nm to 1565 nm) spectral region, with the linewidth of

the order of 10 kHz and less, depending of the grade of each individual device. The wavelength of our laser is 1557.643 nm, well close to the maximum reflectivity of the reference cavity mirror coatings (1557 nm).

The PLANEX<sup>TM</sup> technology based laser butterfly package is installed in the ORION<sup>TM</sup> module (102 mm × 57 mm × 13 mm, Figure 4.4), which integrates the temperature controller and a low noise current driver.

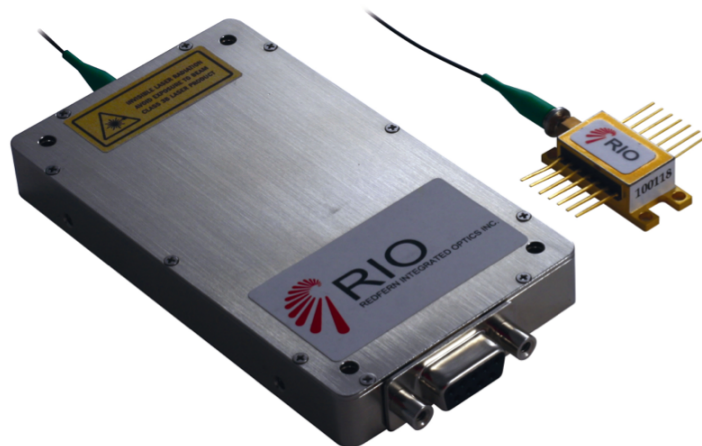


Figure 4.4: ORION<sup>TM</sup> module, housing a PM fiber coupled PLANEX<sup>TM</sup> butterfly package, temperature controller and low-noise current driver.

The laser module is connected with a computer by serial RS-232 port and is controlled by software. At the same connector, two pins are dedicated as a port for the external laser frequency control (acting on the laser injection current) and a separate cable is installed by the manufacturer for that purpose. The output of the laser can also be tuned by the temperature, controlled by thermoelectric cooler (TEC). The tuning range is about 0.4 nm within the temperature range from 15°C to 45°C, corresponding to  $\sim 50$  GHz change in frequency. In addition, laser wavelength exhibits the hysteresis behavior with the temperature change [58]. Injection current frequency tuning, in the high current regime around 91.5 mA, has been measured from the beat with the 250 MHz Er: fiber frequency comb (MenloSystems, Germany). The change of the laser power and its frequency

tuning with the injection current ( $\approx 23 \frac{\text{MHz}}{\text{mA}}$ ) are displayed in Figure 4.5. This tuning coefficient is dependent on the laser injection

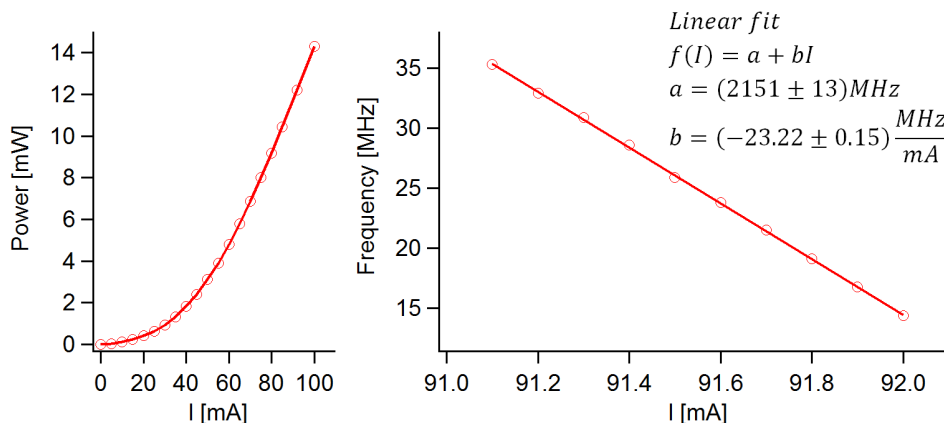


Figure 4.5: Output power and frequency tuning of the PW-ECL with the injection current.

current. It was also measured in the low-current ( $\sim 33 \text{ mA}$ ) and the mid-current ( $\sim 56 \text{ mA}$ ) region, and in these cases its values were  $\approx 28.9 \frac{\text{MHz}}{\text{mA}}$  and  $\approx 27.6 \frac{\text{MHz}}{\text{mA}}$ , respectively.

The frequency noise power spectral density of the free-running PW-ECL (Figure 4.6) [13] has been measured from the heterodyne beat with the Newport Velocity ECDL stabilized to the LTF-ULE1 cavity, by the Miteq RF frequency discriminator (Chapter 2).

Only the noise that is above the  $\beta$ -separation line contributes to the laser linewidth (Section 3.2), which is in this case up to the Fourier frequency of  $\sim 3 \text{ kHz}$ . The linewidth of the PW-ECL, calculated from the frequency noise PSD by Equation 3.3, amounts to less than  $10 \text{ kHz}$  for an observation time of  $0.1 \text{ s}$ .

The attempts to lock the laser to the reference cavity only by feedback to the laser injection current were unsuccessful. Figure 4.7 shows the response of the PW-ECL within the ORION<sup>TM</sup> module to the injection current modulation [13]. This transfer function was measured in a lock-in scheme by demodulating the heterodyne beat note signal between the PW-ECL and a frequency comb, again using the frequency discriminator technique (Chapter 2). In the amplitude, the  $-3 \text{ dB}$  bandwidth is  $\sim 3 \text{ kHz}$ , which is only marginally enough

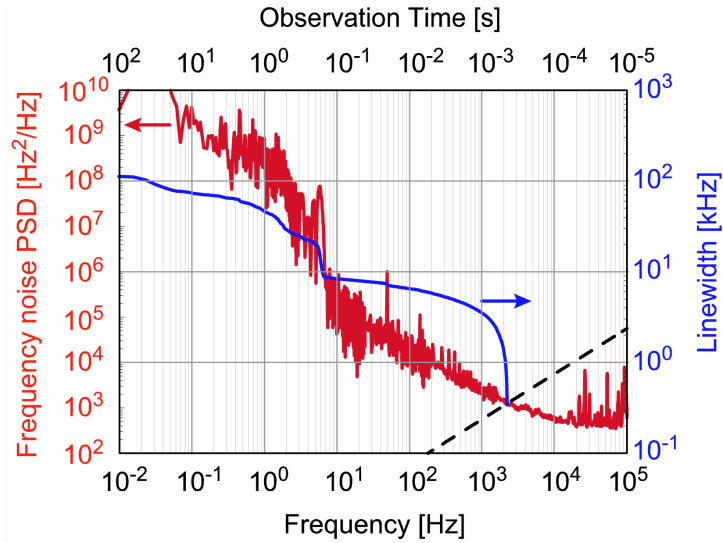


Figure 4.6: Left scale: Frequency noise power spectral density (PSD) of the free-running PW-ECL. Right scale: Linewidth of the free-running PW-ECL, calculated from the frequency noise PSD (Equation 3.3) [59].  $\beta$ -separation line (Equation 3.2) is shown as dashed black line.

for the effective feedback. The bandwidth of the ORION<sup>TM</sup> module limits the possibility of a lock by feedback to the laser injection current and an acousto-optic modulator has to be used in order to increase the feedback bandwidth.

## 4.4 Reference cavity housing

Compared to the LTF-ULE1 system [42], the mechanical layout is improved in few details. The layout of the fully assembled system is shown in Figure 4.8.

The second system is built with the proper commercial components i.e. the rigid optical table with the thick breadboard as the basis. Wheels are added to the table to make it transportable, but when the system is placed in the desired position, the standard support stands can be adjusted in order to shift the contact points from the wheels and bring the system to a rigid contact with the ground. The active anti-vibration system (AVI 200, HWL Scientific Instru-

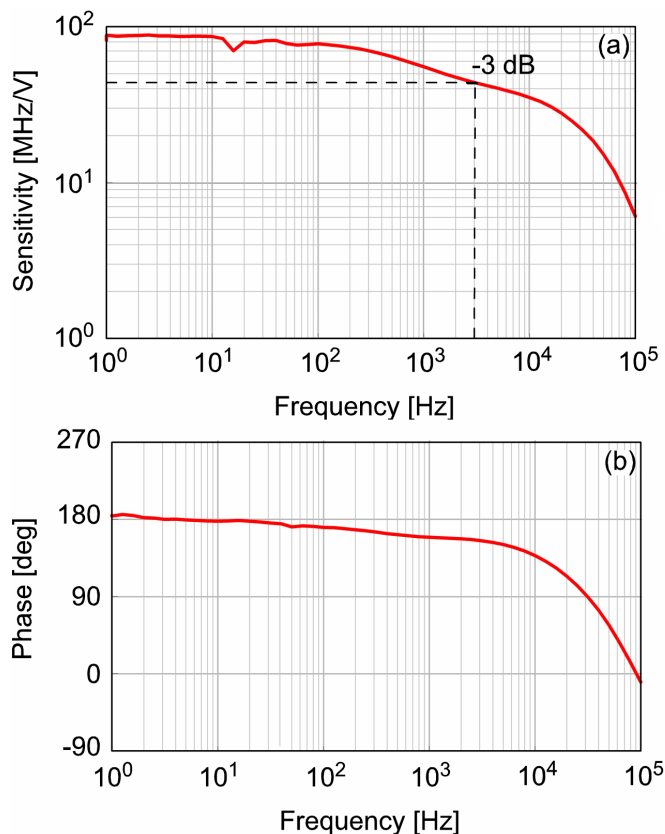


Figure 4.7: Transfer function in amplitude (a) and phase (b) of the RIO PW-ECL for the injection current modulation, applied through the ORION<sup>TM</sup> modulation port. The amplitude -3 dB bandwidth is  $\sim 3$  kHz [59].

ments) is placed at the base (thick) breadboard, with the main (thin) breadboard placed on top of the AVI.

On top of the main breadboard we have installed the vacuum chamber and the small breadboard with the optical components used to inject the light into the reference cavity. This breadboard (60 cm  $\times$  30 cm) is lifted 18 mm from the surface by four home made pads, in order to align the injection system with the optical axis of the ULE cavity. With the masses of the vacuum chamber assembly and the injection optics part taken into account, the positions of the center of mass is determined in order to avoid that the system is leaning towards the vacuum chamber side. The vacuum chamber has been

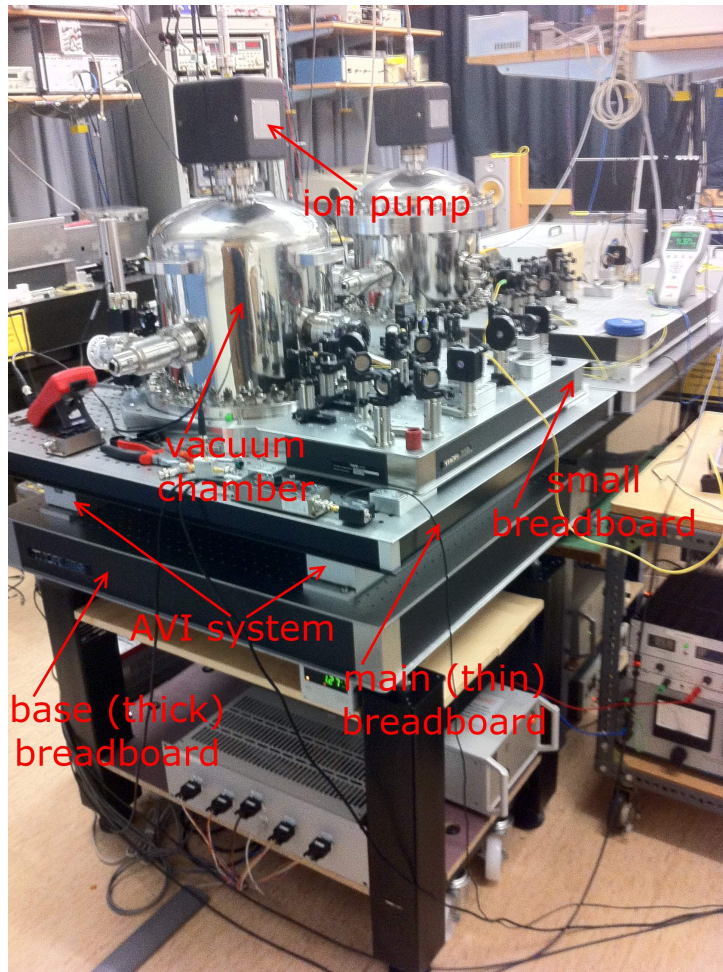


Figure 4.8: LTF-ULE2 reference cavity housing. Bottom shelf: temperature control system. In a bottom-up direction: base breadboard (thick), two arms of the active anti-vibration system, main breadboard (thin), vacuum chamber and an ion pump. On a side: small breadboard with the free-space optics for the injection of light into the reference cavity.

manufactured with the angled input and output window holders and indium sealed anti-reflection high precision BK7 windows (FOCtek Photonics Inc., China) have been installed. Before the insertion of the ULE cavity, the vacuum system has been tested for leaks and has been constantly pumped and outgassed in three cycles by baking it up to  $140^{\circ}\text{C}$ . After the installation of the cavity, the system was outgassed one more time, with the baking temperature not exceeding

70°C.

The fluctuations of the residual air pressure in the vacuum chamber induce the refractive index fluctuations, which then introduce the change of the cavity optical length. The dependence of the refractive index change with the pressure is given by [47]

$$\delta n \sim 3 \times 10^{-7} \times \delta p \text{ [mbar]}. \quad (4.15)$$

With the goal of the relative frequency stability i.e. the relative cavity length change of the order of  $10^{-15}$  and with the above stated contribution of the pressure fluctuations to the index of refraction fluctuations, it is important that the pressure variations are at the level of  $10^{-8}$  mbar or lower. When the cavity has been installed and the system closed, the residual pressure of  $2 \times 10^{-7}$  mbar is reached and is maintained with the 20 l/s ion pump (StarCell<sup>®</sup> 20, Varian Inc.). The pressure sensor control unit indicates the short-term fluctuations at the second decimal place. If we imagine that the pressure oscillations were higher, at the level of e.g. 10% ( $\delta p = \pm 2 \times 10^{-8}$  mbar), the contribution to the relative variation of the optical path length is still below the level which would compromise the system target performance. In the first system, with the identical ion pump and the volume of the vacuum chamber, the residual pressure is at the level of  $3 \times 10^{-8}$  mbar [59], owing to the indium seal applied between the vacuum chamber and the baseplate, while for the second system the Viton<sup>®</sup> O-ring is used. If at some point it turns out that the improvement of the vacuum is needed, the indium seal should be installed in the second system as well.

## 4.5 Cavity thermal enclosure

The ultimate performance level of the high-finesse Perot-Fabry cavity is set by the thermal noise (Brownian motion) of the materials used for the production of the spacer, mirror substrates and mirror coatings [60]. Temperature stability of the cavity as well as keeping



the cavity at the temperature of the minimum of the thermal expansion coefficient are crucial for the minimization of the frequency drift of the cavity resonance.

We have designed a two layer thermal enclosure in order to isolate the cavity from the external temperature fluctuations and to reach a high level of cavity temperature homogeneity. The goal would be to achieve state-of-the-art short-term laser frequency stability and to extend it to mid-term, up to a few tens of seconds of the integration time. The thermal enclosure is displayed in Figure 4.9. The

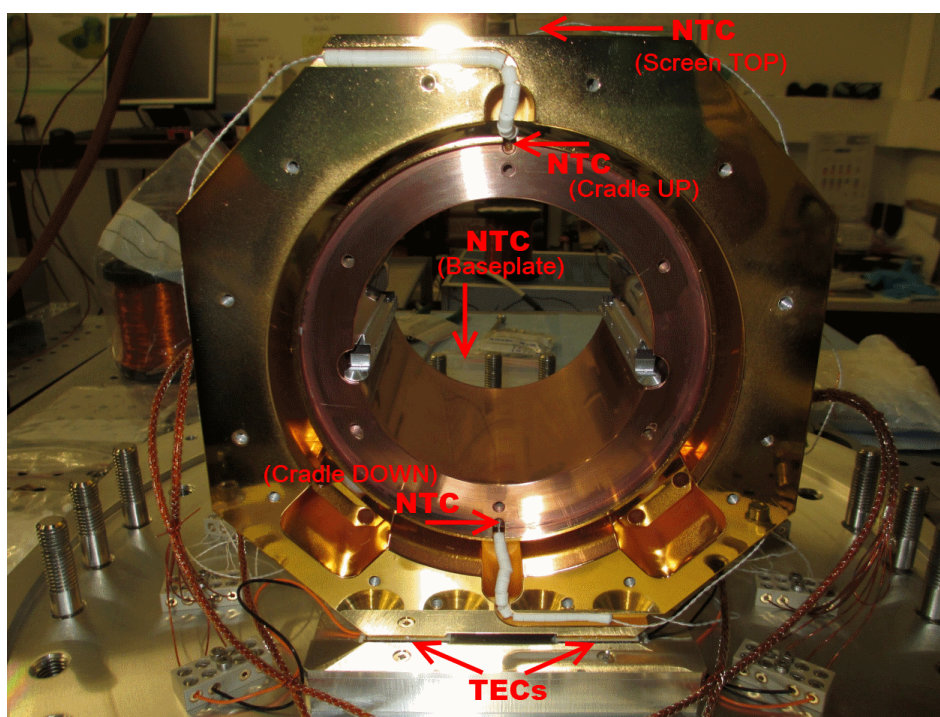


Figure 4.9: LTF-ULE2 reference cavity thermal enclosure. Inner layer ("cradle") made of copper, gold coated only on the outer surface. Outer layer ("screen") made of aluminum, fully gold coated.

inner cylinder ("cradle") is made of copper and acts as a black body that imposes a homogeneous temperature distribution onto the cavity. The copper inner surface is not coated, in order to maximize the radiative heat exchange between the cradle and the cavity. Its outer surface is gold coated and faces the inner surface of the outer



layer which acts as a thermal screen. The "screen" is made out of aluminum and serves as a thermal filter between the environment and the cradle-cavity system. The screen is fully gold coated, therefore its heat exchange by radiation is minimized. The optical access to the cavity is enabled by two BK7 anti-reflection windows (Thorlabs WG11050-C), which are thermally contacted to the screen front and back cover by indium seals. The temperature of the screen is controlled by four Peltier elements (thermo-electric couples - TECs, model MELCOR HT4-12-30-T2) which are placed at four corners ("feet") of the bottom surface of the screen. The thermal contact between the screen and the TECs is improved by application of the LewVac<sup>TM</sup> apiezon type-L vacuum grease. Next to the TECs, we have placed the calibrated NTCs and each TEC's temperature is therefore independently controlled. Additionally, NTC sensors are placed on top and bottom of the cradle, on top of the screen and on the baseplate of the vacuum chamber. The temperature of each "foot" of the thermal screen can be controlled at the mK level.

The time constants  $\tau_{sc}$  and  $\tau_{cu}$  of the heat exchange between the screen and the cradle and between the cradle and the ULE cavity have been measured with the LTF-ULE1 system and they are at the order of 6 days and 1 day, respectively [59]. These were long-term measurements, and the laser had to remain locked to the cavity for long periods of time. Changing the temperature of the cavity with such a long time constant is the process that takes  $\sim 20$  days ( $3\tau$  principle). One of the goals with the LTF-ULE2 system was to make the temperature control more flexible. Somewhat arbitrarily, we decided to strengthen the demand on the temperature margin to  $\pm 5$  mK. In other words, we consider that the temperature step has been made when the monitored temperatures reach the values within 5 mK from their new set values. With this criterion in mind and without the active temperature control, the time for the realization of the temperature step for the ULE cavity rises to more than 30 days. The next section is therefore devoted to the modeling of the system thermal behavior, with the intention to reduce this very long

time.

## 4.6 Thermal model of the cavity enclosure

Figure 4.10 shows the cross-section of the vacuum system, with the cavity placed inside the two-layer enclosure.

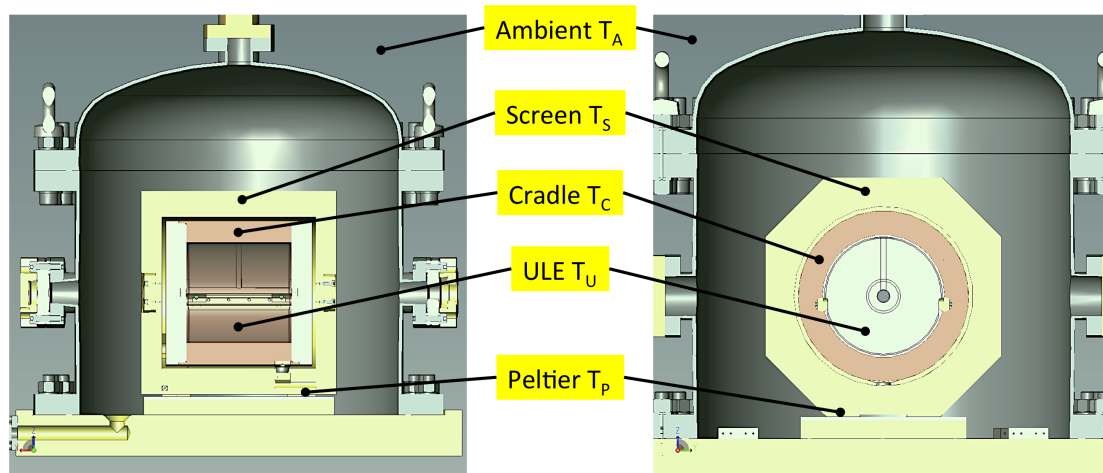


Figure 4.10: Cross-section of the vacuum chamber with the ULE cavity in place.

This system can be represented with the equivalent electrical circuit (Figure 4.11) [61], if the physical quantities of interest can be related to equivalent electrical quantities. For the purpose of modeling, the heat flow can be represented as the flow of the electrical current, thermal resistance between two physically contacted objects or between the objects engaged in the radiative heat exchange, corresponds to the electrical resistance, thermal capacity of each part to the electrical capacity and the temperature corresponds to the voltage.

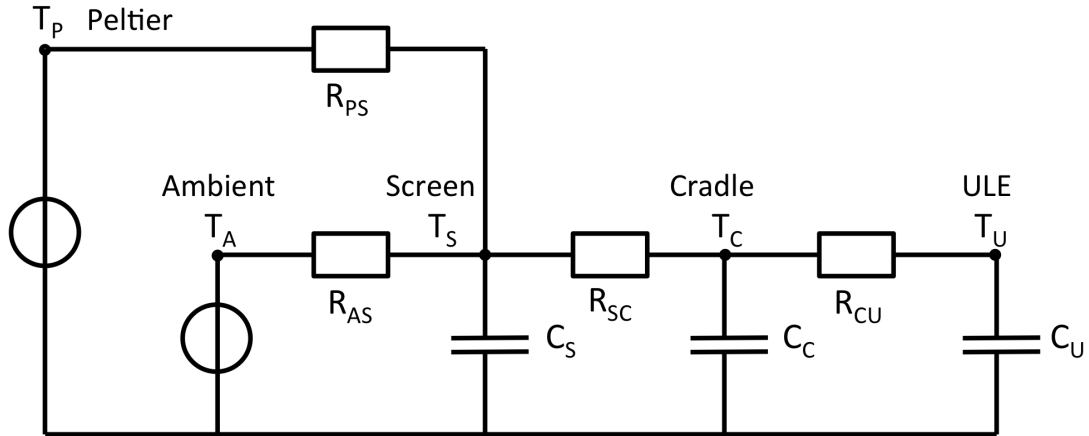


Figure 4.11: Equivalent electrical circuit of the cavity and its thermal enclosure. The following mapping is considered: heat flow  $\leftrightarrow$  electrical current flow, thermal resistance between the objects (both for the radiation and for the conduction)  $\leftrightarrow$  electrical resistance, thermal capacity  $\leftrightarrow$  electrical capacity and temperature  $\leftrightarrow$  voltage.

#### 4.6.1 Thermal properties of the system components

We analyzed the logical subsections of the system, with the ultimate goal of setting up the temperature control in a way that would enable us to change the temperature of the cavity in a convenient amount of time (within days instead of few tens of days). It is therefore necessary to determine the basic thermal properties of all of the components present in the model and to calculate the equivalent electrical quantities. For that matter, in terms of the heat exchange, we think about the ULE cavity, its Cu cradle and Al screen as of three spheres encircling each other, while the areas of the spheres are calculated from the dimensions of the actual cylindrical shape of these elements. In the similar manner, the masses of the spheres are equal to the masses of the corresponding objects. Table 4.1 [61] summarizes the physical properties of the materials present in the vacuum chamber.

The whole system can be divided in two parts. The first "passive"

<b>Material</b>	<b>Specific heat</b> $c \left[ \frac{J}{kg \cdot K} \right]$	<b>Thermal conductivity</b> $\kappa \left[ \frac{W}{m \cdot K} \right]$	<b>Density</b> $\rho \left[ \frac{kg}{m^3} \right]$
Al	904	235	2700
Cu	384.4	400	8920
ULE	767	1.31	2210

Table 4.1: Physical characteristics of the materials used for the mechanical parts [61].

subsystem consists of the thermal screen, cradle and the ULE cavity. The heat between the elements of this subsystem is exchanged by radiation and by conduction through the contact points, since the molecular conduction can be neglected at the pressure levels  $\sim 10^{-7}$  mbar. Nevertheless, in the thermal model, the contact conduction exchange is also ignored, since it has been estimated that the conduction thermal resistance is  $\sim 5$  times higher than the resistance for the radiative heat exchange [59]. The second "active" subsystem comprises the four Peltier elements and the thermal screen, whose temperature is monitored and adjusted by a home made temperature controller, capable of stabilizing the Peltier elements' temperature at the level of mK.

For the analysis of the subsystem consisting of the Al thermal screen, Cu cradle and the ULE cavity, we need to know the thermal capacity ( $C^{th} = m \cdot c$ ) of each one of them (Table 4.2). The emissivity of the surface depends on the material as well as the quality of the surface. In Table 4.3 [61] we summarize the values of the emissivities that were used in the thermal model.

Heat flowing from one surface to another is the sum of the heat emitted by the surface and of the heat reflected from it

$$P_{int \rightarrow ext} = \varepsilon_{int} S_{int} \sigma T_{int}^4 + (1 - \varepsilon_{int}) P_{ext \rightarrow int} \quad (4.16)$$

$$P_{ext \rightarrow int} = \varepsilon_{ext} S_{ext} \sigma T_{ext}^4 + (1 - \varepsilon_{ext}) P_{int \rightarrow ext} \quad (4.17)$$

where  $\varepsilon$ ,  $S$  and  $T$  are the emissivity, the area and the temperature of the corresponding surface. Heat exchange of two concentric spheres

	Screen	Cradle	ULE
$\mathbf{r}_{ext}$ [cm]	10	7	5
$\mathbf{r}_{int}$ [cm]	7.5	5	-
$\mathbf{l}_{ext}$ [cm]	20	14	10
$\mathbf{l}_{int}$ [cm]	15	10	-
$\mathbf{m}$ [kg]	9.81	12.22	1.74
$\mathbf{C}^{th}$ [ $\frac{J}{K}$ ]	8866	4697	1331

Table 4.2: Dimensions (radius and length), masses and thermal capacities of the elements of the subsystem cavity - thermal enclosure, used in the thermal model. The screen and the cradle are hollow cylinders with external and internal dimensions, while the ULE cavity is a full cylinder.

	steel	Au	Cu	ULE
<b>Emissivity</b> ( $\varepsilon$ )	0.15	0.035	0.07	0.92

Table 4.3: Emissivities of the surfaces involved in the radiative heat exchange [61].

can be expressed as a difference of the heats passing from the internal towards the external surface and in the opposite direction. When this system of equations is solved and simplified, the transferred heat can be expressed as

$$P_{trans} = P_{ext \rightarrow int} - P_{int \rightarrow ext} = \frac{\varepsilon_{ext}\varepsilon_{int}\sigma(S_{ext}T_{ext}^4 - S_{int}T_{int}^4)}{\varepsilon_{ext} + \varepsilon_{int} - \varepsilon_{ext}\varepsilon_{int}} \quad (4.18)$$

After linearization [62] around the room temperature  $T_0 = 300$  K, while keeping in mind that  $P_{trans}$  is equivalent to the electrical current and that the temperature corresponds to the voltage, the thermal conductivity is given by

$$\kappa = \frac{dP_{trans}}{dT_0} = \frac{\varepsilon_{ext}\varepsilon_{int}\sigma S \cdot 4T_0^3}{\varepsilon_{ext} + \varepsilon_{int} - \varepsilon_{ext}\varepsilon_{int}} \quad (4.19)$$

Finally, thermal resistance at room temperature is calculated as the inverse of the thermal conductivity (Table 4.4).

	Chamber-Screen	Screen-Cradle	Cradle-ULE
$R^{th} \left[ \frac{K}{W} \right]$	52.7	86.5	49.8

Table 4.4: Thermal resistances of the radiative heat exchange between the elements of the cavity thermal enclosure (vacuum chamber included).

## 4.6.2 Thermal dynamics and active temperature control

With the static parameters determined, and with the assumption that the screen temperature  $T_s(t)$  can be externally imposed, it is now possible to make a dynamic model and to determine the time constants of the heat transfer between various subsystem elements.

From the electrical scheme in the Figure 4.11 it follows that

$$C_c^{th} \frac{dT_c(t)}{dt} = \frac{T_s(t) - T_c(t)}{R_{sc}^{th}} - \frac{T_c(t) - T_u(t)}{R_{cu}^{th}} \quad (4.20)$$

and

$$C_u^{th} \frac{dT_u(t)}{dt} = \frac{T_c(t) - T_u(t)}{R_{cu}^{th}}, \quad (4.21)$$

where the indices  $c$ ,  $s$  and  $u$  correspond to the cradle, the thermal screen and the ULE cavity, respectively. This system of two first order ordinary differential equations can be represented by a state space model i.e. a single, first order, but matrix differential equation. From the eigenstates of the state space model, evaluated with previously determined static thermal parameters, we can derive the time constants of the system. By this model, the estimated time constant for the exchange of heat between the cradle and the ULE cavity is  $\tau_{cu}^{est} \sim 0.6$  days and between the screen and the cradle  $\tau_{sc}^{est} \sim 6.2$  days. Graphic representation of the model output for the system response to a 1 K step in the temperature of the screen is given in Figure 4.12.

The measured heat exchange time constant between the thermal screen and the cavity cradle (Figure 4.13) is  $\tau_{sc}^{exp} \sim 4.7$  days. There-

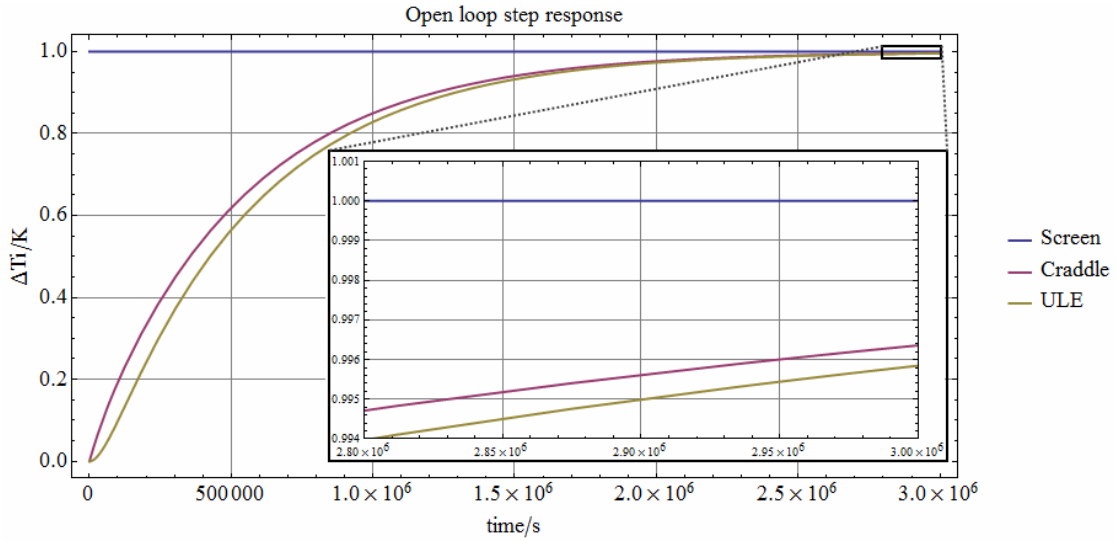


Figure 4.12: Response of the model to a 1 K step in the screen temperature. The estimated ULE cavity temperature reaches 5 mK margin from the set point in  $\sim 2.9 \times 10^6$  s ( $\sim 33.6$  d).

fore, the thermal model overestimates the time constant for  $\sim 32\%$ , which may be the consequence of taking into account only the radiative heat exchange and ignoring the contribution of the conduction through contact points between the elements of the thermal enclosure.

Based on the measured time constant between the screen and the cradle ( $\tau_{sc}^{\text{exp}} \sim 4.7$  d), and on the non-corrected estimated time constant between the cradle and the ULE cavity ( $\tau_{cu}^{\text{est}} \sim 0.6$  d), the time of the ULE cavity temperature change (5 mK margin criterion) is  $\sim 2.15 \times 10^6$  s ( $\sim 24.9$  d). Possible error in the  $\tau_{cu}^{\text{est}}$  is of no significance for this calculation, since its influence on the result would be noticeable (and still with little significance) only if it had the value at the order of days.

Contrary to the first subsystem, where we ignored all of the conductive heat exchanges, in the subsystem consisting of the Peltier elements and the thermal screen a conductive exchange between them is taken into account, acting in parallel with the radiative heat exchange between the ambient heat tank and the thermal screen. The

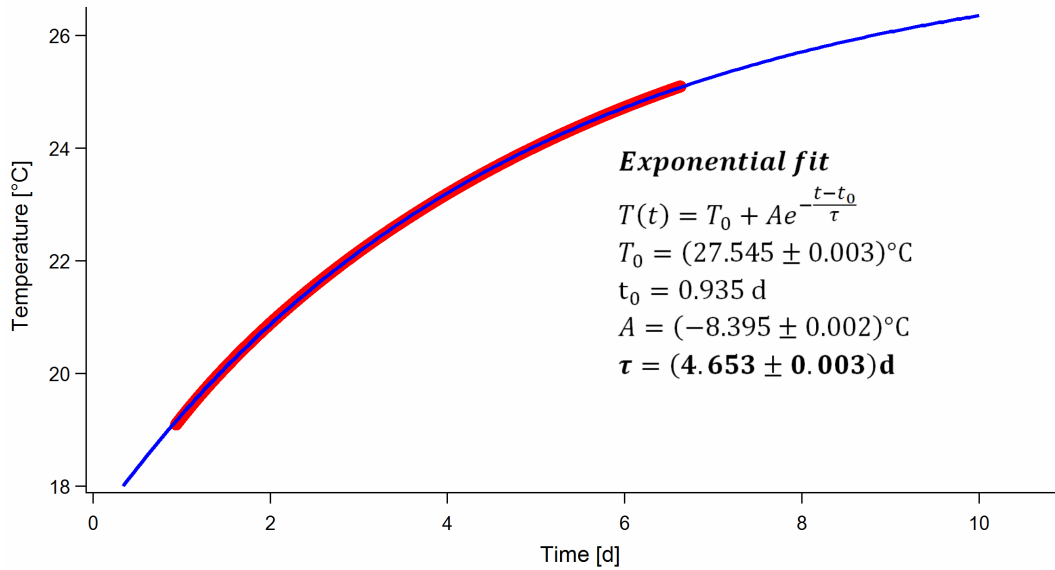


Figure 4.13: Experimental determination of the time constant ( $\tau_{\text{sc}}^{\text{exp}} \sim 4.7$  days) of the heat exchange between the screen and the cradle. The red trace represents the measured evolution of the cradle temperature (mean value of the top and bottom cradle NTC readout) for a 10 K step in the screen temperature. The blue trace represent an exponential fit.

model of these exchanges is simpler

$$C_s^{th} \frac{dT_s(t)}{dt} = \frac{T_0 - T_s(t)}{R_{as}^{th}} + \frac{T_p(t) - T_s(t)}{R_{ps}^{th}}. \quad (4.22)$$

Based on this model, the screen should follow the change in the TEC temperature with the delay of  $\sim 5000$  s [61].

The simplest approach to the ULE cavity temperature manipulation would be to set the temperature of each TEC and wait during approximately one month, but this is very inconvenient. Nevertheless, it was possible to upgrade the temperature controller software, with the introduction of the secondary slow stabilization loop. Schematics of the implemented dual control is shown in Figure 4.14.

In order to determine the operating parameters of this additional (slow) proportional-integral-differential (PID) loop, we introduced the model of this loop in our program, where we connected it in series with the model of the screen-cradle-ULE cavity subsystem. The slow



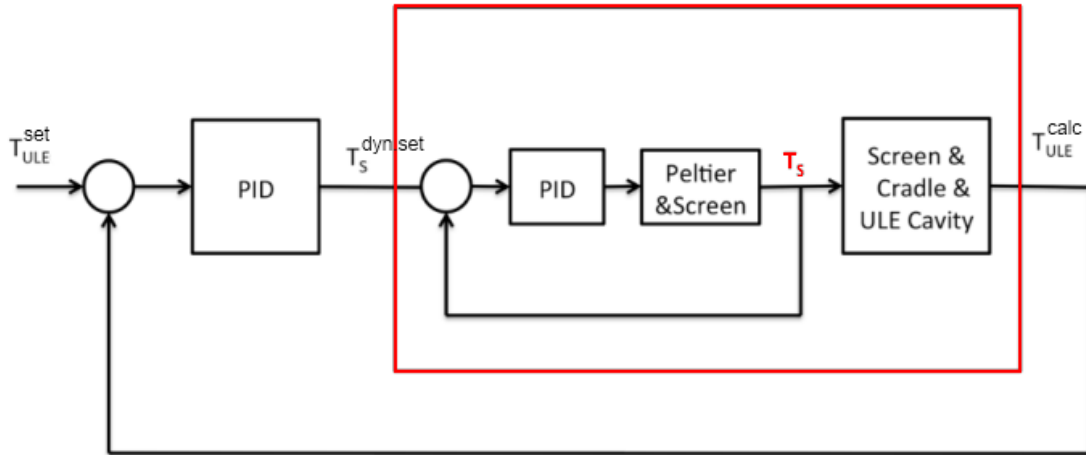


Figure 4.14: Fast (red rectangle) and slow temperature control loops. The dynamic set point  $T_s^{dyn.set}$  of 4 TECs is determined by the slow loop. The fast temperature control is applied for each TEC in a separate loop.  $T_{ULE}^{calc}$  is calculated from the closed loop response of the thermal model.

loop is responsible for the control of the temperature of the thermal screen. In the time frame of a few hundreds of thousands of seconds, the change of the screen temperature (induced by Peltier elements) that takes place with the time constant of a few thousand seconds, can be considered as immediate. Therefore, the output of the slow loop is used as a dynamic set point for the "standard" (fast) PID loop which controls the temperatures of the four Peltier elements.

Since it is not possible to measure the temperature of the ULE cavity, the error signal upon which the slow loop acts is the difference between the set ULE cavity temperature and the temperature of the cavity estimated from the model (4.20-4.21). By trial and error we found the values of the  $k_P$ ,  $k_I$  and  $k_D$  gains of the slow loop, which shaped the evolution of the thermal screen temperature, in a way that a 1 K change of the estimated ULE cavity temperature (as far as the model is concerned) is made within a more convenient time span of  $\sim 3.5 \times 10^5$  s (Figure 4.15).

As the experimental illustration of the outcome of the previous analysis, the evolution of the measured cradle temperatures during

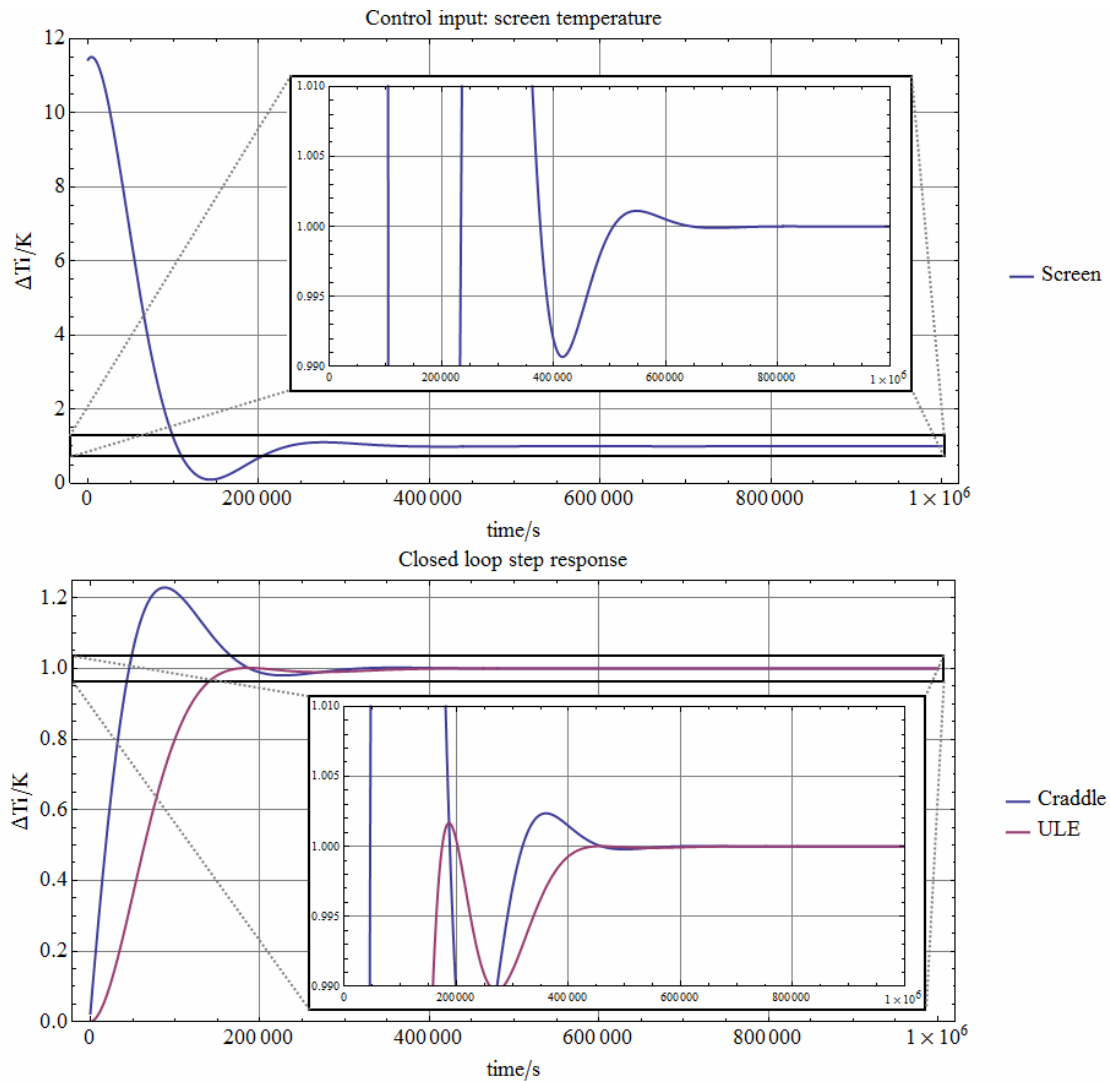


Figure 4.15: Response of the thermal model to a change in the screen temperature, shaped by the additional slow loop, in a way which enables the change of 1 K in the ULE cavity temperature within 4 days.

one of the changes of the ULE cavity temperature is displayed in Figure 4.16.

The cradle temperature is monitored by the two NTCs (cradle up and cradle down), while the temperature of the cavity is estimated from the model. An order of magnitude difference between the  $\tau_{sc}$  and the other time constants in the system means that, amongst all of the temperatures in the system, from the point of view of the

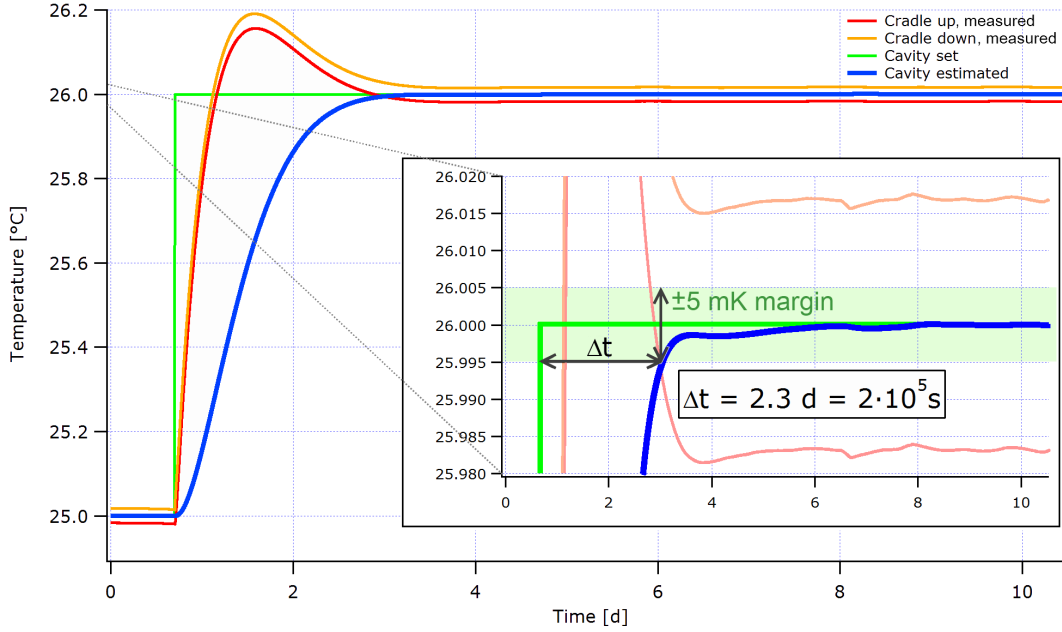


Figure 4.16: The evolution of the temperatures, during a +1 K step in the ULE cavity temperature, with the secondary slow control loop in action. The time for the estimated ULE cavity temperature to arrive within  $\pm 5$  mK margin from the new set point is reduced to  $2 \times 10^5$  s.

control, the most important is the temperature of the cradle. Once it gets under control and is made to change faster, the cavity itself will follow quickly, i.e. with much shorter time constant. The two values of the time needed for the temperature step to be made, without the advanced temperature control ( $\sim 24.9$  days) and with the additional slow loop in action ( $\sim 2.3$  days) show  $\sim 10$ -fold reduction in the system response time. The limiting factor in the system is the TEC current, with the maximum set to 2 A. In the model output on Figure 4.15, the proportional gain was 12 and with this parameter the TEC current was far from the limit. For the measurement that is displayed in Figure 4.16, we increased the proportional gain to 15, which, in addition to the difference between  $\tau_{sc}^{est}$  and  $\tau_{sc}^{exp}$ , resulted in the further decrease of the system response time and in the further mismatch of the model output and the experimental data.

Once the temperature of the zero coefficient of thermal expansion

(CTE) of the reference cavity has been determined (Section 4.9), the temperature controller was set to that value and all the system parameters were continuously monitored. One portion of the monitoring data, corresponding to  $\sim 25$  days is presented in Figure 4.17, with the indicated peak-to-peak variations of the sensors readouts.

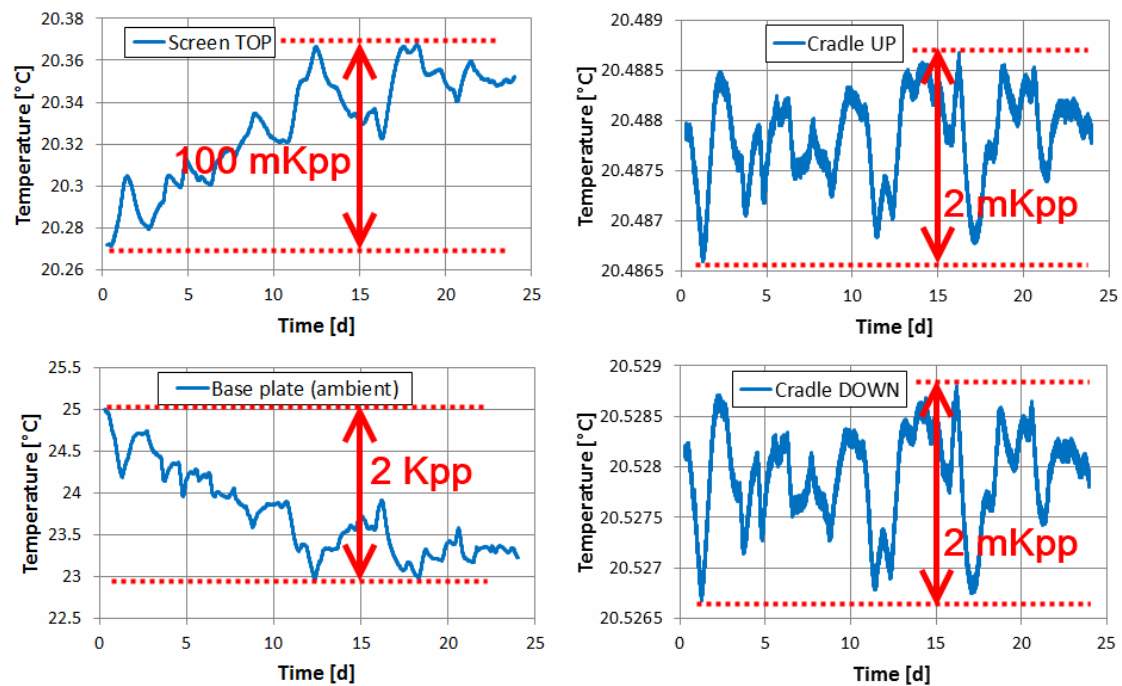


Figure 4.17: Temperature monitoring data during  $\sim 25$  day period, showing peak-to-peak temperature variations of the ambient, the thermal screen and the cradle.

The temperature of the vacuum chamber baseplate is used as the indicator of the ambient temperature variations. The baseplate and the thermal screen are in controlled thermal contact through four Peltier elements. Therefore, as the temperature of the screen is being stabilized, the flow of heat to or from the baseplate influences the readout of the baseplate sensor, and there is visible, scaled anti-correlation between the temperature of the thermal screen and the baseplate. Nevertheless, the cradle sensors show that the ULE cavity temperature stability, which is no worse than the temperature stability of the cradle, is at the aimed level of  $\pm 1$  mK, necessary for

the relative cavity resonant frequency fluctuations to be at the level of  $10^{-15}$  (Equation 4.23).

## 4.7 Optical setup

Figure 4.18 shows the schematics of the setup used for the realization of the laser stabilization to a high finesse rigid cavity.

The first diffraction order output of a fiber coupled, 40 MHz acousto-optic modulator (IntraAction FCM-460.8E5A), is taken to a fibered polarization beam splitter (POBS-15-3, AFW Technologies). One arm of the beam splitter is used to guide light further to the reference cavity, while the other arm is used as the stabilized laser output. The next element in the loop is the electro-optical modulator (EOM, model MPZ-LN-10, Photline Technologies) that phase modulates the incoming light. The modulation frequency is arbitrary, in a sense that it only should be high enough for the sidebands to lie outside of the reference cavity resonance, once the carrier is positioned at the top of the resonance. In this case, the modulation frequency was 21.4 MHz, only because of the possibility to easily band-pass filter that frequency, if necessary. From the output of the EOM, the light is collimated and then it reaches the free space part of the setup.

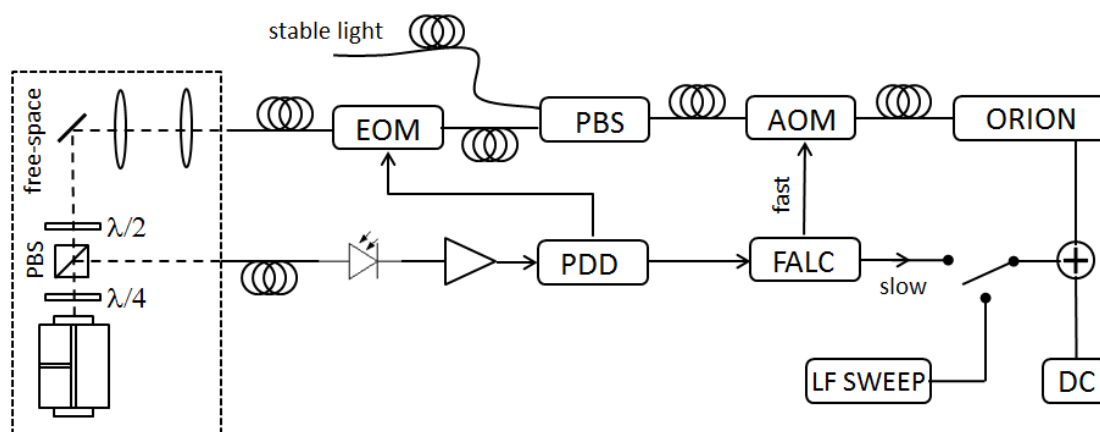


Figure 4.18: ORION<sup>TM</sup> laser stabilization to the LTF-ULE2 cavity.

The critical part for this experiment is the mode matching between the laser beam and the longitudinal mode of the reference cavity. The mode parameters of the cavity are defined by its geometry. The flat entrance mirror dictates that the incoming beam waist should coincide with the position of the coating of the first mirror and the second cavity mirror, positioned at  $L = 10$  cm distance with the radius of curvature of  $r = 50$  cm determines the size of the beam waist.

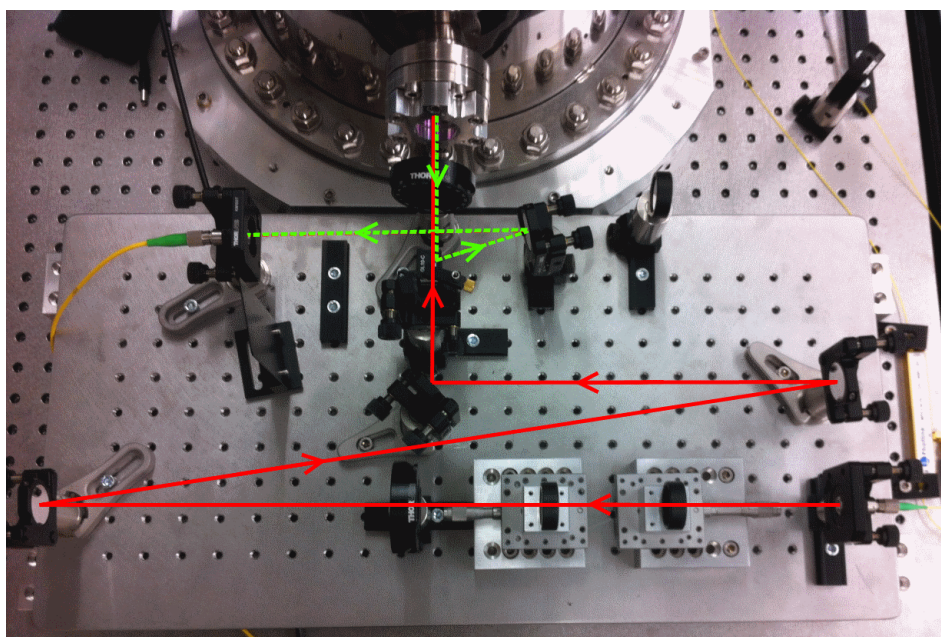


Figure 4.19: The free-space part of the setup, used for the injection of light in the reference cavity. Full red line shows the beam path before entering the cavity. Dashed green line shows the path in the reflection.

The free-space part of the optical setup is shown in Figure 4.19. All of the components are arranged on a relatively small breadboard (30 cm by 60 cm). A half-wave plate is placed after the two lenses of the mode-matching telescope (ThorLabs LF1015-C,  $f = -300$  mm and Thorlabs AC254-300-C,  $f = +300$  mm). Three folding mirrors are used in order to guide the beam towards the optical axis of the reference cavity and to adjust the length of the optical path (1604 mm), necessary for the mode-matching condition to be fulfilled. The next

element is a high power, high extinction factor Glan-Taylor calcite polarizer (ThorLabs GL10-C), enabling a very high polarization purity of 100000:1. Quarter-wave plate is the last optical element before the vacuum chamber that houses the reference cavity. Typical power injected into the cavity is  $\sim 50 \mu\text{W}$ . The back reflected light passes once more through a quarter-wave plate and reaches the Glan-Taylor polarizer, now with the polarization rotated by  $90^\circ$ , thus being reflected off the cube. Finally, the light is coupled into a fiber and taken to a fiber-coupled photodetector (ThorLabs DET01CFC).

On the back side of the cavity, one folding mirror, a lens and a variable gain photodetector (ThorLabs PDA10CS-EC) are used to detect the transmission signal.

## 4.8 Closing the loop

After theoretical analysis and physical building of the experiment, it takes a lot of time to eliminate all of the problems, to tune numerous parameters and to finally have the setup running. Therefore, although it is not usually the case, I will give a bit of a technical insight in the process of the setup of the laser stabilization loop.

The electronic part of the stabilization loop starts from the Topica PDD110f module. Its RF output is at 21.4 MHz and is used to drive the EOM. After the optical part of the experiment, when the reflected light from the reference cavity is detected with the photodetector, the signal is amplified by FEMTO<sup>®</sup> HCA-200M-20K-C transimpedance amplifier and taken back to the PDD110f module for demodulation. For the proper Pound-Drever-Hall signal (dispersive signal, in quadrature with the modulation signal), it might be necessary to compensate for possible phase shift, accumulated in the loop, for which purpose there is a phase setting potentiometer on the module. Demodulated output represents the error signal, which is then taken to a loop PID filter (Toptica FALC110). This PID controller has multiple configurable stages, so that its transfer function can be adjusted according to the system needs. The output of this

module is divided into the slow and fast branch. The slow branch is used to apply feedback to the ORION<sup>TM</sup> laser module, while the fast branch is connected to the modulation input of the AOM driver, which closes the stabilization loop.

Many parameters influence the performance of the stabilization, therefore some practice is necessary with the loop setup. FALC110 module takes some time to heat-up and to reach optimal functioning. That's why it is the best never to switch it off, which means that the control system is always trying to act on the laser (except the low-frequency unlimited integrator). If the servo was not in action, it would not have been possible to detect that the laser is within the stabilization loop capture range, i.e. this behavior is used to detect the resonance of the reference cavity. In order to see the P-D-H signal, laser has to be swept with low frequency. This is achieved by applying a triangular signal of appropriate amplitude to the laser tuning port. For fine tuning laser frequency a small DC voltage is also added.

In any position of the switch, used for the selection between the LF sweep and slow FALC110 output, the fast part of the loop is continuously acting on the AOM. When all of the FALC110 stages, its proportional gain and input offset are correctly set, the oscilloscope trace of the transmission signal starts to widen, fully correlated with the widening of the central part of the P-D-H error signal. Once all of the parameters are at the optimum, this temporary laser lock to the cavity resonance is manifested by the transmission signal with the shape shown in Figure 4.20. The input offset of the FALC110 module has to be set in a way that the bipolar error signal is symmetrically positioned relative to the zero level i.e. that the linear part of the error signal in the vicinity of the center of the cavity resonance, crosses zero.

FALC has two inputs, inverting and non-inverting. If the wrong input is chosen, the modulation sidebands will be locked to the cavity resonance during the sweep, in which case the spreading appears on the wings of the error signal and not in the center. In such a case



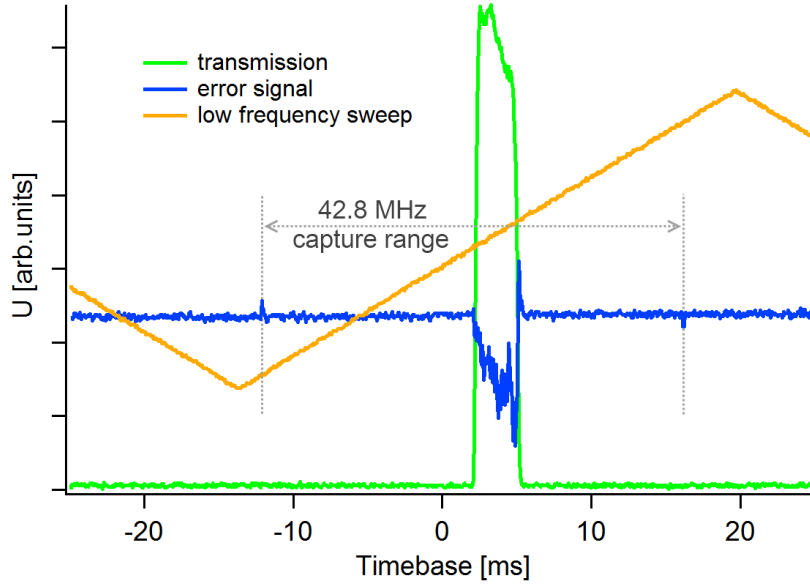


Figure 4.20: Shapes of the transmission (green) and error (blue) signals during laser frequency sweep (orange) that reflects the correct setup of the stabilization loop parameters. Wide and symmetric central part, with the maximum in the middle, indicates the proper parameters settings. Phase modulation sidebands ( $\Omega = 21.4$  MHz) are used for the frequency calibration.

the other input of the PID controller should be used.

With the sweep switched off, the laser frequency is slowly tuned by adding a small DC voltage, until the transmission signal reaches its maximum. This indicates that the frequency has been brought into capture range of the loop and that the fast branch of the loop is in action. It is also useful to monitor the correction signal at the output of FALC110 on a separate oscilloscope with a long timebase (roll mode of the time axis). By switching on the unlimited integrator of the FALC110 module and setting up its offset in a way that the rolling correction signal is centered around zero, the full stabilization is achieved. Figure 4.21 displays the spectrum of the correction signal. The servo bump at  $\sim 170$  kHz indicates the bandwidth of the stabilization loop. With the free running linewidth of the PW-ECL laser of the order or 10 kHz at 0.1 s observation time [59], the

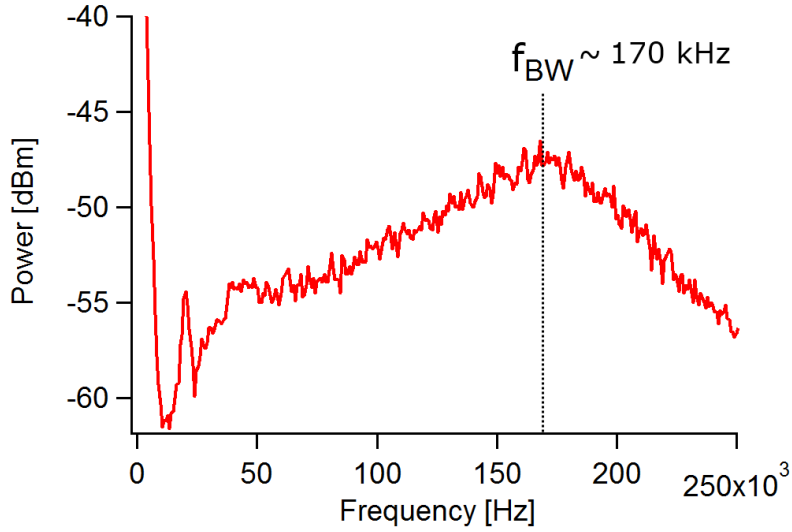


Figure 4.21: Electrical spectrum analyzer display of the correction signal, showing a servo bump around 170 kHz, which gives the idea of the stabilization loop bandwidth.

demonstrated bandwidth is sufficient for the laser stabilization to the cavity and in the absence of the external perturbations, the laser can stay locked during multiple hours.

## 4.9 High finesse Perot-Fabry reference cavity

The LTF-ULE2 optical cavity (Figure 4.22) is a 10 cm long ULE glass (Ti-doped silicate glass) cylinder (produced by AT Films, Boulder, Colorado, USA) with two optically contacted fused-silica (FS) mirrors, whose high reflectivity is centered at 1557 nm. The horizontal notched cavity, with the vibration insensitive design is based on the SYRTE development [63]. For such a hybrid material cavity, the zero coefficient of thermal expansion (CTE) temperature is few tens of kelvin lower than for the cavities fully made out of the ULE. Therefore, ULE rings (outer diameter 25.4 mm, inner diameter 6 mm, thickness 6.35 mm) are optically contacted on the back side

of each of the fused-silica mirrors. These rings compensate for the thermal deformations of the FS mirrors and by proper choice of the ring dimensions, the zero CTE temperature of the cavity as a whole can be tuned over as much as 30 K, bringing the operation back to a more convenient, room temperature region [64].

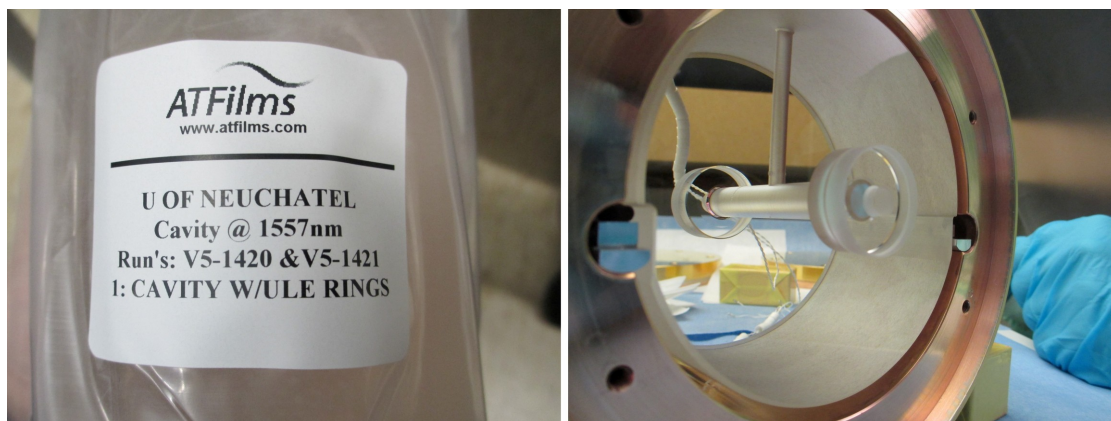


Figure 4.22: LTF-ULE2 notched optical cavity in protective package and placed in the cradle, resting on four Viton<sup>®</sup> support pads.

The entry cavity mirror is flat and the back mirror is concave, with the radius of curvature of 50 cm. The coating on the flat mirror has a radius of 8 mm, while on the curved mirror it is 12 mm, which is important to know for the proper orientation of the cavity.

### 4.9.1 Thermal noise limit

With the Pound-Drever-Hall stabilization scheme, the incoming laser field is locked to the averaged field resonating in the cavity. All of the fluctuation that are imposed on the length of the optical path inside the cavity, are directly transferred to the laser, as the residual frequency noise. The fundamental limit of the cavity length noise  $\sqrt{S_{\delta L}(f)}$  is set by the thermal noise (Brownian motion) of the cavity materials. Following the work of Numata et al. [60], we can estimate the thermal noise limit of the LTF-ULE2 reference cavity. The following parameters are used for this estimation: beam radius  $w_0 = 314 \mu\text{m}$ , mirror coating thickness  $d \sim 5 \mu\text{m}$ , temperature  $T =$

293.67 K (LTF-ULE2 cavity zero CTE temperature, see below), ULE spacer losses  $\phi_{\text{ULE}} = \frac{1}{6 \times 10^4}$ , FS mirror substrate losses  $\phi_{\text{FS}} = \frac{1}{1 \times 10^6}$  and mirror coating losses  $\phi_{\text{coating}} = 4 \times 10^{-4}$ , while Young's moduli and Poisson's ratios values are  $E_{\text{ULE}} = 67.6$  GPa,  $E_{\text{FS}} = 72.7$  GPa,  $\sigma_{\text{ULE}} = 0.17$  and  $\sigma_{\text{FS}} = 0.16$ . The results are summarized in Table 4.5.

Cavity	Spacer	Substrate	$\sqrt{S_{\delta L}(1 \text{ Hz})} \left[ \frac{\text{m}}{\sqrt{\text{Hz}}} \right]$	$\sqrt{S_{\delta \nu}(1 \text{ Hz})} \left[ \frac{\text{Hz}}{\sqrt{\text{Hz}}} \right]$	$\sigma_y(\tau = 1 \text{ s})$
LTF-ULE1 [59]	ULE	ULE	$5.5 \times 10^{-17}$	0.11	$6.5 \times 10^{-16}$
LTF-ULE2	ULE	FS	$2.9 \times 10^{-17}$	0.056	$3.5 \times 10^{-16}$

Table 4.5: Comparison of the thermal noise limitations of the two ULE cavities. The displacement noise  $\sqrt{S_{\delta L}(f)}$  and the corresponding frequency noise  $\sqrt{S_{\delta \nu}(f)}$ , both exhibiting flicker behavior, are estimated at 1 Hz Fourier frequency. The estimated thermal noise limit of the fractional frequency stability  $\sigma_y(\tau)$  (Allan deviation) is given for the integration time of 1 s.

The total cavity displacement noise power spectral density ( $S_{\delta L}(f)$ ) comprises contributions of the two cavity spacer flat ends, two mirror substrates and two mirror coatings, with the estimated partial contributions (at 1 Hz Fourier frequency) of 0.6%, 14.6% and 84.8%, respectively.

## 4.9.2 Thermal expansion turning point

The LTF-ULE1 cavity is a full ULE design [42], with the inversion temperature of 22.46 °C, determined by application of heating and cooling temperature ramp to the baseplate of the vacuum chamber [59]. The temperature control described in Section 4.6 came in very useful for the determination of the temperature where the LTF-ULE2 cavity has a zero coefficient of thermal expansion (CTE). The determination of zero CTE temperature of the LTF-ULE1 cavity was a few months long process, because of the high level of the thermal isolation of the cavity placed in the two-layer thermal shield. With our second system, we were able to set the cavity temperature within

$\pm 5$  mK margin from the set temperature only in 2.3 days, which enabled us to determine the minimum of the cavity expansion from a set of discrete measurements. In other words, it was enough to set the temperature, wait for it to settle, lock the laser to the cavity and measure the frequency of the laser for some time.

The heterodyne optical beat between the laser and the 250 MHz Er:fiber optical frequency comb (MenloSystems, Germany) is detected by ThorLabs DET01CFC detector, amplified with FEMTO<sup>®</sup> DHPA-100 current amplifier and counted with FXM50 (K+K Messtechnik, Germany) zero dead time counter. The results of the four weeks of measurements, where we were able to set seven different cavity temperatures (starting from 25°C) are shown in Figure 4.23.

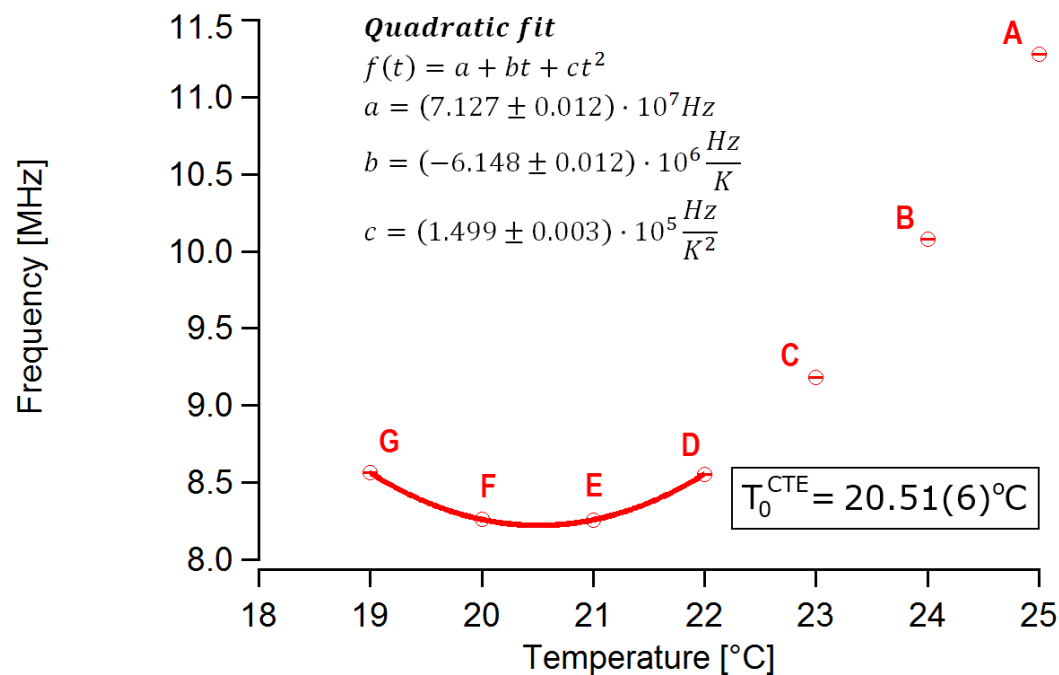


Figure 4.23: Static determination of the temperature inversion point of the LTF-ULE2 reference cavity.

The first three points (A, B and C) were used to check the trend of the change, as well as to make the first estimate of the zero expansion temperature. Afterwards, we used the four points (D, E, F and G), symmetrically distributed around the curve minimum for the

quadratic fit, showing the zero CTE temperature at  $T_0^{\text{CTE}} = (20.51 \pm 0.06)^\circ\text{C}$ . With the cavity temperature set to this value, the residual quadratic relative frequency sensitivity is

$$\frac{\Delta f}{f} = 7.8 \cdot 10^{-10} [K^{-2}] \Delta T^2 \quad (4.23)$$

where  $\Delta T = T - T_0^{\text{CTE}}$  represents the difference between the actual cavity temperature and its zero CTE temperature.

### 4.9.3 Cavity drift

For the determination of the cavity drift, it is necessary to record the laser frequency evolution over a prolonged period of time, but it is also important to be sure that the change in frequency is indeed the consequence of the drift and not e.g. the result of the oscillations induced by the daily change in the ambient temperature. With the estimated error of  $\Delta T_0^{\text{CTE}} = 0.06$  K, and with the measured temperature difference of  $\sim 35$  mK between top and bottom of the cradle, we assume that the cavity set temperature is no more than  $\Delta T = 0.2$  K away from the exact zero CTE temperature. From the derivative of the curve in Figure 4.23 at the point 0.2 K away from the minimum, the cavity temperature sensitivity is estimated at  $\sim 60 \frac{\text{Hz}}{\text{mK}}$ . From the measured cradle temperature oscillations, at the order of 2 mKpp on a daily scale (Figure 4.17), we could expect to see the corresponding oscillation in the laser frequency of the order of 120 Hz peak-to-peak.

The beat frequency was recorded in stages during 400 thousand seconds. The measured frequencies are displayed in Figure 4.24, spanning  $\sim 14$  kHz during the observation time of  $\sim 4.5$  days, which is much more than the estimated ambient temperature induced frequency oscillations (120 Hz peak-to-peak). The cradle temperature monitoring data (Figure 4.17), recorded before, during and after the cavity drift measurements, excludes the possibility of the temperature instability influence on the ULE cavity. Therefore, we can say that the observed linear drift rate of  $\sim 31 \frac{\text{mHz}}{\text{s}}$  is not the consequence

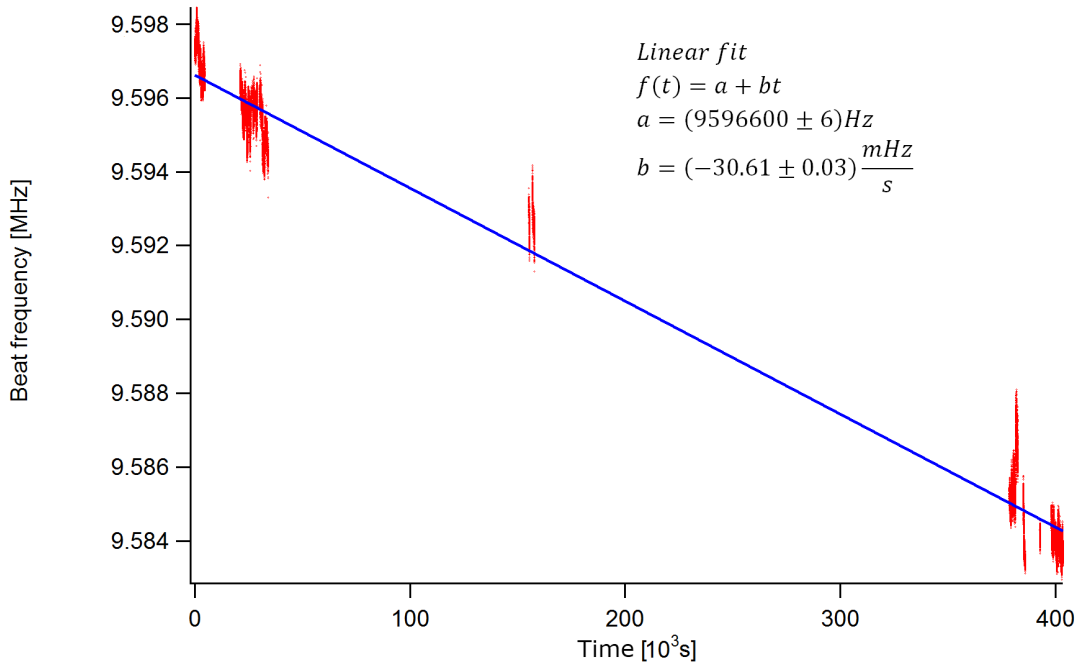


Figure 4.24: Measured cavity drift at zero CTE temperature, is in the accordance with the values reported [15] as the ULE material aging drift.

of the daily temperature variations and that it could be attributed to the cavity material aging or e.g. to the drift in the stabilization electronics. This value is comparable with the drift value of  $\sim 60 \frac{\text{mHz}}{\text{s}}$  reported in [15].

#### 4.9.4 FWHM resonance linewidth. Cavity ring-down time.

The full-width half-maximum (FWHM) linewidth of the cavity resonance can be determined from the cavity ringdown time  $\tau$  as

$$\Delta f_{\text{FWHM}} = \frac{1}{2\pi\tau}. \quad (4.24)$$

In order to measure the ringdown time, it is necessary to lock the laser to the cavity and to quickly cut-off the incoming light, while recording the DC signal on the photo detector in the cavity trans-

mission. Manual beam interruption as well as chopping is not fast enough, because the time of flight of the blade through the beam profile is comparable with the cavity decay time. The shape of the expected exponentially decaying DC signal becomes distorted. The simplest solution is to cut-off the AOM RF output signal and to trigger the scope on the falling edge of the transmission signal, which results in a confident measurement shown in Figure 4.25.

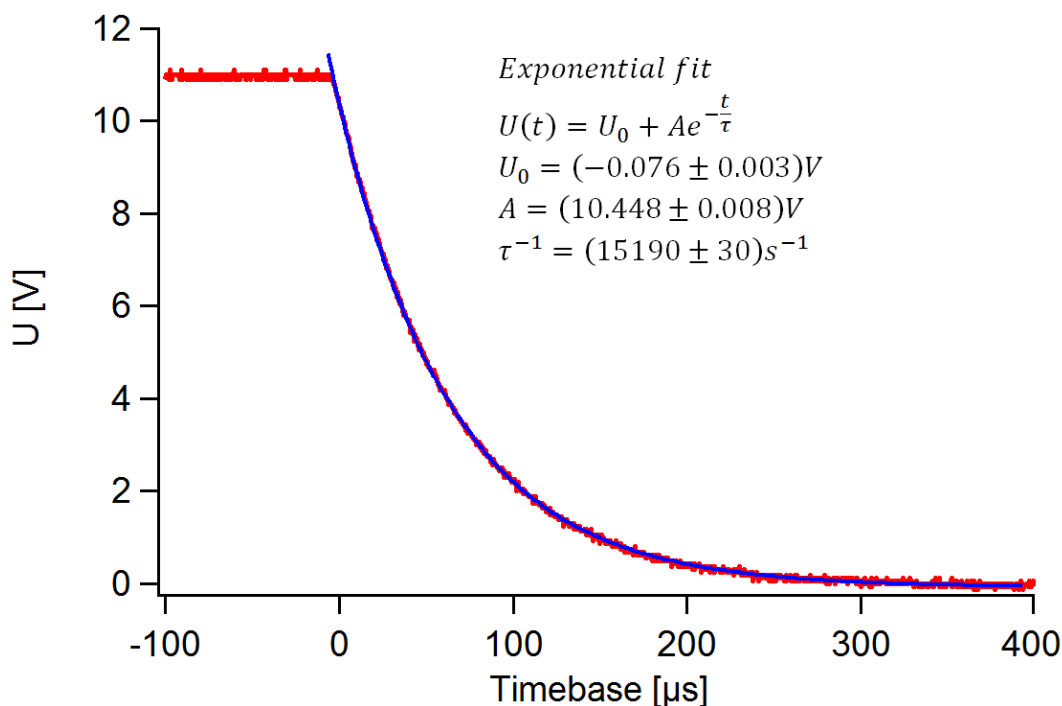


Figure 4.25: Measurement of the ringdown time for the LTF-ULE2 cavity. The signal decays with the time constant of  $\tau \approx 66\mu\text{s}$ .

The decay of the signal is characterized by the time constant of  $\tau^{-1} = 15191 \text{ s}^{-1}$  which in turn gives the resonance linewidth value of

$$\Delta f_{\text{FWHM}} = 2420 \text{ Hz.} \quad (4.25)$$

With the free spectral range of the 10-cm cavity being 1.5 GHz, the cavity finesse (Equation 4.10) is

$$\mathcal{F} = \frac{\text{FSR}}{\Delta f_{\text{FWHM}}} \approx 620000 \quad (4.26)$$



For the  $f_0 = c/\lambda_0 = 192.6$  THz, the resonator quality factor is  $Q = 8 \cdot 10^{10}$ . The finesse value represents more than 3-fold improvement in comparison with the first system, where measured finesse is  $\approx 178000$  and  $\Delta f_{\text{FWHM}} = 8.4$  kHz [42].

#### 4.9.5 Direct resonance profile measurement

The additional check of the results from the previous Subsection was done by the direct measurement of the LTF-ULE2 resonance profile. The scheme of the experiment is shown in Figure 4.26, while the resonance shape is displayed in Figure 4.27, together with the Voigt fit of the data.

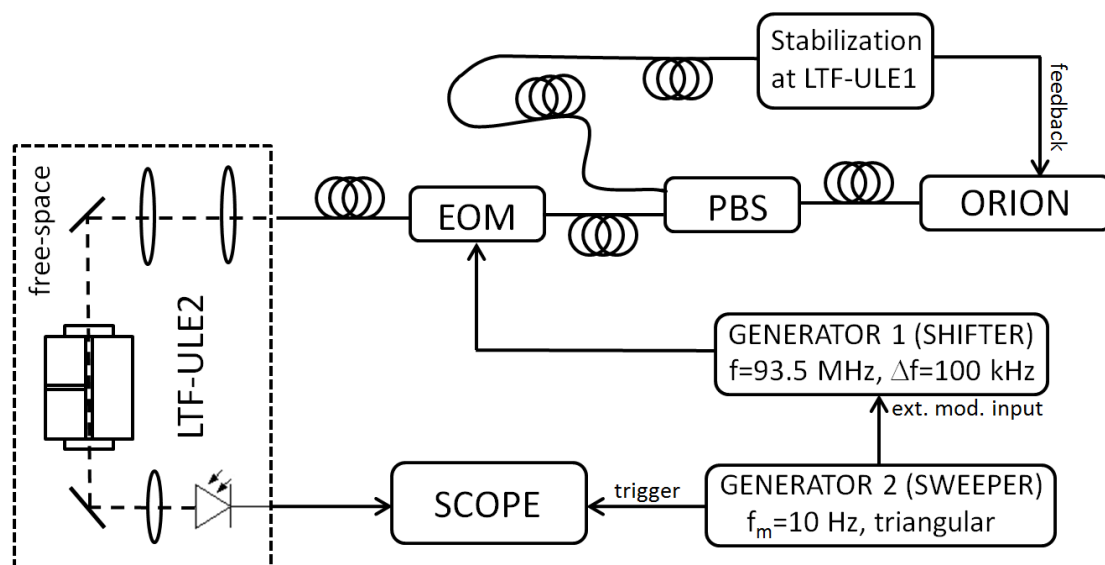


Figure 4.26: Setup for the direct determination of the resonance shape of the LTF-ULE2 cavity. The ORION PW-ECL is stabilized at the LTF-ULE1 cavity. The stabilized laser frequency is shifted by an EOM and swept through the resonance of the LTF-ULE2 cavity.

The laser was locked to the LTF-ULE1 cavity and an EOM (JDSU PM-150-005) is used to shift the laser frequency. The output of the frequency generator 1 is manually scanned in steps of 10 kHz, while being externally slowly swept by the frequency generator 2 ( $f_m = 10$  Hz, triangular,  $T=0.1$  s) with the modulation depth of

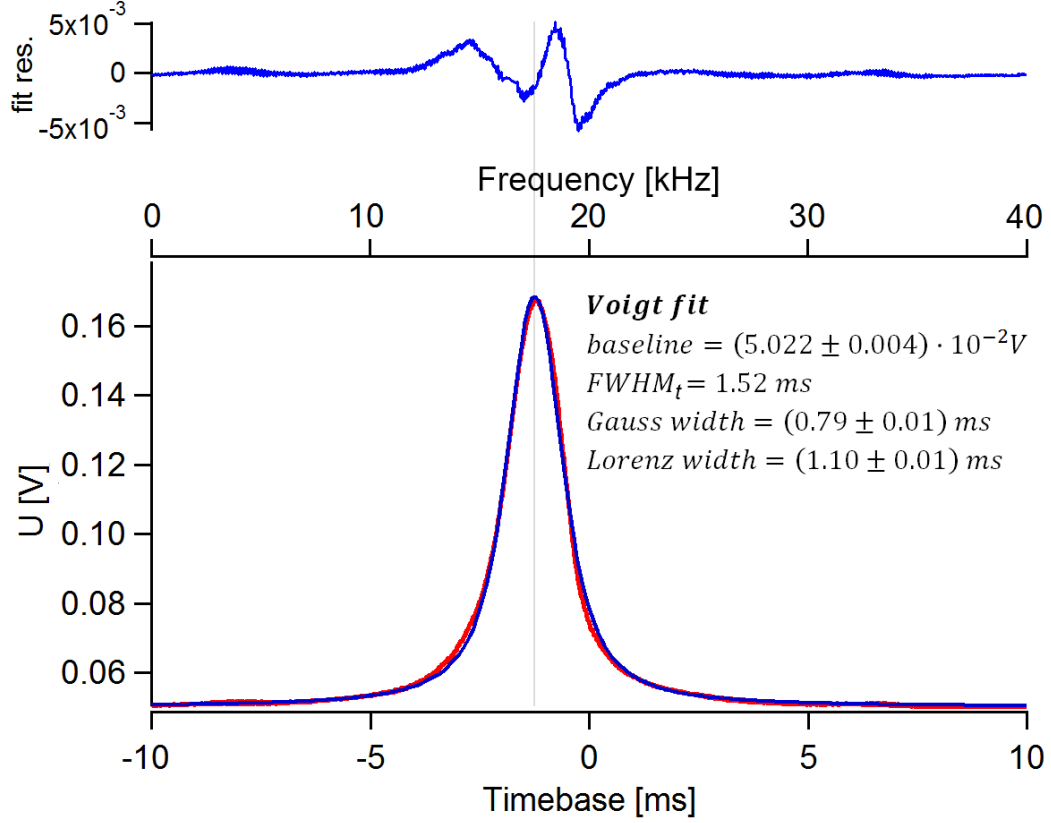


Figure 4.27: Resonance shape of the LTF-ULE2 cavity. Blue trace is the Voigt fit.

$\Delta f = 100$  kHz peak-to-peak. The transmission signal of the LTF-ULE2 cavity is monitored at the oscilloscope and the resonance was found 93.5 MHz away from the first cavity resonance. The linewidth of the cavity resonance is then simply calculated as

$$\Delta f_{\text{FWHM}} = \frac{\text{FWHM}_t}{T/2} \Delta f = 3040 \text{ Hz.} \quad (4.27)$$

The difference between this value and the value determined from the cavity ring-down time (4.25) is probably due to the distortion of the line shape caused by the ringing effect which has been noticed during laser sweep and explained independently by several authors [65–67].

## 4.10 Conclusion

In this Chapter I have described how we have implemented the Pound-Drever-Hall technique for the laser frequency stabilization. The building of the reference cavity housing was a personal challenge and I have in more detail mentioned important mechanical, thermal and optical aspects. We used the thermal model of the cavity enclosure [61] to develop the additional control mechanism, which enabled us to change the temperature of the ULE cavity within 2.3 days. This in turn brought substantial liberty in the process of the determination of the zero expansion coefficient temperature. I wanted also to add a few practical observations that could be of general help in similar activities. Finally I have presented the results of the characterization of the LTF-ULE2 cavity. After dozens of situations in the assembly process that could have deteriorated the performance of the system, it is satisfactory to see that very high finesse of 620000 is a reality.

# Chapter 5

## Er:Yb:glass oscillator (ERGO) optical frequency comb

### 5.1 Introduction

Optical frequency combs from mode-locked femtosecond lasers provide a direct, phase-coherent link between optical and microwave frequencies and allow the measurement of the optical frequencies with the highest precision [39, 68]. The possibility to easier count the optical frequencies has led to the development of the new generations of optical clocks that surpass microwave clocks in terms of the stability [69, 70].

The first self-referenced optical frequency combs were based on solid state Ti:sapphire lasers, providing high peak power [71, 72] and an octave spreading spectrum directly at the output of the femtosecond laser [73]. They can operate at a high repetition rate of several gigahertz [74] and also benefit from low-noise properties, resulting from high intracavity power i.e. high Q-factor of their optical resonator. Therefore, Ti:sapphire combs are still widely employed today, despite several disadvantages associated with their complexity, high cost and inefficient pumping. Later on, simpler

and cost-effective Er:fiber combs in the  $1.5\ \mu\text{m}$  region have been developed and self-referenced [75]. Being compact, robust and efficiently diode-pumped, Er:fiber combs have emerged as a valuable alternative to Ti:sapphire laser combs in the past years and now constitute a commonly-used comb technology. With the coverage of the  $1.5\ \mu\text{m}$  transmission window of optical fibers, it became possible to distribute the broad laser spectrum over large distances through proper noise-cancellation fiber links for simultaneous comparison of distant optical and microwave frequency standards [76]. In comparison to Ti:sapphire combs, fiber-laser combs generally exhibit significantly higher frequency noise and broader optical comb lines, due to their high gain, low Q-factor cavities and strong fiber nonlinearities. Significant improvements have been realized, in particular through the achievement of sub-Hz carrier-envelope offset (CEO) linewidth [77–81]. However noise suppression in fiber lasers remains more challenging and generally requires a wide feedback bandwidth in the 100 kHz range [78]. Notable exceptions are the Er:fiber comb developed at NIST operating with a reduced bandwidth of  $\sim 25$  kHz [82] and the multi-branch Er:fiber comb of Nakajima et al. that achieved a CEO beat linewidth of 10–30 kHz in the free-running conditions [80].

In an attempt to combine comfortable diode-pumping of the fiber lasers and low-noise operation of the solid-state lasers, diode-pumped solid state lasers (DPSSLs) [83] and more specifically, semiconductor saturable absorber mirror (SESAM)-modelocked DPSSLs have been developed [84]. DPSSLs have low intrinsic noise owing to their high-Q cavities with low residual losses and can access substantially higher average power levels than unamplified femtosecond fiber oscillators [85]. Repetition rates larger than 100 GHz have already been achieved in fundamental modelocking in the picosecond pulse width regime [86] and more recently larger than 1 GHz in the femtosecond regime [87, 88]. Despite the large number of femtosecond DPSSLs reported, CEO frequency detection has been demonstrated only occasionally, e.g. with a Kerr-lens modelocked 865 nm Cr:LiSAF laser

oscillator [89], a fiber-amplified, temporally compressed 1030 nm Yb:KYW laser [90], a SESAM modelocked Er:Yb:glass laser oscillator at 1.5  $\mu\text{m}$  [8], and most recently with a gigahertz diode-pumped Yb:KGW laser without any further amplification [91].

The subject of this chapter is an ultra-fast DPSSL, based on Er:Yb:glass gain medium, mode-locked by a SESAM [92]. This novel type of laser was lent to the Laboratoire Temps-Fréquence by the Keller group of the Institute of Quantum Electronics at ETH Zürich.

The characterization of the ERGO frequency comb includes the analysis of the stability and noise of the comb elements (carrier-envelope offset, repetition rate and a comb line at 1558 nm) in the free-running and phase-locked mode of operation. The assessment of the comb line properties is done by the frequency discriminator technique (Chapter 2), applied on the heterodyne RF beat between one of the comb lines and the cavity-stabilized ultra narrow linewidth CW laser (Chapter 4). It will be shown that the phase noise and the stability of the ERGO comb line are limited by the repetition rate reference oscillator. On the other hand, the contribution of the intrinsically low-noise CEO beat to the noise of the optical line is of no significance at all Fourier frequencies. A linewidth of  $\sim 160$  kHz is obtained for an optical comb line at 1558 nm.

Furthermore, I will discuss the influence of the dynamics of the CEO frequency ( $f_{\text{CEO}}$ ), controlled by a pump current, on the self-referencing of the ERGO optical frequency comb. The tuning of the  $f_{\text{CEO}}$  with the pump current exhibits a reversal point. Between the low- and high-frequency region in the dynamic response of the  $f_{\text{CEO}}$  to the pump current modulation, there is a significant phase shift of  $\sim 180^\circ$  in the transfer function. As a result, it is impossible to stabilize  $f_{\text{CEO}}$  at a pump current above the reversal point, although the free-running CEO beat at this point has a higher signal-to-noise ratio than underneath the reversal point, where the locking is straightforward. These results indicate that a high signal-to-noise ratio and a low-noise CEO beat are not sufficient indicators for the feasibility of the comb self-referencing in cases for which CEO dynamics plays

a dominant role.

## 5.2 75-MHz Er:Yb:glass ultra-fast laser

The layout of the Er:Yb:glass based frequency comb is given in the Figure 5.1. This passively mode-locked diode-pumped solid state laser is centered at 1558 nm, with the spectral width of  $\sim 15$  nm.

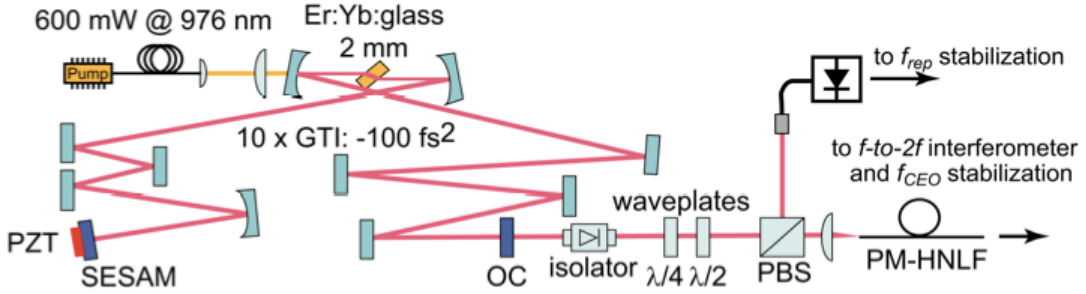


Figure 5.1: Layout of the diode-pumped Er:Yb:glass laser oscillator (ERGO). SESAM: semiconductor saturable absorber mirror; GTI: high reflection Gires-Tournois mirror, dispersion  $-100 \text{ fs}^2$  each; OC: output coupler; PBS: polarization beam-splitter cube; PM-HNLF: polarization maintaining highly nonlinear fiber.

For the detection of the CEO frequency a coherent octave spanning spectrum is generated in the 1.5 m long, dispersion flattened, polarization maintaining highly nonlinear fiber (PM-HNLF). The output of the laser consists of 170 fs Fourier transform limited pulses, emitted at the repetition rate of 75 MHz, with the average output power of 110 mW [8]. Two aspects of this ERGO laser are particularly advantageous, leading finally to the reliable and efficient operation. The first is the use of the SESAM for self-starting and stable soliton mode-locking [93], while the other one is the direct diode pumping by a 600 mW fiber-coupled telecom laser at 976 nm. Cavity length is coarsely tuned by a stepper motor which controls the position of the SESAM-carrying piezo transducer (PZT), itself responsible for the fine cavity length adjustment. High cavity

Q-factor and thus a significantly lower quantum noise limit, compared to a typical fiber-based laser [94], is a result of very low cavity round-trip losses, being below 3%.

The transportability of the ERGO laser is achieved by its placement on a 10 cm thick, 30 cm by 60 cm optical breadboard, while the improvement in its thermal and mechanical stability comes from the surrounding enclosure. The majority of the power is used for the coherent spectral broadening in the PM-HNLF and only a small portion is required for the detection and stabilization of the repetition rate frequency. Finally, a very silent CEO beat signal, with only 3.6 kHz free-running FWHM linewidth [8], is detected in the f-to-2f interferometer [30], at 1025 nm.

### 5.3 Frequency comb stabilization

The frequency comb is a frequency domain representation of a train of the femtosecond pulses. A very simple relation

$$\nu_n = f_{CEO} + n f_{\text{rep}} \quad (5.1)$$

shows that each optical frequency ( $\nu_n$ ), present in the comb spectrum, can be related to two RF frequencies  $f_{CEO}$  and  $f_{\text{rep}}$ . If the laser pulses were absolutely identical in terms of the envelope and the underlying carrier field, the comb spectrum would start at zero frequency and would be made out of the exact multiples of the repetition rate frequency. In reality, due to a difference in the velocities of the pulse envelope (group velocity) and the carrier field (phase velocity), a pulse-to-pulse phase shift is introduced and is registered as a frequency offset of whole of the comb spectrum from zero frequency. The stabilization of these two radio frequencies, results in the stabilization of whole of the optical frequency comb spectrum.

The repetition rate is phase-stabilized by custom MenloSystems RRE100 electronics. Less than 300  $\mu\text{W}$  of the femtosecond laser output power is injected into a single-mode fiber for the repetition rate detection. The 28<sup>th</sup> harmonic at 2.1 GHz is detected on a fast



photo diode (Thorlabs DET01CFC), band-pass filtered and compared in a double-balanced mixer with a reference signal, which is in this case a hydrogen maser referenced dielectric resonator oscillator (DRO, Miteq DLCRO-010-02100). The comparison at the 28<sup>th</sup> harmonic improves the sensitivity of the detection to phase fluctuations. On the other hand, the choice of this particular DRO, compared to a hydrogen maser reference, introduces a certain amount of the excess noise in the range from 2 Hz to 400 Hz. At the mixer output, the error signal is low-pass filtered, fed to a PI servo-controller after which the correction signal is amplified in order to be able to drive the cavity length PZT control.

Phase stabilization of the CEO beat to an external 20 MHz hydrogen maser reference is governed by a MenloSystems XPS800-E locking electronics. The most important component of this system is a digital phase detector DXD200 with a large linear phase difference detection range of  $\pm 32 \times 2\pi$  rad. The error signal is filtered and amplified in the loop PI controller (PIC201) and the feedback is applied to the pump laser current. The PI servo parameters are adjusted in a way that the residual CEO beat phase fluctuations are at the minimum, with the feedback bandwidth reaching the maximum, while the loop remains in the stable operation regime. Figure 5.2 is showing the total transfer function (both in amplitude and phase) of the CEO beat stabilization loop. It is derived from the measurements of the response of the each element of the loop i.e. DXD200 phase detector, PIC201 servo controller and the modulation response of the CEO beat itself. The loop unity gain frequency is only 5.5 kHz, with the phase margin of  $\sim 15^\circ$ . The feedback bandwidth in this case is mainly limited by the dynamics of the Er gain medium [95].

## 5.4 Stabilized CEO beat properties

With only the information on the CEO linewidth, its noise properties are not fully disclosed. The frequency noise power spectral density (PSD) is displaying the full noise information about the signal un-

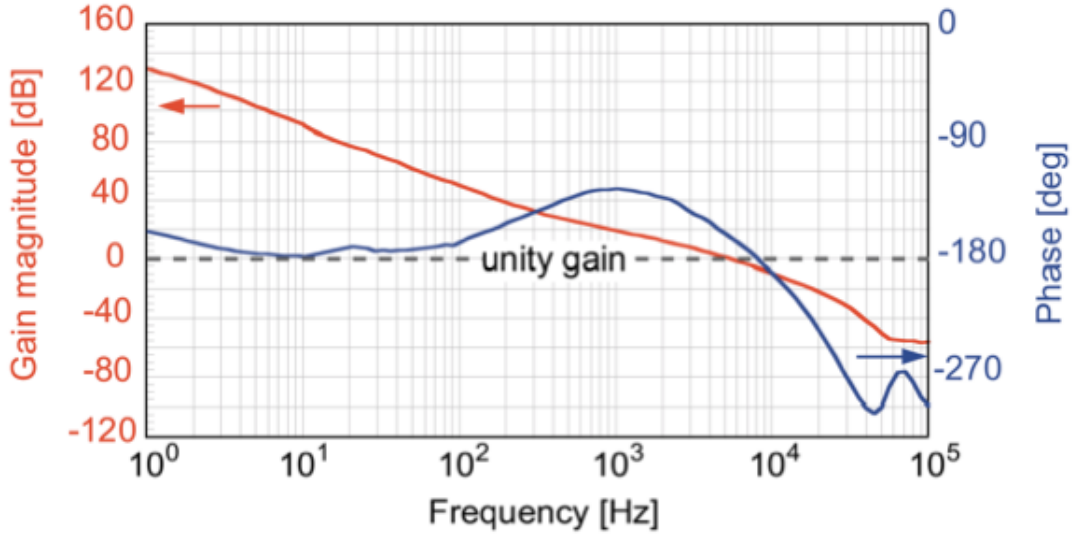


Figure 5.2: Amplitude and phase of the CEO beat stabilization loop.

der test. In this study the frequency noise PSD was measured by the use of the frequency discriminator technique, described in Chapter 2. Furthermore, in Chapter 3, it has been shown that the noise contribution to the linewidth comes only at the Fourier frequencies where the modulation is slow i.e. where  $S_{\delta\nu}^{\text{CEO}}(f) > \frac{8 \ln 2}{\pi^2} f$ .

The frequency noise PSD of the free-running CEO beat is displayed in Figure 5.4. The contribution to the linewidth comes from the noise at the Fourier frequencies below 3 kHz, which is the point of the intersection of the frequency noise PSD with the  $\beta$ -separation line. The linewidth is calculated from the frequency noise spectrum by Equation 3.3 and it increases with the observation time. The calculated value of  $\approx 5$  kHz at 1 ms observation time is in the agreement with the value of 3.6 kHz, extracted from the RF spectrum and previously reported in [8]. Very low-noise free-running properties of the CEO beat are making it possible to reach a tight phase-lock even with the feedback loop of limited bandwidth.

The frequency noise PSD of the phase-stabilized CEO beat, is measured from the in-loop error signal at the output of the DXD200 phase detector, with the detector measured sensitivity (Section 2.2.4)



Figure 5.3: CEO beat stabilization loop.

taken into account. The use of the in-loop signal is justified by the much lower phase noise of the maser reference. The level of noise suppression, displayed in Figure 5.5, is sufficient to give rise to a full CEO beat linewidth narrowing. The shape of the CEO coherent peak, with 30 dB signal-to-noise ratio at 30 Hz resolution bandwidth (inset in Figure 5.5) confirms the realization of a tight phase-lock.

The noise which remains present can be seen as a pedestal below the coherent peak. In order to quantify it numerically, an integrated residual phase noise is calculated as  $\Delta\phi_{\text{rms}}^{\text{CEO}} = \sqrt{\int \frac{S_{\delta\nu}^{\text{CEO}}(f)}{f^2} df} = 0.72$  rad-rms, integrated from 0.1 Hz to 100 kHz. This represents the lowest residual phase noise value for an optical frequency comb in the  $1.5 \mu\text{m}$  region, achieved with such a small feedback bandwidth of only  $\sim 5.5$  kHz.

Figure 5.5 shows that the main contribution to the residual integrated phase noise comes from the 5.5 kHz servo bump. Also, a small technical contribution of  $\sim 10\%$  originates from the peak at 360 Hz, which is visible in the frequency noise spectrum as well. This peak corresponds to a mechanical resonance in a translation stage

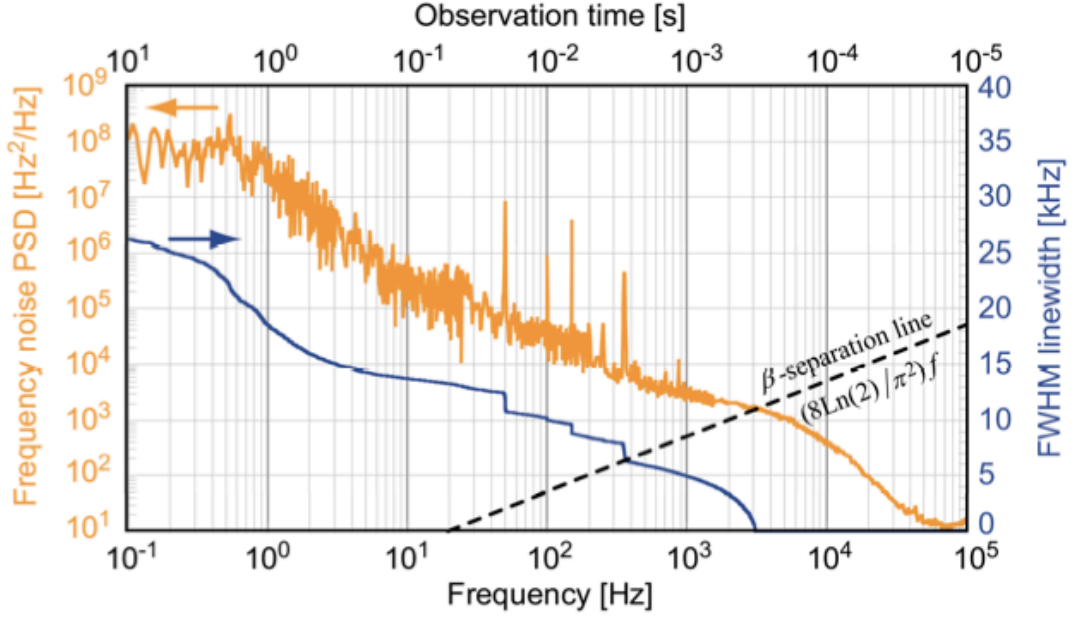


Figure 5.4: Left scale: Frequency noise PSD of the free-running ERGO comb CEO beat. The demodulation of a 20 MHz signal is done by a frequency discriminator technique. The  $\beta$ -separation line is used to determine which Fourier frequency region contributes to the CEO beat linewidth. Right scale: FWHM linewidth of the free-running CEO beat, calculated (see Equation 3.3) from the frequency noise spectrum, as a function of the observation time.

of the pump laser focusing lens. The residual phase noise could be further reduced by the improvement of the mechanical stability of the resonator or by introduction of an additional phase-lead filter in the feedback loop, which would extend the loop bandwidth [79].

For the analysis of the phase-locked CEO stability, its frequency was recorded with a zero dead time counter (K+K Messtechnik, FXM50). Figure 5.6 (a) shows a time series of the  $f_{\text{CEO}}$  during more than 10 hours of the stable ERGO operation. The Allan deviation (Figure 5.6 (b)) shows a fractional frequency instability at the level of  $10^{-8} \times \tau^{-1}$  of the 20 MHz CEO beat frequency, with the contribution at the level of  $10^{-15}$  to the optical carrier frequency instability ( $\nu_n = 200$  THz) at 1 s integration time. Furthermore, the comparison with the  $f_{\text{CEO}}$  of the Er:fiber frequency comb (Men-

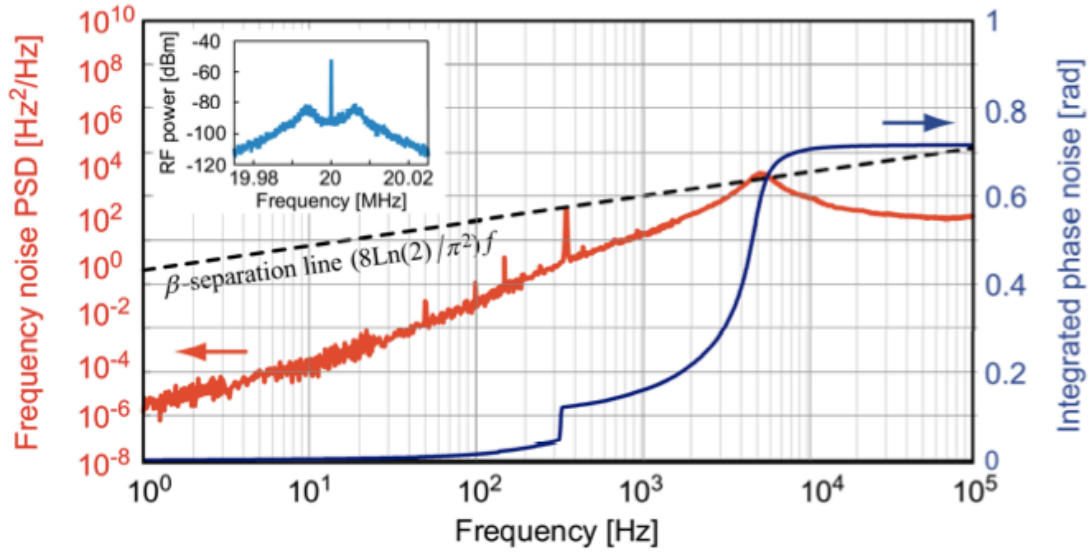


Figure 5.5: Left scale: frequency noise PSD of the phase-locked CEO beat, measured from the in-loop error signal at the output of the phase detector. Right scale: integrated residual phase noise (integration from 0.1 Hz up to the cut-off frequency). Inset: CEO beat RF spectrum, showing a coherent peak with 30 dB signal-to-noise ratio at 30 Hz resolution bandwidth.

loSystems FC1500-250) shows a 20-fold improvement in the CEO fractional frequency stability. For this comparison, both systems were in their best operating conditions, i.e. the feedback was acting within the full bandwidth, without any artificial limitations. Three times higher repetition rate (250 MHz in Er:fiber comb vs. 75 MHz in the ERGO) is partially responsible for this difference, but the main improvement factor is the larger Q-factor of the ERGO laser resonator.

Very recently, a new stabilization technique was successfully applied with this ERGO laser [96]. The SESAM was used as a fast intra-cavity opto-optical modulator (OOM), resulting in more than 10-fold increase in the CEO control bandwidth. The residual CEO phase noise was further reduced, from  $\sim 720$  mrad to only  $\sim 65$  mrad (integrated from 1 Hz to 100 kHz), resulting in a 4 times better CEO fractional frequency stability of  $2.5 \times 10^{-9}$  at 1 s integration time.

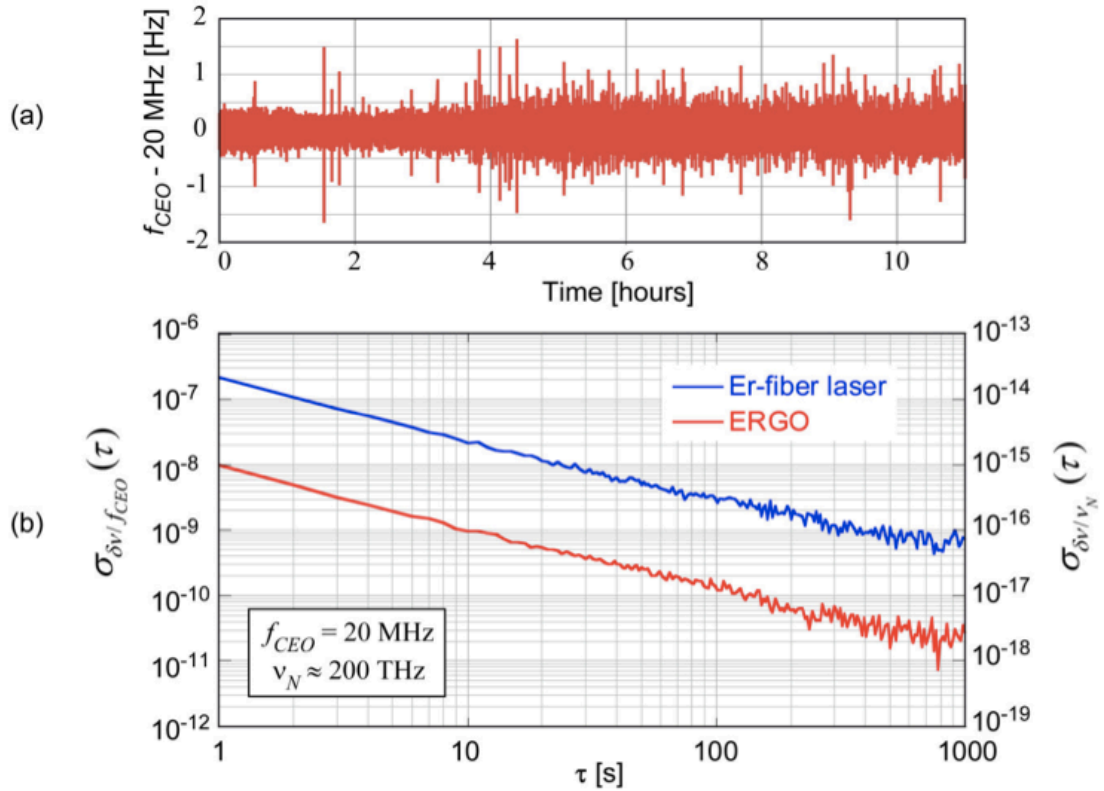


Figure 5.6: (a) Time series of the  $f_{CEO}$  measured with a zero dead time counter FXM50. (b) Allan deviation of the ERGO comb  $f_{CEO}$ , compared to a self-referenced Er:fiber comb. The left scale shows the fractional frequency stability with respect to the 20 MHz  $f_{CEO}$ , while on the right the scale is chosen in relation to the optical frequency  $\nu_n = 200$  THz.

## 5.5 Optical comb line properties

The first evaluation of the properties of the optical line of the ERGO frequency comb was done in a configuration where the comb was referenced to a hydrogen maser. The analysis was performed on the heterodyne beat signal between one line of the frequency comb, centered at  $1.56 \mu\text{m}$  and the cavity-stabilized ultra narrow linewidth laser (see Chapter 4). The beat signal was produced in a single mode 50-50 splitter/combiner (AFW Technologies, FOBC-2-15-50-C), by combining  $\sim 800 \mu\text{W}$  from the  $1557.5 \text{ nm}$  ultra-stable laser with  $\sim 200 \text{ nW}$  from the ERGO laser, spectrally filtered to a  $0.3 \text{ nm}$  width

by a diffraction grating. A fiber-coupled photodiode is then used for the detection of the beat note at  $\sim 29$  MHz, with a signal-to-noise ratio of more than 30 dB in 100 kHz resolution bandwidth. Afterwards, the signal was filtered, amplified and up-converted in order to be demodulated by the analog PLL frequency discriminator (Subsection 2.2.1). The demodulated base-band signal was recorded with the FFT spectrum analyzer.

The contribution of the phase noise of the ultra-stable laser to the noise of the detected beat signal is negligible. Therefore, the frequency noise of the beat signal corresponds directly to the frequency noise  $S_{\delta\nu}^{\text{opt}}(f)$  of the optical comb line (Figure 5.7).

The repetition rate is stabilized by applying feedback within the measured bandwidth of  $\sim 300$  Hz to the piezo-transducer (PZT) that carries the SESAM. The frequency noise of the repetition rate  $S_{\delta\nu}^{\text{rep}}(f)$  is measured by the SpectraDynamics Noise Measurement System Controller (NMSC-2), both for the fully stabilized and free-running ERGO frequency comb.

Compared to the hydrogen maser reference, some excess noise is present in the range from 2 Hz to 400 Hz in the repetition rate frequency noise PSD as well as in the optical line noise spectrum. The separate measurements of the noise of the reference dielectric resonator oscillator (DRO, locked to the hydrogen maser) and of the repetition rate, after being scaled to the frequency of the  $N$ -th comb line, reveal that the DRO is the source of this technical contribution to the noise of the optical line. Therefore, in this configuration, the stability of the optical line is limited by the RF reference and the noise of the optical line is dominated by the repetition rate noise, while the contribution of the CEO is negligible. Even in the kHz range, the servo bump of the CEO stabilization loop is not visible, which is usually the case in the fiber based systems [82].

The inset of the figure 5.7 is showing the linewidth of the optical line of the ERGO frequency comb stabilized fully to the RF reference. The FWHM linewidth is calculated by Equation 3.3 and is displayed in the function of the observation time. For the observation times

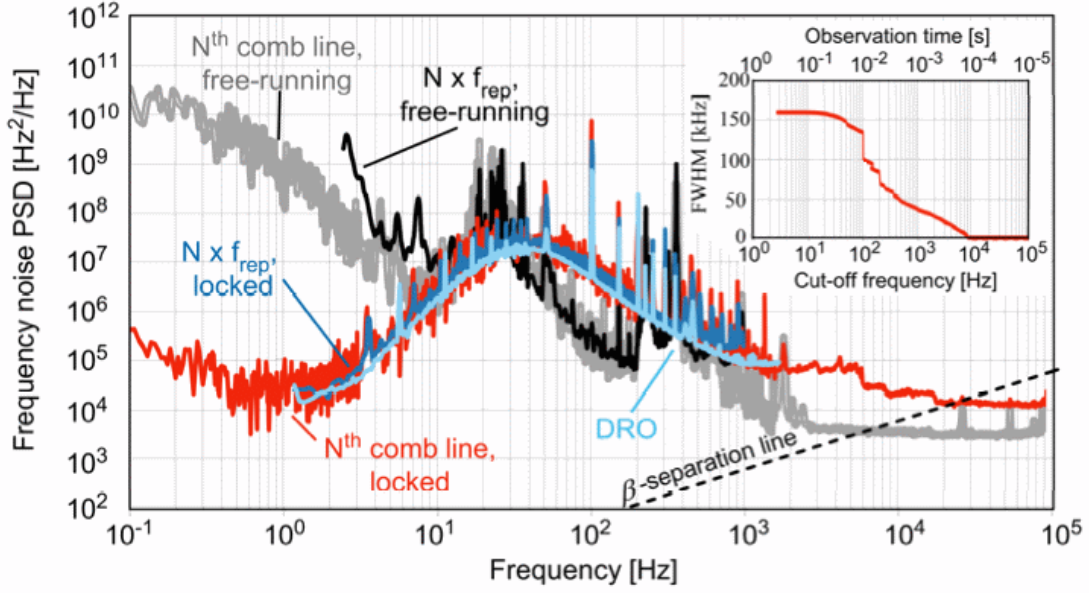


Figure 5.7: RF reference limiting the stability of the ERGO comb. The frequency noise of the comb line at 1557.5 nm with the index  $N \approx 2570000$  is accessed through the heterodyne beat with the narrow linewidth laser. Both free-running and stabilized mode of operation are displayed. For comparison, the frequency noise of the repetition rate multiplied by the line index  $N$  is also displayed ( $S_{\delta\nu}^{rep}(f)$  scaled by  $N^2$ ). Inset: FWHM linewidth of the optical line, calculated by Equation 3.3.

longer than 100 ms, the FWHM linewidth of  $\sim 160$  kHz is mainly the result of the presence of the excess noise in the repetition rate DRO reference.

## 5.6 CEO dynamics impact on stabilization

Many physical effects contribute to the change of the  $f_{\text{CEO}}$  with the pump power in a frequency comb, as it is exhaustively discussed in [97]. The response of the  $f_{\text{CEO}}$  to a change in the pump power thus is not simple and generally leads to a nonlinear behavior, which may affect the CEO stabilization. In a Ti:Sapphire comb, the existence



of a reversal point in the dependence of the  $f_{\text{CEO}}$  on the pump power has been shown in [98], with an important consequence for the CEO stabilization. This reversal point was accompanied by a significant change of the CEO frequency noise, revealing a strong reduction of the linewidth of the free-running CEO beat around this particular point. As a consequence, a much better stabilization of the CEO beat (i.e. achieving a lower residual phase noise) was obtained by tuning the pump power close to the reversal point, at which the contribution of pump power fluctuations to the CEO noise was minimized.

A reversal point in the variation of the  $f_{\text{CEO}}$  with the pump current in a 1.5  $\mu\text{m}$  DPSSL comb, has a different but crucial impact on the CEO stabilization. The dynamics of the  $f_{\text{CEO}}$ , that is, its frequency response to pump current modulation, depends on the position of the operating point relative to the reversal point and plays a major role in the ability to phase-stabilize  $f_{\text{CEO}}$ . More specifically, the dynamic response changes differently at low and high modulation frequencies on either side of the reversal point, indicating that different effects contribute to the tuning of the  $f_{\text{CEO}}$  with the pump current. The observed dynamic response, in particular in terms of its phase, fully explains the experimentally observed impossibility to stabilize the  $f_{\text{CEO}}$  when the pump current was tuned above the reversal point, whereas a tight phase-lock was straightforwardly achieved below the reversal point.

A pump diode current control, resulting in a linear variation of the pump power, is implemented as a standard method of the  $f_{\text{CEO}}$  fine-tuning and stabilization. By the direct influence on the pulse duration and energy, the pump current variations translate into a change of the CEO frequency. The static tuning of the  $f_{\text{CEO}}$  with the pump current is nonlinear and even non-monotonous in the ERGO comb, as illustrated in Figure 5.8.

A reversal point at which the slope of the dependence of the  $f_{\text{CEO}}$  on the pump current  $I_p$  changes its sign occurs at  $I_{\text{reversal}} \sim 860$  mA, corresponding to a pump power of  $\sim 563$  mW. In the ERGO comb, the CEO frequency is locked to a 20 MHz reference [9], which should

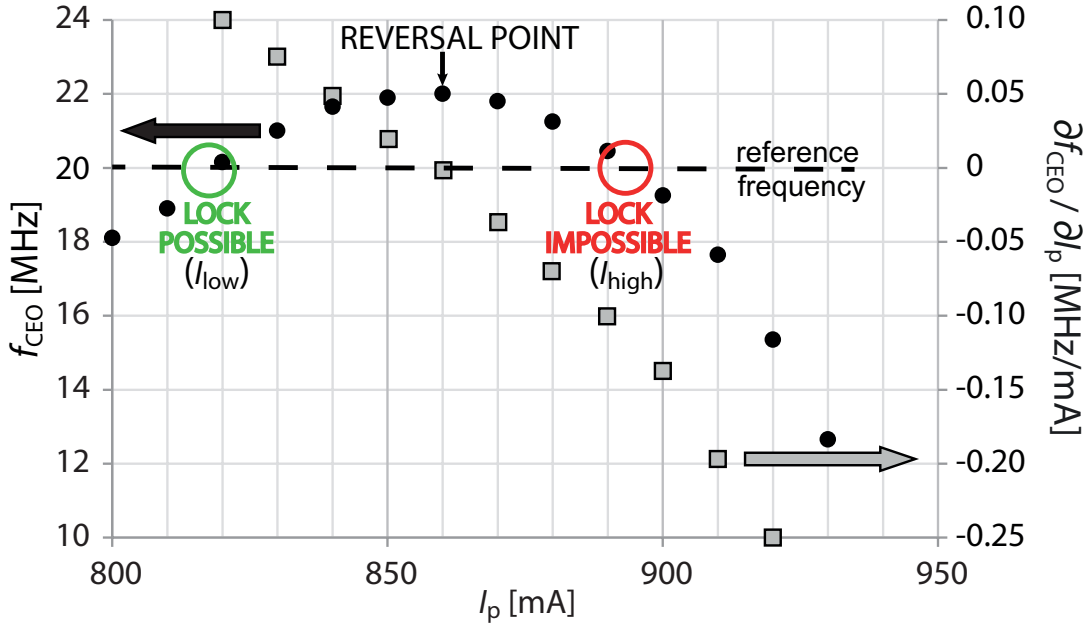


Figure 5.8: Static tuning curve of the CEO frequency  $f_{\text{CEO}}$  with respect to the pump current showing a reversal point at  $I_p \sim 860$  mA:  $f_{\text{CEO}}$  vs.  $I_p$  (left scale, black circles) and static tuning coefficient (right scale, grey squares).  $f_{\text{CEO}}$  is stabilized to 20 MHz in the ERGO comb, which can be realized in principle at two current values  $I_{\text{low}}$  and  $I_{\text{high}}$ .

be achievable in principle at the two different currents labeled  $I_{\text{low}} \sim 817$  mA and  $I_{\text{high}} \sim 893$  mA, respectively, for which  $f_{\text{CEO}} = 20$  MHz (Figure 5.8), provided that a correct sign is chosen for the feedback signal applied to the pump current. In practice, this is not the case and a strongly different behavior was observed on both sides of the reversal point. The lock is possible only at the operating current  $I_{\text{low}}$  located below the reversal point at which the CEO tuning coefficient  $\frac{\partial f_{\text{CEO}}}{\partial I_p}$  is positive. Despite the better signal-to-noise ratio of the CEO beat obtained at the higher current  $I_{\text{high}}$  located above the reversal point (40 dB observed at 100 kHz resolution bandwidth compared with 33 dB below the reversal point, as shown in the inset in Figure 5.9), no locking could be achieved at this point.

In contrast to the previous observations made in the Ti:Sapphire laser [98], there is no significant change in the frequency noise of the CEO beat, and thus on its free-running linewidth, when tuning the

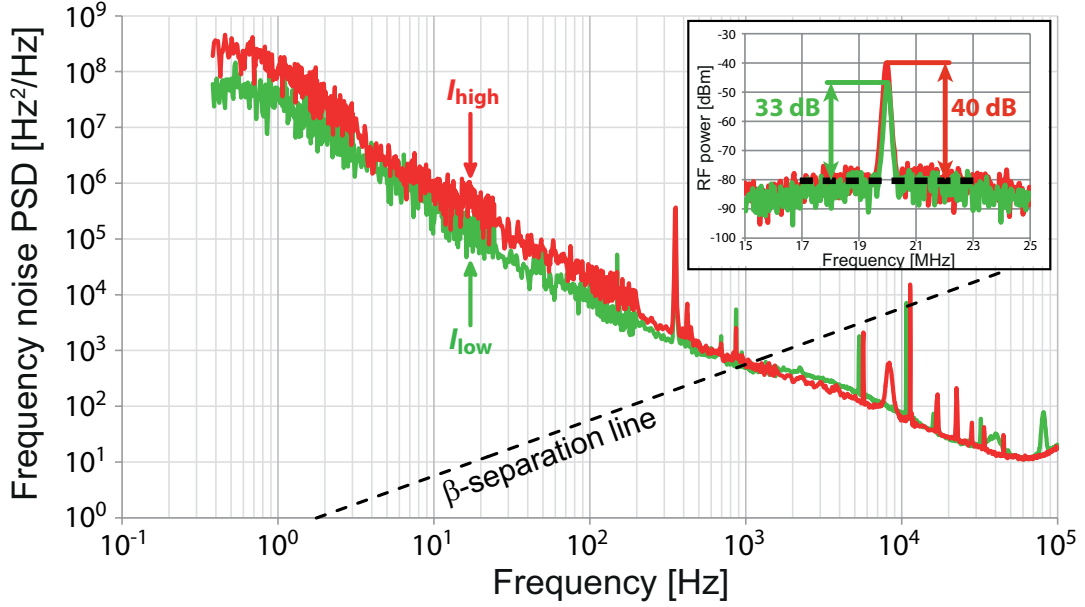


Figure 5.9: Frequency noise power spectral density (PSD) of the CEO beat measured at two different pump currents  $I_{\text{low}}$  and  $I_{\text{high}}$  at which  $f_{\text{CEO}} = 20\text{MHz}$ , located on each side of the reversal point. Only the noise that exceeds the  $\beta$ -separation line  $S_{\delta\nu}(f) = \frac{8 \ln 2}{\pi^2} f$  (dashed line) contributes to the linewidth of the CEO beat [7]. Inset: corresponding CEO beat showing a higher signal-to-noise ratio at  $I_{\text{high}}$  than at  $I_{\text{low}}$ .

pump current across the reversal point. Figure 5.9 shows a similar frequency noise PSD of the CEO beat at two operating currents  $I_{\text{low}}$  and  $I_{\text{high}}$ , measured using a frequency discriminator [5] and a fast Fourier transform analyzer. This indicates that the frequency noise of the CEO beat is not dominated by the fluctuations of the pump laser power in the ERGO comb and that some other effect is responsible for the inability to lock  $f_{\text{CEO}}$  at a high current value  $I_{\text{high}}$ .

To investigate this issue, the dynamic response of  $f_{\text{CEO}}$  was measured in amplitude and phase in a standard lock-in scheme, for a small pump current modulation depth (1 mA peak-to-peak), using a frequency discriminator (frequency-to-voltage converter) to demodulate the CEO beat. Figure 5.10 displays the transfer function of the  $f_{\text{CEO}}$  measured at different pump currents located on both sides of the reversal point. Figure 5.8 shows that the CEO static tuning

coefficient with the pump current is zero at the reversal point. Nevertheless, the yellow curve in Figure 5.10(a) does not strictly go to zero at the DC. The reason for this is the day to day manipulation within the laser cavity which can shift the exact position of the reversal point as well as the experimental error of setting the pump current exactly to the value that corresponds to the reversal point. One notices that the response at high frequencies (above  $\sim 1$  kHz) does not depend (both in amplitude and phase) on the operating pump current, whereas in the low-frequency range, a significant difference is observed, especially in the phase of the transfer function, which changes by  $180^\circ$  between low and high pump current. This behavior indicates that two different physical phenomena in the gain medium (with a nonlinear refractive index  $n_2 = 3.3 \times 10^{-16} \frac{\text{cm}^2}{\text{W}}$ ) are responsible for the tuning of the  $f_{\text{CEO}}$  with the pump current. Self-phase modulation (Kerr effect) very likely dominates the dependence of the  $f_{\text{CEO}}$  on the pump current at high modulation frequencies. This contribution is instantaneous and has no reason to be affected by a sign reversal with respect to the pump current. At low frequencies, however, a different, slower mechanism is responsible for the significant change of the transfer function observed at different pump currents, in particular in terms of phase. With a relatively tight focus in the gain medium (beam radius estimated by the simulation to  $20 \mu\text{m}$  in the tangential plane and  $13 \mu\text{m}$  in the sagittal plane [92]), thermal effect, such as thermal lensing in the gain medium, is believed to be responsible for this change.

Thermal lensing could change the overlap between the pump and the laser beams in the gain medium as a function of the pump current, and this change may lead to a shift of the CEO frequency in either direction. This thermal effect also constitutes the dominant contribution to the static tuning coefficient  $\frac{\partial f_{\text{CEO}}}{\partial I_p}$ . Its change of sign occurring at the reversal point (see Figure 5.8) is in good agreement with the  $180^\circ$  phase shift observed in the CEO transfer function at low modulation frequencies between the two cases  $I_p < I_{\text{reversal}}$  and  $I_p > I_{\text{reversal}}$ . This  $180^\circ$  phase shift is at the origin of the impossibility

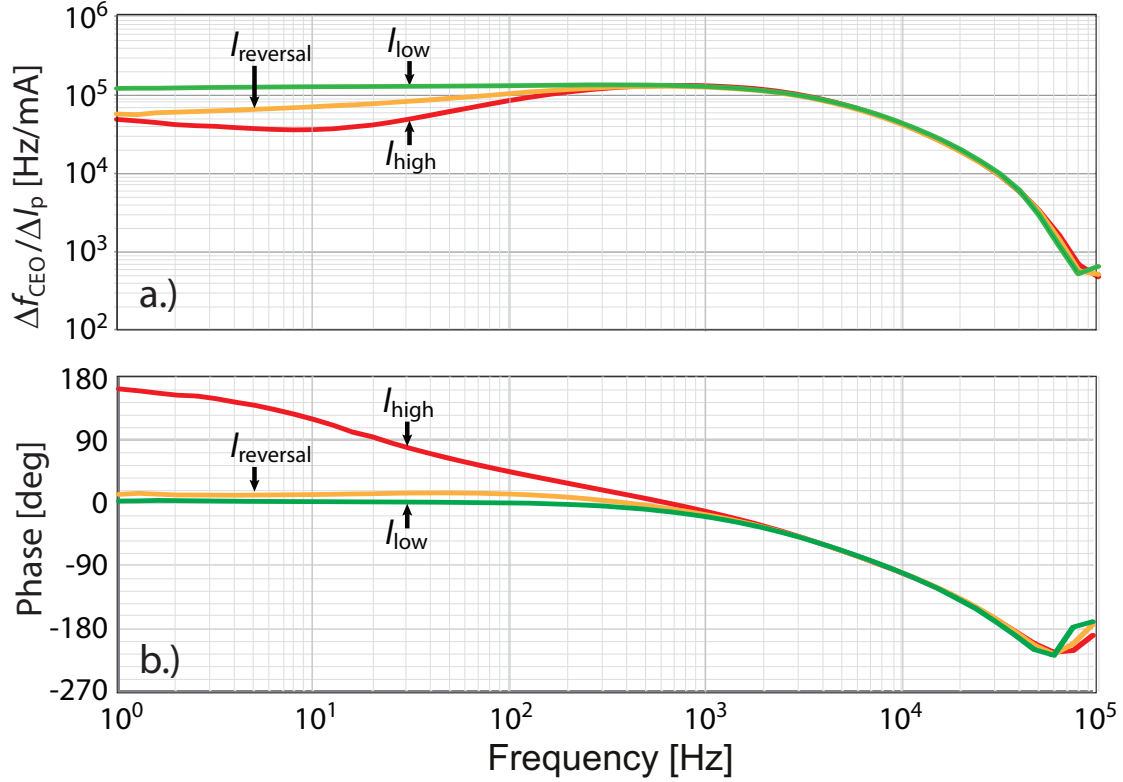


Figure 5.10: Amplitude (a) and phase (b) of the dynamic response of the  $f_{\text{CEO}}$  to pump current modulation measured at different pump currents:  $I_p = I_{\text{low}}$  below the reversal point (green curves),  $I_p = I_{\text{high}}$  above the reversal point (red curves) and  $I_p = I_{\text{reversal}}$  at the reversal point (orange curves).

to phase-stabilize  $f_{\text{CEO}}$  at the high pump current  $I_{\text{high}}$ , whereas the stabilization is straightforward at  $I_{\text{low}}$ , as will be discussed.

A general rule of thumb in control systems, requires a sufficient phase margin to be reached at the unity gain frequency, to keep a feedback loop stable [56]. As a consequence, the overall phase shift accumulated throughout the loop has to be kept sufficiently higher than  $-180^\circ$  to prevent the system from turning into a positive feedback loop, leading to an unstable operation. In the ERGO comb, the CEO beat stabilization loop involves a digital phase detector (MenloSystems DXD200) for the measurement of the phase fluctuations between the CEO beat and the 20 MHz reference frequency

and a servo controller (MenloSystems PIC201) to close the loop. The transfer function of these two components has been measured in amplitude and phase. Combined with the dynamic response of the  $f_{\text{CEO}}$  to the pump current modulation depicted in Figure 5.10, the transfer function of the entire stabilization loop has been determined, both in amplitude and phase, for the two pump currents of interest, as displayed in Figure 5.11.

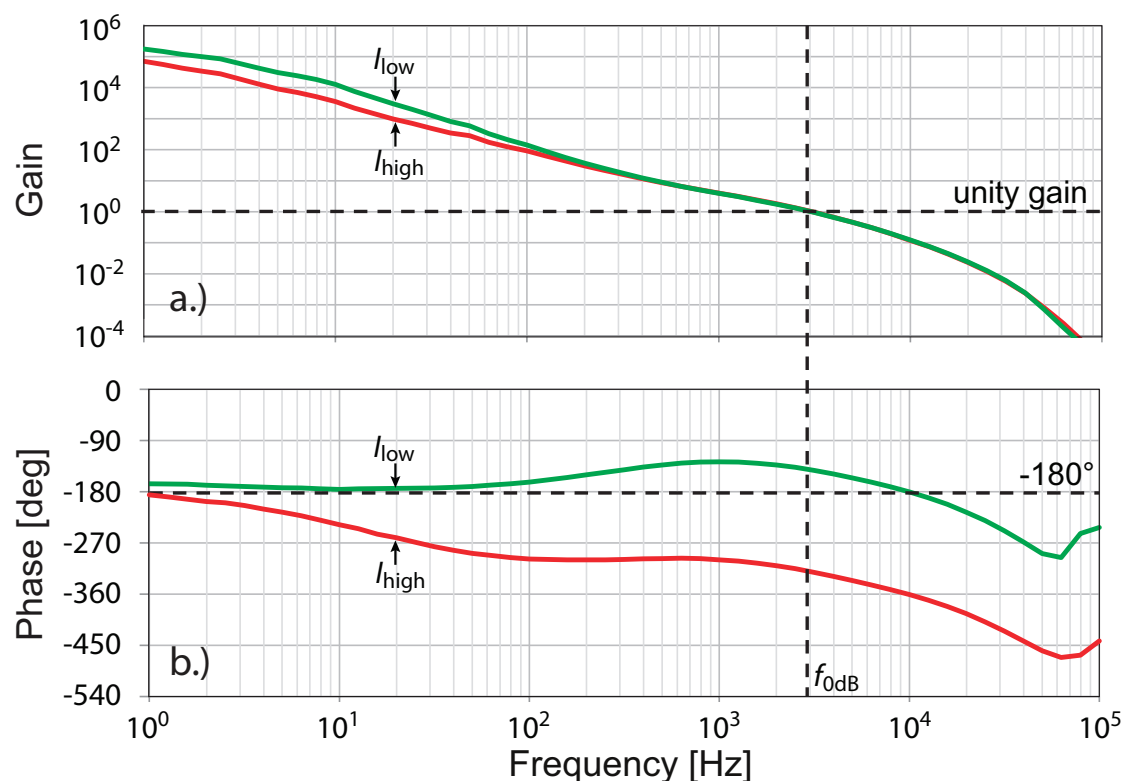


Figure 5.11: Gain (a) and phase (b) of the overall CEO stabilization loop transfer function at the two different pump currents  $I_p = I_{\text{low}}$  (top curves) and  $I_p = I_{\text{high}}$  (bottom curves). At  $I_p = I_{\text{low}}$ , the phase margin is sufficient to achieve a feedback bandwidth (labeled as  $f_{\text{0dB}}$ ) of several kHz. At  $I_p = I_{\text{high}}$ , the phase is  $< -180^\circ$  already at 1 Hz Fourier frequency, which prevents the CEO stabilization.

The contribution from the dynamic response of the CEO beat to the pump current modulation does not exhibit a significant phase shift up to  $\sim 1$  kHz at pump currents below the reversal point (Fig-

ure 5.10), so that a feedback bandwidth of several kilohertz can be achieved with a sufficient phase margin, resulting in a tight phase lock of the CEO beat. On the other side of the reversal point, a large phase shift in the CEO beat dynamic response is already reached at a very low frequency, which leads to an overall loop phase shift lower than  $-180^\circ$  already at 1 Hz Fourier frequency. This explains the impossibility to stabilize the CEO beat at an operating current above the reversal point.

## 5.7 Conclusion

In this chapter I have described the full stabilization of the ERGO (Er:Yb:glass) DPSSL based frequency comb in the  $1.5 \mu\text{m}$  spectral region and its noise properties. The strong advantage of the high Q cavity operation is reflected in the low-noise CEO beat signal of the record low free-running FWHM linewidth (below 4 kHz) in this spectral region. As a direct consequence it is possible to stabilize the CEO beat to an external 20 MHz reference with a feedback loop of only 5.5 kHz in bandwidth. The residual CEO integrated phase noise of 0.72 rad-rms is one of the smallest in this spectral region obtained with the servo loop of such a small bandwidth. This bandwidth is limited with the Er dynamics and further improvements would not make this comb comparable with the e.g. Ti:sapphire based systems, having the residual phase noise of the CEO beat below 0.1 rad-rms. In such a system the upper state lifetime of the Ti is much lower resulting therefore in the higher stabilization bandwidth.

The Allan deviation of the 20 MHz CEO beat frequency at the level of  $10^{-8} \times \tau^{-1}$  is 20-fold improvement in comparison with the commercial Er:fiber frequency comb. The comparison is done with both system operating in the optimal conditions, i.e. with the utilization of the full feedback bandwidth of each system. The low-noise properties of the CEO beat are qualifying this comb technology for the ultra-stable microwave generation [13]. The high stability of the optical reference i.e. cavity-stabilized CW laser is directly transferred

to the microwave signal within the simplest possible locking scheme, by locking one of the teeth of the comb to the optical reference. The contribution of the CEO to the stability of the generated microwave is expected to be at the level of  $10^{-15}$  at 1 s, decreasing with the integration time as  $\tau^{-1}$ .

The properties of the optical comb line have been analyzed from the heterodyne beat with the cavity-stabilized laser. The limitations coming from the reference DRO have been demonstrated. The linewidth of the comb line of  $\approx 160$  kHz is calculated from the frequency noise spectrum. Some improvements could be expected with the fine tuning or upgrade of the stabilization electronics, specially from the elimination of the spurious noise peaks at 50 Hz and its harmonics. Nevertheless, the main improvement in the operation is expected from the stabilization of the comb to the optical reference.

The importance of the CEO dynamics in the self-referencing of a DPSSL frequency comb has been demonstrated. The existence of a significant phase shift of  $\sim 180^\circ$  in the dynamic response of the  $f_{\text{CEO}}$  for pump current modulation between the low (a few hertz) and the high (kilohertz) frequency ranges prevents the CEO beat to be phase-stabilized at pump currents above the reversal point. On the contrary, the flat CEO phase response obtained at pump currents below the reversal point enables an overall feedback bandwidth of several kilohertz, which straightforwardly results in a tight CEO lock. This result demonstrates that a high signal-to-noise ratio and a low-noise CEO beat are the prerequisites for the self-referencing of an optical frequency comb, but these conditions may not be sufficient in cases for which the CEO dynamics plays a crucial role. Although this observation was made for a particular DPSSL comb, similar effects might also occur in the other types of combs and have to be considered when a new type of ultrafast laser is aimed at being self-referenced.





## Chapter 6

# Conclusion and outlook

In this work, I presented one part of our group's and my own activities in the domain of the optical frequency metrology.

We developed an analog phase-locked loop (PLL) based, radio frequency (RF) discriminator technique for the noise analysis of the narrow linewidth optical beat signals. Terahertz oscillations are down-converted to the radio frequency domain by beating of the two optical signals. It is then possible to use the frequency discriminator technique for the demodulation of the RF signal and therefore enable access to the noise that originates at the optical frequencies. A set of the commercial frequency (phase) discriminators (Miteq RF discriminator, MenloSystems DXD200 digital phase detector and Zurich Instruments HF2PLL digital phase-locked loop) has been characterized in detail and the comparison with the home-made analog PLL was made. With its large linear range (7 MHz), bandwidth of 200 kHz and frequency noise floor below  $10^{-2} \frac{\text{Hz}^2}{\text{Hz}}$  between 10 Hz and 100 kHz, the analog PLL frequency discriminator enables the characterization of the beat signals whose linewidths lie between few megahertz and few hertz. Therefore, it enables the measurement of the frequency noise of the free-running lasers, as well as the cavity stabilized ultra-stable lasers. It can also be used for the determination of the response bandwidth of the repetition rate and the carrier-envelope offset (CEO) in both the free-running and sta-

bilized frequency combs. The Miteq RF discriminator, although the simplest to implement, has a strong sensitivity to the amplitude modulation and the amplitude noise. Its amplitude noise induced high noise floor hides the greatest portion of the residual frequency noise of the stabilized CEO signals, but it is still useful for the analysis of the free-running signals. The HF2PLL digital phase-locked loop, being low-noise and quite flexible, in terms of characterization of the frequency noise spectrum suffers from the limited bandwidth. Additionally, at lower Fourier frequencies (below 100 Hz) and for lower discriminator factors (necessary in order to avoid the saturation of the output) the noise floor is preventing the detection of the small frequency fluctuations. The DXD200 digital phase detector is very sensitive to small frequency fluctuations at low Fourier frequencies. It is therefore the most sensitive device for the analysis of the beat signals that contain both frequency and amplitude noise, as is the case e.g. in the stabilized CEO beat of the Er:Yb:glass (ERGO) frequency comb.

Di Domenico et al. [6] made a theoretical analysis of the relation between the linewidth of the laser and its frequency noise power spectral density (PSD). They have recognized a  $\beta$ -separation line ( $S_{\delta\nu}(f) = \frac{8\ln 2}{\pi^2}f$ ) in the frequency noise PSD, that makes a distinction between the noise components contributing to the linewidth and to the wings of the lineshape. Based on this observation, they proposed a simple geometrical approximation ( $\Delta f_{FWHM} = \sqrt{(8\ln 2)A}$ ) which enables the calculation of the laser linewidth from the surface  $A$  in the frequency noise power spectral density graph. The surface  $A$  is calculated by taking into account only those noise components that are above the  $\beta$ -separation line ( $S_{\delta\nu}(f) > \frac{8\ln 2}{\pi^2}f$ ) i.e. the components which are responsible for the slow carrier modulation. This approximation was experimentally validated on a set of the optical heterodyne beat signals, produced by the state-of-the-art laser sources, namely a solid state and a fiber-based frequency combs and the cavity stabilized narrow-linewidth laser. The frequency discriminator technique was applied for the measurement of the frequency

noise of the signals with the different spectral properties. At the same time, the signal under test was recorded with the spectrum analyzer and its linewidth was determined by fitting the data. These directly measured values are then compared with the values calculated from the frequency noise power spectrum. We demonstrated an excellent agreement between the approximate and the directly measured linewidth. Furthermore, we confirmed that the above mentioned approximation is valid over a broad range of values, spanning three decades (from  $10^3$  Hz to  $10^6$  Hz), as well as for a wide variety of the line shape functions, expressed through different contributions of the Lorentzian and Gaussian linewidth to the Voigt linewidth. This approximation avoids the two-step numerical integration procedure, encountered in the exact determination of the laser line shape from the frequency noise PSD [33] and it thus represents a practical and reliable tool.

The ultra-narrow, cavity stabilized lasers are essential for the development and the operation of the optical frequency standards. Recently we have built the second ultra-stable Perot-Fabry passive reference cavity (LTF-ULE2). The 10 cm long, notched and vibration insensitive, horizontal cavity spacer [63] is made out of the ultra-low expansion (ULE) glass. The high reflectivity cavity mirrors (for  $\lambda = 1557$  nm) are deposited on the fused silica (FS) substrates and are optically contacted with the ULE spacer. Additional ULE rings are optically contacted on the back side of the FS mirrors in order to compensate for the difference in the thermal expansion coefficient of the spacer and the mirror substrates. In this manner it is possible to tune the coefficient of thermal expansion of the cavity [64] and to bring the zero crossing of the cavity's CTE into the room temperature region. The cavity is placed in the two-layer thermal shield (inner Cu cradle within the gold coated Al thermal screen) and the whole assembly is isolated in the vacuum chamber at the residual pressure of  $2 \times 10^{-7}$  mbar. The vacuum chamber and the optical setup that is used to couple the light into the cavity, are mechanically stabilized by the active anti-vibration system. The mechanical layout is opti-

mized for the transportability that might be needed in the future. A homemade temperature controller is used to monitor, manipulate and stabilize the temperature of the thermal screen. A thermal model of the system under vacuum has been developed and it was used to improve the thermal control, which enabled a temperature step for the LTF-ULE2 cavity to be made within 2.5 days. This represents more than 10-fold speed-up in comparison with the LTF-ULE1 system [42] where the advanced temperature control has not been implemented. The low-noise planar waveguide extended cavity laser (PW-ECL) from Redfern Integrated Optics Inc. is stabilized to the LTF-ULE2 cavity in the Pound-Drever-Hall stabilization scheme. The slow corrections are applied through the laser current module and the fast to the acousto-optic modulator (AOM), resulting with the bandwidth of the stabilization loop of  $\sim 170$  kHz. By changing the cavity temperature in 1 K steps, with the laser frequency counted at each, discrete temperature set point, the temperature of the zero expansion coefficient is determined to be at  $T_0^{CTE} = (20.51 \pm 0.06)^\circ\text{C}$ . The cavity resonance FWHM linewidth of 2.4 kHz is determined from the ring-down time of  $\approx 66 \mu\text{s}$ , which, for the free spectral range of 1.5 GHz corresponds to the finesse of  $\approx 620000$  i.e. to the resonator Q factor of  $8 \times 10^{10}$ . When the cavity temperature was stabilized at the  $T_0^{CTE}$ , the frequency of the stabilized laser was monitored in stages during 400 thousand seconds, and the resonance frequency drift of  $\approx 31 \frac{\text{mHz}}{\text{s}}$  was measured.

On our path towards the fully optical generation of the ultra-stable microwave signals, the last element is an optical frequency comb, which can coherently divide the optical reference frequency of the cavity stabilized laser, down to the microwave domain. We examined the noise properties of a novel type of the ultra-fast Er:Yb:glass oscillator (ERGO), a  $1.5 \mu\text{m}$  diode-pumped solid-state laser (DPSSL) passively mode-locked by the semiconductor saturable absorber mirror (SESAM). In this technology, the high Q and low-noise operation of the solid-state lasers is combined with laser diode pumping, that is more often seen as the approach in the fiber lasers. The main

advantage of this kind of the laser configuration is the record narrow linewidth free-running carrier-envelope offset (CEO) beat in this spectral region of only 3.6 kHz [99]. The stabilization of such a narrow CEO to an external 20 MHz reference is achieved with the loop bandwidth of only 5.5 kHz, limited by the dynamics of the erbium atoms. This stabilization results with the residual integrated phase noise of 0.72 rad-rms, being one of the smallest values achieved in 1.5  $\mu\text{m}$  spectral region with such a low feedback bandwidth. Compared to a commercial Er:fiber frequency comb, we see a 20-fold improvement in the Allan deviation of the 20 MHz CEO beat. The value of the Allan deviation of  $10^{-8} \times \tau^{-1}$  qualifies this frequency comb for the ultra-stable microwave generation with the stability at the level of  $10^{-15}$  at 1 s. The linewidth of the optical comb line is limited by the reference dielectric resonator oscillator (DRO). The value of  $\sim 160$  kHz is calculated from the frequency noise spectrum, measured by the frequency discriminator technique, from the heterodyne beat with the cavity stabilized laser. We also examined the influence of the CEO dynamics on the stabilization of the ERGO frequency comb. The frequency of the CEO is changing with the pump laser current and has a maximum at certain, reversal point. A significant phase shift of  $\sim 180^\circ$  in the response of the  $f_{\text{CEO}}$  to the pump laser current modulation is identified as the reason for the inability to achieve the stabilization of the CEO at pump currents above the reversal point. Therefore, we have seen that sometimes the dynamics of the CEO plays a crucial role in the self-referencing of the optical frequency comb and that a high signal-to-noise ratio and a low-noise CEO are not the only conditions that have to be fulfilled.

Although it is out of the scope of this thesis, all of the elements for the all-optical ultra-stable microwave oscillator have been developed and characterized. The development of the high stability and high spectral purity microwave source for the characterization of the continuous cold cesium atom fountain clock (FOCS-2) [11] is the main goal of our activities. This atomic fountain is placed in the Swiss

Federal Institute of Metrology (METAS, Bern). Therefore, the second ultra-stable cavity enclosure was constructed to be transportable and in the future, together with the ERGO comb it might be moved to METAS. When one line of the ERGO frequency comb is phase-locked to the cavity-stabilized laser, the stability of the ultra-narrow laser is transferred from the optical to microwave domain. Recently, the microwave signal at  $\sim 10$  GHz was extracted and characterized by the use of the transportable cryogenic sapphire, ultra-low instability signal source (ULISS) from Femto-ST in Besançon, France. The Allan deviation of  $\sim 6 \times 10^{-15}$  at 1 s has been measured, as well as roughly 20 dB improvement in the phase noise, compared to the signal generated in the same scheme from the Er:fiber frequency comb [12, 13]. In the near future, the second laser should be stabilized to either of the ULE cavities and with the observation of the beat signal between the two, the operation of both systems could be optimized. E.g. the source of the low frequency perturbations (a few hertz) still has not been identified and removed. The stabilization setup should be made more robust and in that sense, an acoustic isolation should be considered. Finally, with all of the technical parameters optimized, the beat between the two ultra-stable lasers with the linewidth in the range from one to a few hertz is expected. With the two frequency combs in the laboratory (75 MHz ERGO DPSSL and 250 MHz MenloSystems Er:fiber) as well as the two ultra-stable lasers, the opportunity for the all-in-house microwave generation and characterization will be open.

Very interesting illustration of the potential application of the combination ultra-stable laser  $\leftrightarrow$  optical frequency comb, as the source of the low-noise microwave signal is displayed in Figure 6.1. The image shows the radio signal of the Voyager 1 spacecraft, captured when the probe was about to leave the Solar system and enter the inter-stellar space, 18.5 billion kilometers away from the Earth. The signal was recorded by the Very Large Baseline Array (VLBA) of radio telescopes, spanning the distance of 8000 kilometers. This measurement technique is fundamentally dependent on the quality of the

local oscillators which enable the correlation of the signals captured at continental distances. Hydrogen masers are currently used but in the future, when the optically generated microwave signal sources reach commercially acceptable stage, this field could profit from the low noise and high stability, coming from the optical domain.

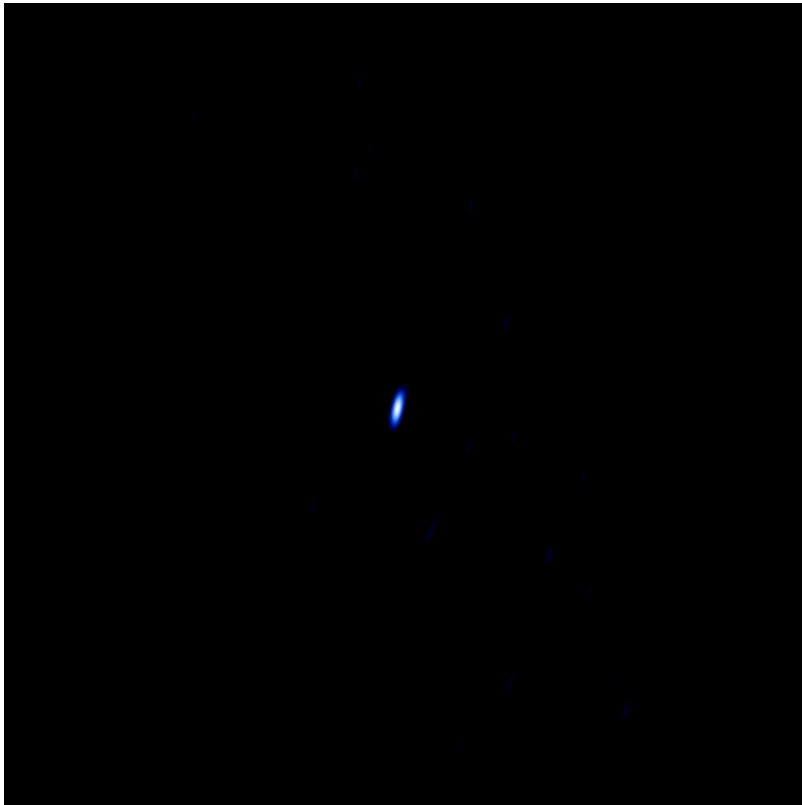


Figure 6.1: Radio signal of the Voyager 1 probe, 18.5 billion kilometers away from the Earth, reconstructed from the VLBA radio telescope array. The image is the courtesy of NRAO/AUI/NSF.





# Bibliography

- [1] R. F. C. Vessot, “Test of relativistic gravitation with a spaceborne hydrogen maser,” *Physical Review Letters*, vol. 45, pp. 2081–2084, 1980.
- [2] J. C. Hafele and R. E. Keating, “Around-the-world atomic clocks: observed relativistic time gains,” *Science*, vol. 177, pp. 168–170, 1972.
- [3] R. Le Targat, L. Lorini, Y. Le Coq, M. Zawada, J. Guéna, M. Abgrall, M. Gurov, P. Rosenbusch, D. G. Rovera, B. Nagorny, R. Gartman, P. G. Westergaard, M. E. Tobar, M. Lours, G. Santarelli, A. Clairon, S. Bize, P. Laurent, P. Lemonde, and J. Lodewyck, “Experimental realization of an optical second with strontium lattice clocks,” *Nature Communications*, vol. 4, July 2013.
- [4] N. K. Pavlis and M. A. Weiss, “The relativistic gravitational redshift with  $3 \times 10^{-17}$  uncertainty at NIST, Boulder, Colorado,” *Metrologia*, vol. 40, pp. 66–73, 2003.
- [5] S. Schilt, N. Bucalovic, L. Tombez, V. Dolgovskiy, C. Schori, G. Di Domenico, M. Zaffalon, and P. Thomann, “Frequency discriminators for the characterization of narrow-spectrum heterodyne beat signals: application to the measurement of a sub-hertz carrier-envelope-offset beat in an optical frequency comb,” *Review of Scientific Instruments*, vol. 82, no. 12, p. 123116–123116, 2011.

- [6] G. Di Domenico, S. Schilt, and P. Thomann, “Simple approach to the relation between laser frequency noise and laser line shape,” *Applied Optics*, vol. 49, no. 25, p. 4801–4807, 2010.
- [7] N. Bucalovic, V. Dolgovskiy, C. Schori, P. Thomann, G. Di Domenico, and S. Schilt, “Experimental validation of a simple approximation to determine the linewidth of a laser from its frequency noise spectrum,” *Applied Optics*, vol. 51, no. 20, p. 4582–4588, 2012.
- [8] M. Stumpf, S. Pekarek, A. Oehler, T. Südmeyer, J. Dudley, and U. Keller, “Self-referencable frequency comb from a 170-fs, 1.5- $\mu\text{m}$  solid-state laser oscillator,” *Applied Physics B*, vol. 99, no. 3, pp. 401–408, 2010.
- [9] S. Schilt, N. Bucalovic, V. Dolgovskiy, C. Schori, M. C. Stumpf, G. D. Domenico, S. Pekarek, A. E. H. Oehler, T. Südmeyer, U. Keller, and P. Thomann, “Fully stabilized optical frequency comb with sub-radian CEO phase noise from a SESAM-modelocked 1.5- $\mu\text{m}$  solid-state laser,” *Optics Express*, vol. 19, p. 24171–24181, Nov. 2011.
- [10] N. Bucalovic, V. Dolgovskiy, M. C. Stumpf, C. Schori, G. Di Domenico, U. Keller, S. Schilt, and T. Südmeyer, “Effect of the carrier-envelope-offset dynamics on the stabilization of a diode-pumped solid-state frequency comb,” *Optics Letters*, vol. 37, pp. 4428–4430, Nov. 2012.
- [11] G. Di Domenico, L. Devenoges, A. Joyet, A. Stefanov, and P. Thomann, “Uncertainty evaluation of the continuous cesium fountain frequency standard FOCS-2,” in *Frequency Control and the European Frequency and Time Forum (FCS), 2011 Joint Conference of the IEEE International*, pp. 1–5, 2011.
- [12] V. Giordano, S. Grop, B. Dubois, P.-Y. Bourgeois, Y. Kersale, G. Haye, V. Dolgovskiy, N. Bucalovic, G. D. Domenico, S. Schilt, J. Chauvin, D. Valat, and E. Rubiola, “New-generation of

- cryogenic sapphire microwave oscillators for space, metrology, and scientific applications,” *Review of Scientific Instruments*, vol. 83, no. 8, p. 085113, 2012.
- [13] V. Dolgovskiy, S. Schilt, N. Bucalovic, G. Domenico, S. Grop, B. Dubois, V. Giordano, and T. Südmeyer, “Ultra-stable microwave generation with a diode-pumped solid-state laser in the 1.5- $\mu\text{m}$  range,” *Applied Physics B*, pp. 1–9, DOI: 10.1007/s00340-013-5740-7, 2013.
- [14] L. Hollberg, S. Diddams, A. Bartels, T. Fortier, and K. Kim, “The measurement of optical frequencies,” *Metrologia*, vol. 42, pp. S105–S124, June 2005.
- [15] J. Alnis, A. Matveev, N. Kolachevsky, T. Udem, and T. W. Hänsch, “Subhertz linewidth diode lasers by stabilization to vibrationally and thermally compensated ultralow-expansion glass Fabry-Perot cavities,” *Physical Review A*, vol. 77, May 2008.
- [16] B. C. Young, F. C. Cruz, W. M. Itano, and J. C. Bergquist, “Visible lasers with subhertz linewidths,” *Physical Review Letters*, vol. 82, no. 19, p. 3799, 1999.
- [17] C. E. Wieman and L. Hollberg, “Using diode lasers for atomic physics,” *Review of Scientific Instruments*, vol. 62, pp. 1–20, Jan. 1991.
- [18] T. Okoshi, K. Kikuchi, and A. Nakayama, “Novel method for high resolution measurement of laser output spectrum,” *Electronics Letters*, vol. 16, no. 16, pp. 630–631, 1980.
- [19] L. D. Turner, K. P. Weber, C. J. Hawthorn, and R. E. Scholten, “Frequency noise characterisation of narrow linewidth diode lasers,” *Optics Communications*, vol. 201, no. 4, p. 391–397, 2002.
- [20] S. Bartalini, S. Borri, P. Cancio, A. Castrillo, I. Galli, G. Giusfredi, D. Mazzotti, L. Gianfrani, and P. De Natale, “Observing

- the intrinsic linewidth of a quantum-cascade laser: Beyond the Schawlow-Townes limit,” *Physical Review Letters*, vol. 104, Feb. 2010.
- [21] S. T. Cundiff and J. Ye, “Colloquium: Femtosecond optical frequency combs,” *Reviews of Modern Physics*, vol. 75, no. 1, p. 325, 2003.
- [22] L. Tombez, J. D. Francesco, S. Schilt, G. D. Domenico, J. Faist, P. Thomann, and D. Hofstetter, “Frequency noise of free-running 4.6  $\mu\text{m}$  distributed feedback quantum cascade lasers near room temperature,” *Optics Letters*, vol. 36, p. 3109–3111, Aug. 2011.
- [23] G. Galzerano, A. Gambetta, E. Fasci, A. Castrillo, M. Marangoni, P. Laporta, and L. Gianfrani, “Absolute frequency measurement of a water-stabilized diode laser at 1.384  $\mu\text{m}$  by means of a fiber frequency comb,” *Applied Physics B*, vol. 102, no. 4, pp. 725–729, 2011.
- [24] J. Tournenc, *Caractérisation et Modélisation du Bruit d’Amplitude Optique, du Bruit de Fréquence et de la Largeur de Raie de VCSEs monomodes émettant autour de 850nm*. PhD thesis, Université de Montpellier II, 2005.
- [25] D. Baney and W. Sorin, “High resolution optical frequency analysis,” in *Fiber Optic Test and Measurement* (D. Derickson, ed.), pp. 169–219, New Jersey: Prentice Hall, 1998.
- [26] M. Prevedelli, T. Freegrade, and T. W. Hänsch, “Phase locking of grating-tuned diode lasers,” *Applied Physics B*, vol. 60, p. S241–S248, 1995.
- [27] F. Riehle, “Characterisation of amplitude and frequency noise,” in *Frequency Standards*, p. 47–79, Wiley-VCH Verlag GmbH & Co. KGaA, 2005.

- [28] E. Rubiola, “The Leeson effect - phase noise in quasilinear oscillators,” in *Phase Noise and Frequency Stability in Oscillators*, Cambridge University Press, 2008.
- [29] M. Stumpf, S. Pekarek, A. Oehler, T. Südmeyer, J. Dudley, S. Schilt, G. Di Domenico, P. Thomann, and U. Keller, “First fully stabilized frequency comb from a SESAM-modelocked 1.5- $\mu\text{m}$  solid-state oscillator,” in *EFTF-2010 24th European Frequency and Time Forum*, pp. 1–4, 2010.
- [30] H. R. Telle, G. Steinmeyer, A. E. Dunlop, J. Stenger, D. H. Sutter, and U. Keller, “Carrier-envelope offset phase control: A novel concept for absolute optical frequency measurement and ultrashort pulse generation,” *Applied Physics B*, vol. 69, no. 4, p. 327–332, 1999.
- [31] S. Schilt, V. Dolgovskiy, N. Bucalovic, L. Tombez, M. Stumpf, G. Di Domenico, C. Schori, S. Pekarek, A. Oehler, T. Südmeyer, U. Keller, and P. Thomann, “Optical frequency comb with sub-radian CEO phase noise from a SESAM-modelocked 1.5  $\mu\text{m}$  solid-state laser,” in *CLEO 2011, talk CFK3*, (Baltimore, USA), May 2011.
- [32] S. Spießberger, M. Schiemangk, A. Wicht, H. Wenzel, G. Erbert, and G. Tränkle, “DBR laser diodes emitting near 1064 nm with a narrow intrinsic linewidth of 2 kHz,” *Applied Physics B*, vol. 104, no. 4, pp. 813–818, 2011.
- [33] D. S. Elliott, R. Roy, and S. J. Smith, “Extracavity laser bandshape and bandwidth modification,” *Physical Review A*, vol. 26, p. 12–18, July 1982.
- [34] P. Gallion and G. Debarge, “Quantum phase noise and field correlation in single frequency semiconductor laser systems,” *Quantum Electronics, IEEE Journal of*, vol. 20, no. 4, pp. 343–349, 1984.

- [35] G. Stéphan, T. Tam, S. Blin, P. Besnard, and M. Têtu, “Laser line shape and spectral density of frequency noise,” *Physical Review A*, vol. 71, Apr. 2005.
- [36] L. B. Mercer, “1/f frequency noise effects on self-heterodyne linewidth measurements,” *Lightwave Technology, Journal of*, vol. 9, no. 4, pp. 485–493, 1991.
- [37] A. L. Schawlow and C. H. Townes, “Infrared and optical masers,” *Physical Review*, vol. 112, p. 1940–1949, Dec. 1958.
- [38] C. Henry, “Theory of the linewidth of semiconductor lasers,” *Quantum Electronics, IEEE Journal of*, vol. 18, no. 2, p. 259–264, 1982.
- [39] T. Hänsch, “Nobel lecture: Passion for precision,” *Reviews of Modern Physics*, vol. 78, pp. 1297–1309, Nov. 2006.
- [40] E. Benkler, H. Telle, A. Zach, and F. Tauser, “Circumvention of noise contributions in fiber laser based frequency combs,” *Optics Express*, vol. 13, p. 5662–5668, July 2005.
- [41] V. Dolgovskiy, N. Bucalovic, P. Thomann, C. Schori, G. Di Domenico, and S. Schilt, “Cross-influence between the two servo loops of a fully stabilized Er:fiber optical frequency comb,” *JOSA B*, vol. 29, no. 10, p. 2944–2957, 2012.
- [42] V. Dolgovskiy, S. Schilt, G. Di Domenico, N. Bucalovic, C. Schori, and P. Thomann, “1.5- $\mu\text{m}$  cavity-stabilized laser for ultra-stable microwave generation,” in *Joint IFCS/EFTF 2011, poster #228*, (San Francisco, USA), May 2011.
- [43] J. J. Olivero and R. L. Longbothum, “Empirical fits to the Voigt line width: A brief review,” *Journal of Quantitative Spectroscopy and Radiative Transfer*, vol. 17, no. 2, pp. 233 – 236, 1977.

- [44] P. Gill, “Optical frequency standards,” *Metrologia*, vol. 42, pp. S125–S137, June 2005.
- [45] A. Quessada, R. P. Kovacich, I. Courtillot, A. Clairon, G. Santarelli, and P. Lemonde, “The Dick effect for an optical frequency standard,” *Journal of Optics B: Quantum and Semiclassical Optics*, vol. 5, no. 2, p. S150, 2003.
- [46] F. Füzési, M. Plimmer, G. Dudley, J. Guéna, and P. Thomann, “Design details of FOCS-2, an improved continuous cesium fountain frequency standard,” in *Frequency Control Symposium, 2007 Joint with the 21st European Frequency and Time Forum. IEEE International*, pp. 90–95, 2007.
- [47] J. Millo, *Génération de signaux micro-ondes pour la métrologie à partir de références et peignes de fréquences optiques*. PhD thesis, Pierre et Marie Curie - Paris VI, Paris, France, 2010.
- [48] E. Black, “Notes on the Pound-Drever-Hall technique,” Internal working note of the LIGO Project LIGO-T980045-00-D, Caltech, MIT, 1998.
- [49] R. V. Pound, “Electronic frequency stabilization of microwave oscillators,” *Review of Scientific Instruments*, vol. 17, no. 11, p. 490, 1946.
- [50] M. J. Martin and J. Ye, “High-precision laser stabilization via optical cavities,” in *Optical Coatings and Thermal Noise in Precision Measurement*, pp. 237–258, Cambridge University Press, cambridge books online ed., 2012.
- [51] O. Mor and A. Arie, “Performance analysis of Drever-Hall laser frequency stabilization using a proportional+integral servo,” *Quantum Electronics, IEEE Journal of*, vol. 33, no. 4, p. 532–540, 1997.



- [52] E. D. Black, “An introduction to Pound–Drever–Hall laser frequency stabilization,” *American Journal of Physics*, vol. 69, no. 1, p. 79, 2001.
- [53] T. Day, E. Gustafson, and R. Byer, “Sub-hertz relative frequency stabilization of two-diode laser-pumped Nd:YAG lasers locked to a Fabry-Perot interferometer,” *Quantum Electronics, IEEE Journal of*, vol. 28, no. 4, pp. 1106–1117, 1992.
- [54] R. W. P. Drever, J. L. Hall, F. V. Kowalski, J. Hough, G. M. Ford, A. J. Munley, and H. Ward, “Laser phase and frequency stabilization using an optical resonator,” *Applied Physics B*, vol. 31, no. 2, p. 97–105, 1983.
- [55] C. Salomon, D. Hils, and J. L. Hall, “Laser stabilization at the millihertz level,” *J. Opt. Soc. Am. B*, vol. 5, p. 1576–1587, Aug. 1988.
- [56] R. W. Fox, C. W. Oates, and L. W. Hollberg, “Stabilizing diode lasers to high-finesse cavities,” in *Cavity-Enhanced Spectroscopies* (R. D. v. Zee and J. P. Looney, eds.), vol. 40 of *Experimental Methods in the Physical Sciences*, pp. 1 – 46, Academic Press, 2003.
- [57] A. D. Ludlow, X. Huang, M. Notcutt, T. Zanon-Willette, S. M. Foreman, M. M. Boyd, S. Blatt, and J. Ye, “Compact, thermal-noise-limited optical cavity for diode laser stabilization at  $1 \times 10^{-15}$ ,” *Optics letters*, vol. 32, no. 6, p. 641–643, 2007.
- [58] K. Numata, J. Camp, M. A. Krainak, and L. Stolpner, “Performance of planar-waveguide external cavity laser for precision measurements,” *Optics Express*, vol. 18, no. 22, p. 22781–22788, 2010.
- [59] V. Dolgovskiy, *All-Optical Microwave Generation Using Frequency Combs*. PhD thesis, Université de Neuchâtel, 2012.

- [60] K. Numata, A. Kemery, and J. Camp, “Thermal-noise limit in the frequency stabilization of lasers with rigid cavities,” *Physical Review Letters*, vol. 93, Dec. 2004.
- [61] G. Di Domenico, “Analyse thermique des enceintes de la cavité Fabry-Perot en ULE,” internal report, Laboratoire Temps-Fréquence, Université de Neuchâtel, 2013.
- [62] E. Marín, “Linear relationships in heat transfer,” *Latin-American Journal of Physics Education*, vol. 3, no. 2, p. 9, 2009.
- [63] J. Millo, D. Magalhães, C. Mandache, Y. Le Coq, E. English, P. Westergaard, J. Lodewyck, S. Bize, P. Lemonde, and G. Santarelli, “Ultrastable lasers based on vibration insensitive cavities,” *Physical Review A*, vol. 79, May 2009.
- [64] T. Legero, T. Kessler, and U. Sterr, “Tuning the thermal expansion properties of optical reference cavities with fused silica mirrors,” *JOSA B*, vol. 27, no. 5, p. 914–919, 2010.
- [65] J. Poirson, F. Bretenaker, M. Vallet, and A. Le Floch, “Analytical and experimental study of ringing effects in a Fabry–Perot cavity. application to the measurement of high finesses,” *JOSA B*, vol. 14, no. 11, p. 2811–2817, 1997.
- [66] J. R. Greig and J. Cooper, “Rapid scanning with the Fabry-Perot etalon,” *Applied Optics*, vol. 7, p. 2166–2170, Nov. 1968.
- [67] Z. Li, R. G. T. Bennett, and G. E. Stedman, “Swept-frequency induced optical cavity ringing,” *Optics Communications*, vol. 86, no. 1, pp. 51 – 57, 1991.
- [68] J. Ye, H. Schnatz, and L. Hollberg, “Optical frequency combs: From frequency metrology to optical phase control,” *IEEE Journal of Selected Topics in Quantum Electronics*, vol. 9, pp. 1041–1058, July 2003.

- [69] S. A. Diddams, T. Udem, J. Bergquist, E. A. Curtis, R. E. Drullinger, L. Hollberg, W. M. Itano, W. D. Lee, C. W. Oates, K. R. Vogel, and D. J. Wineland, “An optical clock based on a single trapped  $^{199}\text{Hg}^+$  ion,” *Science*, vol. 293, pp. 825–828, July 2001.
- [70] U. Sterr, C. Degenhardt, H. Stoehr, C. Lisdat, H. Schnatz, J. Helmcke, F. Riehle, G. Wilpers, C. Oates, and L. Hollberg, “The optical calcium frequency standards of PTB and NIST,” *Comptes Rendus Physique*, vol. 5, pp. 845–855, Oct. 2004.
- [71] R. Holzwarth, T. Udem, T. W. Hänsch, J. C. Knight, W. J. Wadsworth, and P. S. J. Russell, “Optical frequency synthesizer for precision spectroscopy,” *Physical Review Letters*, vol. 85, no. 11, p. 2264, 2000.
- [72] D. J. Jones, S. A. Diddams, J. K. Ranka, A. Stentz, R. S. Windeler, J. L. Hall, and S. T. Cundiff, “Carrier-envelope phase control of femtosecond mode-locked lasers and direct optical frequency synthesis,” *Science*, vol. 288, no. 5466, p. 635–639, 2000.
- [73] R. Ell, U. Morgner, F. X. Kärtner, J. G. Fujimoto, E. P. Ippen, V. Scheuer, G. Angelow, T. Tschudi, M. J. Lederer, and A. Boiko, “Generation of 5-fs pulses and octave-spanning spectra directly from a Ti:sapphire laser,” *Optics Letters*, vol. 26, no. 6, p. 373–375, 2001.
- [74] A. Bartels, D. Heinecke, and S. A. Diddams, “10-GHz self-referenced optical frequency comb,” *Science*, vol. 326, pp. 681–681, Oct. 2009.
- [75] B. R. Washburn, S. A. Diddams, N. R. Newbury, J. W. Nicholson, M. F. Yan, and C. G. Jrgensen, “Phase-locked, erbium-fiber-laser-based frequency comb in the near infrared,” *Optics Letters*, vol. 29, no. 3, p. 250–252, 2004.

- [76] G. Marra, R. Slavik, H. S. Margolis, S. N. Lea, P. Petropoulos, D. J. Richardson, and P. Gill, “High resolution microwave frequency transfer over a 86 km-long optical fiber network using an optical frequency comb,” *Optics Letters*, vol. 36, no. 4, pp. 511–513, 2011.
- [77] J. J. McFerran, W. C. Swann, B. R. Washburn, and N. R. Newbury, “Elimination of pump-induced frequency jitter on fiber-laser frequency combs,” *Optics Letters*, vol. 31, no. 13, p. 1997–1999, 2006.
- [78] I. Hartl, G. Imeshev, M. E. Fermann, C. Langrock, and M. M. Fejer, “Integrated self-referenced frequency-comb laser based on a combination of fiber and waveguide technology,” *Optics Express*, vol. 13, no. 17, p. 6490–6496, 2005.
- [79] J. McFerran, W. Swann, B. Washburn, and N. Newbury, “Suppression of pump-induced frequency noise in fiber-laser frequency combs leading to sub-radian  $f_{CEO}$  phase excursions,” *Applied Physics B*, vol. 86, pp. 219–227, Sept. 2006.
- [80] Y. Nakajima, H. Inaba, K. Hosaka, K. Minoshima, A. Onae, M. Yasuda, T. Kohno, S. Kawato, T. Kobayashi, and T. Katsuyama, “A multi-branch, fiber-based frequency comb with millihertz-level relative linewidths using an intra-cavity electro-optic modulator,” *Optics Express*, vol. 18, no. 2, p. 1667–1676, 2010.
- [81] E. Baumann, F. R. Giorgetta, J. W. Nicholson, W. C. Swann, I. Coddington, and N. R. Newbury, “High-performance, vibration-immune, fiber-laser frequency comb,” *Optics Letters*, vol. 34, no. 5, p. 638–640, 2009.
- [82] F. Quinlan, T. M. Fortier, M. S. Kirchner, J. A. Taylor, M. J. Thorpe, N. Lemke, A. D. Ludlow, Y. Jiang, and S. A. Diddams,

- “Ultralow phase noise microwave generation with an Er:fiber-based optical frequency divider,” *Optics Letters*, vol. 36, no. 16, p. 3260–3262, 2011.
- [83] U. Keller, D. A. B. Miller, G. D. Boyd, T. H. Chiu, J. F. Ferguson, and M. T. Asom, “Solid-state low-loss intracavity saturable absorber for Nd:YLF lasers: an antiresonant semiconductor Fabry–Perot saturable absorber,” *Optics Letters*, vol. 17, p. 505–507, Apr. 1992.
- [84] U. Keller, K. J. Weingarten, F. X. Kartner, D. Kopf, B. Braun, I. D. Jung, R. Fluck, C. Honninger, N. Matuschek, and J. Aus der Au, “Semiconductor saturable absorber mirrors (SESAM’s) for femtosecond to nanosecond pulse generation in solid-state lasers,” *Selected Topics in Quantum Electronics, IEEE Journal of*, vol. 2, no. 3, p. 435–453, 1996.
- [85] T. Südmeyer, S. V. Marchese, S. Hashimoto, C. R. E. Baer, G. Gingras, B. Witzel, and U. Keller, “Femtosecond laser oscillators for high-field science,” *Nature Photonics*, vol. 2, no. 10, p. 599–604, 2008.
- [86] A. E. H. Oehler, M. C. Stumpf, S. Pekarek, T. Südmeyer, K. J. Weingarten, and U. Keller, “Picosecond diode-pumped 1.5  $\mu\text{m}$  Er:Yb:glass lasers operating at 10–100 GHz repetition rate,” *Applied Physics B*, vol. 99, pp. 53–62, Feb. 2010.
- [87] S. Pekarek, C. Fiebig, M. C. Stumpf, A. E. H. Oehler, K. Paschke, G. Erbert, T. Südmeyer, and U. Keller, “Diode-pumped gigahertz femtosecond Yb:KGW laser with a peak power of 3.9 kW,” *Optics Express*, vol. 18, no. 16, p. 16320–16326, 2010.
- [88] S. Yamazoe, M. Katou, T. Adachi, and T. Kasamatsu, “Palm-top-size, 1.5 kW peak-power, and femtosecond (160 fs) diode-pumped mode-locked  $\text{Yb}^{+3}$ :  $\text{KY}(\text{WO}_4)_2$  solid-state laser with

- a semiconductor saturable absorber mirror,” *Optics Letters*, vol. 35, no. 5, p. 748–750, 2010.
- [89] R. Holzwarth, M. Zimmermann, T. Udem, T. W. Hansch, P. Russbüldt, K. Gäbel, R. Poprawe, J. C. Knight, W. J. Wadsworth, and P. S. J. Russell, “White-light frequency comb generation with a diode-pumped Cr:LiSAF laser,” *Optics Letters*, vol. 26, no. 17, p. 1376–1378, 2001.
- [90] S. A. Meyer, J. A. Squier, and S. A. Diddams, “Diode-pumped Yb:KYW femtosecond laser frequency comb with stabilized carrier-envelope offset frequency,” *The European Physical Journal D*, vol. 48, pp. 19–26, Jan. 2008.
- [91] S. Pekarek, T. Südmeyer, S. Lecomte, S. Kundermann, J. M. Dudley, and U. Keller, “Self-referenceable frequency comb from a gigahertz diode-pumped solid-state laser,” *Optics Express*, vol. 19, no. 17, p. 16491–16497, 2011.
- [92] M. C. Stumpf, *Diode-pumped solid state lasers for frequency comb generation*. PhD thesis, ETH Zürich, 2009.
- [93] F. X. Kartner, I. D. Jung, and U. Keller, “Soliton mode-locking with saturable absorbers,” *Selected Topics in Quantum Electronics, IEEE Journal of*, vol. 2, no. 3, p. 540–556, 1996.
- [94] A. Schlatter, B. Rudin, S. C. Zeller, R. Paschotta, G. J. Spühler, L. Krainer, N. Haverkamp, H. R. Telle, and U. Keller, “Nearly quantum-noise-limited timing jitter from miniature Er:Yb:glass lasers,” *Optics Letters*, vol. 30, no. 12, p. 1536–1538, 2005.
- [95] B. R. Washburn, W. C. Swann, and N. R. Newbury, “Response dynamics of the frequency comb output from a femtosecond fiber laser,” *Optics Express*, vol. 13, p. 10622–10633, Dec. 2005.
- [96] M. Hoffmann, S. Schilt, and T. Südmeyer, “CEO stabilization of a femtosecond laser using a SESAM as fast opto-optical modulator,” *Optics Express*, vol. 21, p. 30054, Nov. 2013.

- [97] N. Newbury and B. Washburn, “Theory of the frequency comb output from a femtosecond fiber laser,” *IEEE Journal of Quantum Electronics*, vol. 41, pp. 1388–1402, Nov. 2005.
- [98] K. Holman, R. Jones, A. Marian, S. Cundiff, and J. Ye, “Detailed studies and control of intensity-related dynamics of femtosecond frequency combs from mode-locked Ti:sapphire lasers,” *IEEE Journal of Selected Topics in Quantum Electronics*, vol. 9, pp. 1018–1024, July 2003.
- [99] M. C. Stumpf, S. Pekarek, A. E. H. Oehler, T. Südmeyer, and U. Keller, “First CEO beat frequency directly from a 1.5  $\mu\text{m}$  Er:Yb:glass laser oscillator,” in *Lasers and Electro-Optics 2009 and the European Quantum Electronics Conference. CLEO Europe - EQEC 2009. European Conference on*, pp. 1–1, 2009.